Title

On the temporal and spatial flow scales in the near field of homogeneous and immiscible round turbulent jets through image-based measurements

Author

Ibarra, Eric

Publication Date

2021

Peer reviewed|Thesis/dissertation

On the temporal and spatial flow scales in the near field of homogeneous and immiscible round turbulent jets through image-based measurements

By

Eric Ibarra

A dissertation submitted in partial satisfaction of the

requirements for the degree of

Doctor of Philosophy

in

Engineering - Mechanical Engineering

in the

Graduate Division

at

University of California, Berkeley

Committee in charge:

Professor Ömer Savaş, Chair
Professor Phillip Marcus
Professor Evan Variano

Spring 2021

On the temporal and spatial flow scales in the near field of
homogeneous and immiscible round turbulent jets
through image-based measurements

Abstract

On the temporal and spatial flow scales in the near field of
homogeneous and immiscible round turbulent jets
through image-based measurements

Eric Ibarra
Doctor of Philosophy in Mechanical Engineering
University of California at Berkeley
Berkeley, CA 94720-1740
Professor Ömer Savaş, Chair

The work being presented here concentrates on characterizing flow scales of turbulent jets in the near field. Experiments were carried out with water jets and immiscible silicone oil jets of two viscosities submerged in a water tank. The jet Reynolds numbers are in the range of Re $\approx$ 4500 - 50000 for homogeneous water jets and Re $\approx$ 3500 - 27000 for silicone oil jets in water. To observe the turbulent/non-turbulent interface, the jet fluids are made visible by doping with fluorescent dye and excitation with directional illumination. The jet interfaces are continuous and convoluted for water jets, whereas the interfaces of the oil jets are convoluted and discontinuous with droplets and ligaments. Direct flow visualization, schlieren photography, shadowgraph photography and particle image velocimetry are employed as appropriate. Interfacial length scales are characterized using various image processing techniques for both water and oil jet runs. For the homogeneous water jet runs, streamwise internal length scales of the schlieren recording are investigated after applying temporal filters to isolate scales within the flow. When isolated based on their temporal signatures, observations of the homogeneous water jets show that the length scales of internal features increase with Reynolds number. As the Reynolds number increases, the temporal signatures of the features within the jet can be seen populating higher frequency modes. Droplet sizes for the immiscible jet runs are quantified using Hough transformation. Interface length scales decrease with Reynolds number and increase gradually with distance from the exit plane for a given Reynolds number. These scales are isotropic for the homogeneous water jets and exhibit a streamwise to cross-stream ratio of about 1.3 for the oil jets. Results indicate the average droplet size in the immiscible jets is determined by the interfacial surface tension, in relation to the Weber number.

Contents

List of Tables

List of Figures

Chapter 1

Introduction

Figure 1.1 shows examples of the near field within about 6 exit diameters downstream of five jet discharges over a wide range of Reynolds numbers. Frame (a) shows a snapshot of the Deepwater Horizon (DWH)/Macondo Well oil spill in the Gulf of Mexico in April 2010 ([McNutt *et al.*(2011), Savaş(2012), Shaffer *et al.*(2015)]). In this accidental discharge, the upstream conditions in the duct are unknown and the flow conditions in the surrounding water are not well defined. The discharging oil is opaque, hence, only the interface between the jet fluid and the surrounding water is visible. The Reynolds number is estimated as 1.4×10^5 ([Savaş(2012)]). The visible features at the interface are signatures of the jet turbulence. Any quantitative statements regarding the discharge had to be based on these visible interface features. In contrast, frame (b) shows hydrogen-bubble visualization of the near-field cross-sectional view of a laboratory controlled homogeneous water jet egressing from a 5.1 cm diameter nozzle at $Re = 9000$ into quiescent water ([Yule(1978)]). Evidently, the flow at the discharge plane is uniform and free of turbulence. The unstable cylindrical shear layer develops into a series of vortex rings, the celerity of which can easily be determined from a sequence of images, whereupon the volume flux, for example, can be deduced. The vortex rings develop streamwise instabilities at higher Reynolds numbers ([Savaş & Gollahalli(1986)]), but the overall ring structure dominates the near field, which is well understood.

Frames (c), (d) & (e) of figure 1.1, taken from this study and described below, show sample flow images of water and the two silicone oil jets discharging into quiescent water. The Reynolds numbers are high enough that the tripped flows in the discharge tube are developed turbulent flows. That none of the flows show any orderly ring-like structures, such as those seen in figure 1.1(b), may be taken as corroboration of developed turbulent flows in the discharge tube. The homogeneous water jet in frame (c) shows the jet-ambient fluid interface clearly. The discharge liquid is rendered opaque, hence only the interface features are visible. The interface is distorted immediately after the fluid leaves the tube and develops into an intricate topology. Shadows created by the dyed jet fluid make the details of the interface clearly visible. Despite the very intricate shape of the interface, there is no indication that it is disconnected. The interface *shell* lacks the orderliness of frame (b), and is more orderly than in frame (a). In fact, the spatial statistical uniformity suggests that some features of the interface should be tractable, which indicates that quantitative statements about the flow can be made with an acceptable level of confidence. Frames (d) and (e) show 1cS and 5cS-oil jets in water that have visually comparable scales to those in frame (c). Reflections off the convex parts of the convoluted interfaces and the surfaces of the detached oil droplets give a *starry* appearance. As in frame (c), flows at the end of the discharge pipe display evidence of developed turbulent flow in the pipe. In stark contrast to the homogeneous jet in (c), the oil jets exhibit axial striations, or ligaments. Furthermore, instead of the contiguous mushroom-like excursions into the ambient fluid seen in (c), we now see detached oil droplets in the ambient fluid. It is not clear if there are water droplets in the jet fluid, though. Another clearly visible feature is the underlying large scale, arrowhead (chevron) structures in the oil jets (d & e) which do not seem to have a counterpart in the water jet in (c). Even though buoyant plumes in quiescent environments are

not expected to meander, one may associate these features with meandering of the jets, however small in amplitude ([Hübner(2004)]). Perhaps unexpectedly, the lower Reynolds number flow of the 5cS-oil jet in frame (e) has finer scales than the 1cS-oil at a higher Reynolds number in frame (d). Here again, the scales of these features may be related to the overall characteristics of the discharging jet. It is this aspect of the flows that is the subject matter of this paper.

The self-preserving, asymptotic state of the homogeneous round turbulent jet has been well studied (e.g. Abramovich (1963), Hinze (1975)). Here we sample studies mostly of the near field behavior of a jet as it develops from the orifice of discharge. [Crow & Champagne (1971)] present an extensive study on the orderly large coherent structures of well-engineered air jets with clean, uniform initial flow over a range of $0 < x/D < 16$), where x is the downstream distance and D is the exit diameter. [Lau & Fisher(1975)] concluded that, from hot wire measurements, the dominant large scale structure in the first few diameters of a round jet consists of an axial array of toroidal vortices, and as they move downstream they sweep fluid from the high velocity side of the jet to the other and vice versa. [Yule(1978)] presents measurements in air and visualization in water in the near field of well engineered jets where the flow is dominated by toroidal vortices. [Bogusławski & Popiel(1979)] present hot wire measurements in the extended near field ($x/D < 12$) of a jet discharging from a fully developed turbulent pipe flow. They present only mean values and report that the highest turbulence intensities occur around $(x/D, r/D) \sim (6, 1)$. [Dimotakis *et al.*(1983)] present laser-induced fluorescence (LIF) measurements at the far field of turbulent water jets over the Reynolds number range of 500 to 10,000 and conclude the persistence of large scale structures, both circular or helical, in the flow field. [Savaş & Gollahalli(1986)] present schlieren images of the near field of well engineered propane jets in air, both cold and burning, highlighting the toroidal vortical structures. The smoke wire visualization pictures in figures 5 and 6 of [Popiel & Trass(1991)] show the stark difference between a laminar flow at the jet exit and one that is tripped to turbulence with a screen upstream of the exit. The classical toroidal vortical structures are obliterated by turbulence. [Catrakis & Dimotakis(1996)] present scalar data, using LIF in water, at $x/D = 275$ where the jet is in its asymptotic, self-similar state. At this measurement location, the ambient fluid may be entrained across the jet, thus rendering the identification of a contiguous isosurfaces from side view challenging. However, they find that the fractal dimension goes from 1 to 2 as scales go from the lowest (largest) to the highest (smallest). In his review article, [Dimotakis(2000)] discusses the mixing transition which seems to occur at Taylor's Reynolds number of order 100-140. [Hu *et al.*(2003)] present simultaneous particle image velocimetry (PIV) and planar laser-induced fluorescence (PLIF) measurements in the near-nozzle region of a well engineered jet, essentially duplicating and complimenting the work of [Yule(1978)].

Westerweel and coworkers in [Westerweel *et al.*(2002)], [Westerweel *et al.*(2005)], [Westerweel *et al.*(2009)], have presented details of the interface of a homogeneous turbulent water jet of initial diameter of $d = 1$mm at $Re = 2,000$. [Westerweel *et al.*(2002)] present simultaneous PIV and LIF measurements in the water jet, and essentially confirm the results of [Catrakis & Dimotakis(1996)]: that there is a sharp interface between the turbulent and nonturbulent regions of the flow, and irrotational fluid parcels can be found nestled within the rotational turbulent regions. Continuing the work of [Westerweel *et al.*(2002)], based on the analysis of data recorded over $60 < x/D < 100$, [Westerweel *et al.*(2005)] conclude that the turbulence interface propagates outward by a small scale "nibbling" process, which, in turn, implies that large-scale engulfment is not the dominant entrainment mechanism. [Westerweel *et al.*(2009)] reaffirm and further quantify the conclusions in [Westerweel *et al.*(2005)]. [Westerweel *et al.*(2011)], continuing experiments in the same setup used in the earlier studies, conclude that the turbulent interfaces of

isothermal and nonisothermal jets in the far field are essentially the same.

[Hunt *et al.*(2006)] developed approximate models at inhomogeneous turbulence interfaces where local structures control the entrainment processes. In their review article of the Euromech 517 colloquium on interfacial processes and inhomogeneous turbulence (June 2010), [Hunt *et al.*(2011)] classify interfaces into three categories. One of the categories describes the interface between turbulent and non-turbulent regions in a flow, which is similar to the near field of a discharging jet discussed here. They identify numerous issues pertinent to the understanding of those layers. They argue that the features at the interface should be observed from their respective reference frames as the flow scales evolve, instead of the laboratory frame. [Holzner *et al.*(2007)], who studied the small-scale aspects of flows in proximity to the turbulent/nonturbulent interface, concluded that turbulent entrainment occurs through the viscous forces.

[Savaş(2012)] carried out a series of dye flow visualization experiments in water to study the visible flow features in the near field of turbulent jets at Reynolds numbers of $0.3 - 2.2 \times 10^5$. The large coherent structures at the core of the flow and the smaller eddies at the edge show disparate, independent length scales, with convection speeds that are more than an order of magnitude apart. [Shaffer *et al.*(2015)] conducted a series of experiments, exploring techniques to extract flow rates from video images. They show that a routine application of PIV software to a video of the DWH oil leak jet, a frame of which is shown in figure 1.1(a), yields velocities that are 10 – 50% lower than manual measurements of velocities from the advection of the interface features.

At the turbulent/non-turbulent interface of the jet, in the near field, structures form in the free shear layer due to the sharp velocity gradient in the radial direction. This sharp velocity gradient in the radial direction generates vorticity in the azimuthal direction about the axis of the jet. In a non-turbulent jet, these vortical structures would primarily be toroidal in the near field, as seen in the well engineered jet in figure(1.1.b). The Reynolds number for the homogeneous runs investigated here ran from Re $\approx 10^3 - 10^4$, where the flow was tripped with a mesh grid in the pipe $\approx$ 30 pipe diameters upstream to allow the flow to develop into fully turbulent flow field at the discharge orifice. The preceding work spurring these experiments stems from [Savaş(2012)], where experiments were done to characterize the discharge rate of accidental turbulent discharges, such as in the Deepwater Horizon event, shown in figure(1.1.a). The findings left questions open-ended for further research. Methods similar to PIV were performed at the edge of the turbulent homogeneous jet's profile, yet did not give an obvious relation. Analysis of the jet's large-scale structures was limited by requiring prior knowledge of the relationship between the velocity of these structures and the average velocity to allow a reliable flow estimate.

The strong radial velocity gradient is still present at the interface, with velocity fluctuation now predominately existing in the mixing sub layer. These chaotic fluctuations perturb the flow, inciting variations of the vortical structures. The scale of these perturbation-induced features is driven by the intensity of the velocity fluctuations. The analysis consists of processing a 2D intensity signal in time and this intensity signal is illustrative of the vortical structures.

Previous studies centered on relatively high Reynolds number jets, $Re \approx 10^3 - 10^4$ being discharged into a quiescent environment. Within the near field, the flow transitions from a jet with a thin shear layer and large potential core to where the shear layers grow into the vanishing potential core, changing the modes that are carrying the bulk of the energy in the flow. [Lau & Fisher(1975)] suggested that within this near field of the jet's discharge, the mixing sub region may be comprised of an array of torodial vortices about the axis of the jet. Their hot-wire measurements alluded to the passing of the structures, which left signatures that were not entirely chaotic. [Yule(1978)] notes that the existence of vortex rings are short lived due to the introduction of instabilities in the

shear layer; this is noted as clean jet of $Re = 9000$ going into transition. The vortices experiencing instabilities coalesce, the ring's entanglements lead to vortex stretching and smaller scale motions leading to turbulent flow structures, noted as eddies.

The scale downstream of a transitioning jet can be influenced by a range of factors: exit geometry, the history of the flow, vibrations, or if the flow was accelerating or deccelerating due to nozzle or diffuser. In earlier work done by [Crow & Champagne (1971)], the scales along the jet were attributed to two different mechanisms, one pertaining to ripples at the surface of the jet interfaces with the ambient, and the other pertaining to reoccurring structures of puffs presenting themselves at a frequency related by a Strouhal number of 0.3. They found that, as the jet Reynolds number increased, the ripples in the boundary layer thickness shortened as the Reynolds number increased to 10^5. To isolate the large structures of puffs from the ripples caused by instabilities at the interface as the flow transitioned, the flow was tripped in the nozzle of the jet. Within the experiments, the flow was tripped ≈ 30 pipe diameters upstream from the point of discharge, restricting the scale of the flow to be relatable to the reoccurring structures of puffs and how their scales evolve in the near field.

As in work by [Dimotakis *et al.*(1983)] and [Catrakis & Dimotakis(1996)], the large scales of a jet in the far field , $x/d > 10$, appear to be independent of the effects of viscosity in the absence of boundaries at sufficiently high Reynolds numbers around $\mathcal{O}(10^6 - 10^8)$. In the near field, roughly between $1-8$ pipe diameters downstream of the source, the structural history of flow from the point of discharge may still persist. The time scale diffusion, τ_{visc}, is inherently bound to scales which it acts on, $\tau_{visc} \propto \dfrac{\ell^2}{\nu}$. Within the near field, the fine scale turbulence structures are dissipated in a shorter time span compared to larger scales in the flow. Inspecting along the stream-wise direction of a homogeneous jet, the prevalent scale of the structures shift from small to large.

The turbulent/non-turbulent interface showcases a range of feature sizes. These features advect downstream at various speeds; some are only momentary visible, when they are not being obscured by larger, slower moving outer shells. Schlieren recordings provide some insight into the motion of these scales, normally obscured when visualized as an opaque jet. These scales are presented across the width of the jet in a convoluted overlay, making quantifiable observations intractable. Temporally filtering a signal has been shown in [Chitanont *et al.*(2015)] as it is applied to schlieren images to visualize sound waves of known frequency. The desire to isolate fluctuations of particular frequencies provides a framework for parsing through the scales raveled within the schlieren captures. Chitanont filtered both temporally and spatially to isolate known sound wave patterns weakly present in the raw schlieren images, the work here focuses on investigating the scales that might be prevalent at incremental frequency bands.

[Shaffer, Ibarra, & Savaş (2021)] present a particle tracking algorithm with accompanying results. The algorithm is capable of using high particle concentration recordings from PIV intended captures to track individual particles over a large number of frames. The results illustrate the distinct motions of particles as they are entrained from the ambient, whipped along cycloidal paths in the shear layer, or even near the centerline of the jet. These trajectories are used to measure the velocity and Lagrangian acceleration of the particle. This process provides granular tracking of particle motion, allowing possible relations to be made between curvatures of features at the turbulent/non-turbulent interface and the curvature of the cycloids, shown to be present in the shear layer of the jet. Investigations demonstrating a link between these curvature measurements could potentially provide clues to better connect the internal flow conditions to the visible coherent structures at the turbulent/non-turbulent interface. There is information veiled in these coherent

structures, [Coles(1981)]. The velocity of these structures as outlined by [Coles(1985)] has already been paramount in describing the mean velocity profile of jets with few assumptions.

The work here focuses on the near field ($x/D < 8$) of homogeneous and immiscible submerged turbulent discharges. Direct flow visualization, schlieren and shadowgraph photography, and PIV are employed simultaneously in various binary combinations. The experimental setup is described first and the relevant definitions are presented. Next, the homogeneous water jets are discussed, followed by the interfacial curvature and length scale analyses, then internal length scales from the schlieren runs. The oil jets are shown subsequently, followed by the interface scale analysis, oil droplet distribution analyses using Hough transformation, and closing remarks. Part of the results presented here have been published in [Ibarra, Shaffer, & Savaş (2020)].

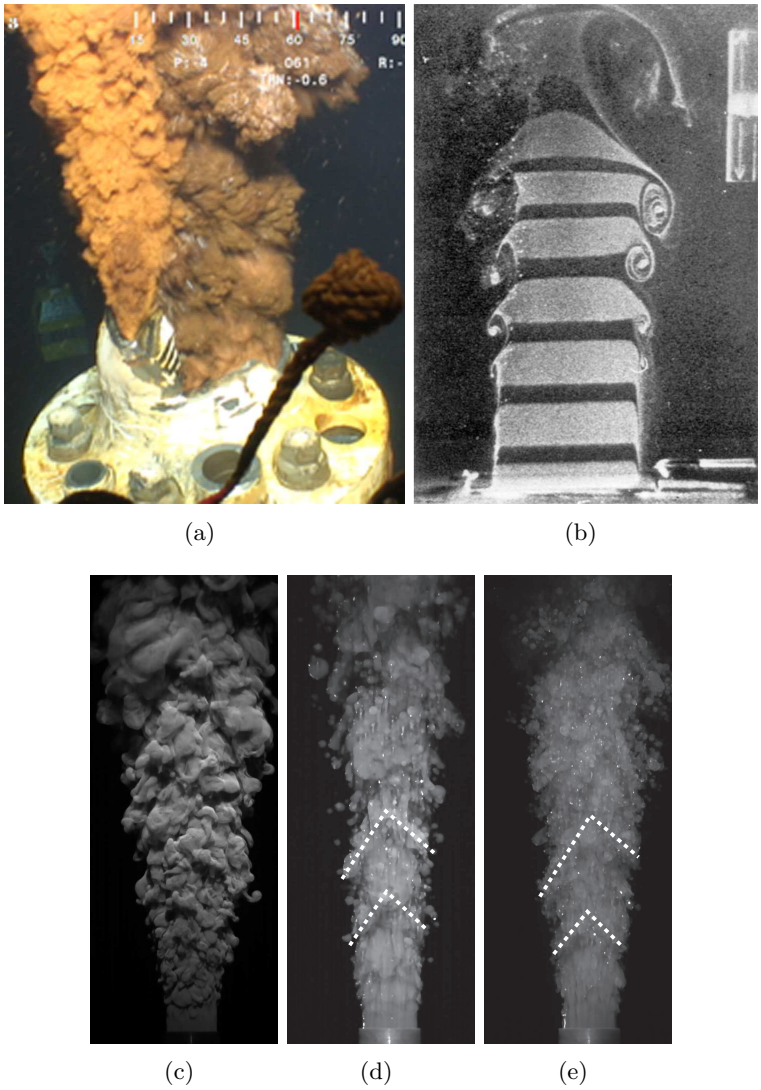

Figure 1.1: Near fields of five jets: (a) an accidental oil discharge into sea water from a 50-cm diameter severed pipe at a submarine oil field well-head where the flow conditions are mostly unknown, the Reynolds number is estimated as 1.4×10^5 [Savaş(2012)], (b) a well engineered homogeneous water jet from a 5.1 cm diameter nozzle where all conditions are known [Yule(1978)], (c) an opaque homogeneous water jet, (d) 1cS silicone oil, and (e) 5cS silicone oil of discharging developed turbulent flow in a 1.38 cm diameter pipe (from the current study). Frame (c) water jet: Re = 0.59×10^4, (d) 1cS-oil jet: Re = 2.41×10^4, and (e) 5cS-oil jet: Re = 0.80×10^4. Flows 1, 21 & 24 in Table 2.2, respectively.

Chapter 2

Experimental Setup

2.1 Flows

Figure 2.1 shows the schematics of the experimental setup employed in the experiments described here, consisting of the flow loop and the optical layout. The flow loop is shown in figure 2.1(a). Experiments are conducted in an available $120^{\mathrm{W}} \times 240^{\mathrm{L}} \times 120^{\mathrm{H}}\mathrm{cm}^3$ glass water tank at a water level of about 105 cm. Jet liquids are discharged into the tank through a vertical smooth copper tube of inner diameter $D = 1.38$ cm, outer diameter of 15.9 mm and length of 42 cm: hence, a length-to-diameter ratio of 30. The end of the tube is machined square. A 30-mesh screen is placed at the entrance to the tube to insure uniformity at the beginning and also trip the flow to promote transition to turbulent flow. The tube protrudes from the center of a 68-cm diameter ground plane. The discharge end of the tube is about 50 cm below the free surface of the water tank. The apparatus is a compromise between a desire to achieve high Reynolds numbers (cf. $\mathcal{O}(10^5)$ for Deepwater Horizon discharge) and a desire to approximate an unbounded domain, hence the small diameter of the discharge tube. Water and two silicone oils of viscosities of 1cS and 5cS (Clearco Products Co.: PSF-1cSt Octamethyltrisiloxane (Trisiloxane) and PSF-5cSt Polydimethylsiloxane/PDMS (Dimethicone)) are used as the discharge jet fluids. The properties of the liquids are given in Table 2.1. The interfacial tension between the oils and water, σ_{ow}, are estimated using the method suggested by [Girifalco & Good(1957)]. We note here that the 5cS-oil has a lower interfacial tension in water than that of the 1cS-oil. The water jet was colored with fluorescein sodium salt solution injected upstream into the flow circuit from a dye reservoir (dye reservoir concentration: 1 g/l, 0.1% by weight). The oil jets are colored with oil soluble fluorescent tracing dye (Kingscote Chemicals, # 506250-RF16, jet fluid concentration 0.07% by weight). The fluorescein dye used in water experiments was neutralized using common chlorine bleach (Chlorox).

Table 2.2 lists the experiments of this study. During the flow visualization runs with water jets, the jet fluid is directly supplied from the laboratory supply line. The inherent lower temperature of the supply line water, usually few degrees Celsius $\Delta T = \mathcal{O}(5^\circ)$ lower than the ambient temperature, has been sufficient to provide high enough refractive index difference of $\Delta n = \mathcal{O}(0.001)$ at a low density difference of about $\Delta\rho \approx 0.0012$ g/cm^3 between the jet fluid and the stagnant water in the tank to facilitate schlieren photography. During the PIV runs, a centrifugal pump is employed to generate the water jets by recirculating the seeded water in the tank. For simultaneous PIV and schlieren photography, the copper supply line was wrapped with an electric heating pad to heat the jet fluid slightly to obtain sufficient refractive index difference for schlieren imaging. During all water jet runs, the flow rate was set by a ball valve and monitored by an industrial grade turbine flow meter of 1% accuracy (GPI Model No: G2S07N09GMA).

The water jets were operated manually and run *continuously*, while the oil jets were run on extremely short intervals under computer control to minimize the oil usage. The oil jets were driven by a calibrated gear pump (PENTAIR Model: SHURFLO BBV5) coupled to a microstepper motor (Compumotor). The runs consisted of ramp up, pre-acquisition steady state, image acquisition, and ramp down phases that are synchronized with the imaging system, all under computer control. The pre-acquisition periods ranged from 4 to 40 seconds, for the highest and the lowest flow rates in Table 2.2, respectively. These time lags allowed ample time for the oil jets to reach the free

surface and spread laterally, reaching steady states before the data acquisition is initiated. The jet oil was contained by a pontoon at the free surface of the tank for quick recovery, recycling into the experiment, and eventual storage. The large differences in refractive indices and the immiscibility of water and oils precluded PIV, schlieren and cross-sectional visualization of the oil jets.

2.2 Optics

There were two experimental setups used for the work presented here. The schematics of the optical layouts for the first set of experiments—capturing schlieren/shadowgraph imaging, interface flow visualization, cross-sectional visualization, and PIV—are all shown jointly in figure 2.1(b). These imaging techniques could be utilized simultaneously as appropriate, as listed in table 2.2.

The classical schlieren layout using two concave mirrors, each of 400-cm focal length and 45-cm diameter, in the Z-configuration is employed here. As shown in figure 2.1(b), the path of the schlieren system wrapped around the tank by folding the classical Z-configuration using two large front surface flat mirrors. The beam path is set at 12° off the normal to the laser sheet in order to allow clear 90° access for the flow visualization cameras. An LED light source is used for illumination (Leica KL 1500LED). The light beam is shaped using a matched achromatic doublet lens pair (Thorlabs MAO:103030-A), a pinhole, and a microscope objective. The system is used both with a single knife edge and simultaneously with two orthogonal knife edges after the light beam is split by a cubical beam splitter.

For PIV, the tank is seeded with silver-coated hollow ceramic spheres of diameter 45μm (Potter Industries Inc., AG-SF-20, 0.8 g/cm^3). The illumination is done using a 10W CW argon-ion laser (American Laser Corporation). PIV data analysis is done using an in-house software package ([Sholl & Savaş(1997), Ortega *et al.*(2003), Bardet *et al.*(2010), Bardet *et al.*(2018)]) , and post processing using various commercial software packages. The laser sheet is also used for cross sectional visualization of the water jets by exciting fluorescent dye in the jet, while the tank had no particles. The immiscibility of oils and water, and their mismatched refractive indices, precludes cross sectional viewing of the oil jets in water. Of the two sets of experiments that are presented here, runs [1-29] are listed in table 2.2 and runs [30-35] are listed in table 2.3. The equipment and setup were effectively identical between the two set of runs. A modification was made in the routing of the laser. Due to the attenuation of the laser sheet through the length of the tank, the laser sheet was instead routed from above to illuminate the same cross-sectional plane of the jet from the first set of experiments. An acrylic viewing box was submerged below the air-water interface of the tank above the discharge pipe to prevent interfacial bending of the light beam from the disturbed surface during runs. An illustration of the setup for the second set of runs is presented in figure 2.2. The bottom of the submerged viewing box was 49cm, around 40 pipe diameters downstream, above the discharge orifice.

The interface of the dyed jet fluid was recorded under oblique, nearly collimated illumination from a 1000-lumen LED flash light set to illuminate the length of $\sim 10D$ downstream from the discharge orifice. The light was directed so that the refracted light illuminated the jets at 35° with the horizontal plane as shown in figure 2.1(c). The flow fields are recorded simultaneously by two high speed cameras , IDT–X3 and IDT–Y3, in various imaging modes. The cameras both have 1280×1024 pixels native image resolution and are both operated at 1280×512 pixels resolution, set at 94 μm/pixel spatial resolution from run numbers [1-29] in table 2.2 and 95 μm/pixel spatial resolution from run numbers [30-35] in table 2.3. They are operated in continuous mode. For

simultaneous imaging, the cameras are synchronized in leader-follower mode. Operating details are give in table 2.2.

For both water and oil experiments, jets were vertically discharged into the tank of quiescent water. Within the near field we investigated, the Morton length scale ([Morton(1959), Turner(2012)]) was sufficiently large to neglect buoyancy effects on the flows for the oil runs listed in table 2.2.

2.3 Definitions

The coordinate system (x, r) at the central plane of the jets is shown in figure 2.1. The corresponding velocity components in the plane are $\mathbf{u} = (u_x, u_r)$. The velocity vector is decomposed as

$$\mathbf{u} = \mathbf{U} + \mathbf{u}' \tag{2.1}$$

where $\mathbf{U} = (U_x, U_r)$ are the time averaged components and $\mathbf{u}' = (u'_x, u'_r)$ the fluctuating components. Overbars are used to indicate averages. The centerline velocity is denoted as $U_0(x)$. For convenience, the radial coordinate r will at times be substituted by y.

Table 2.2 lists the first set of experiments carried out in this study. The main parameter in the experiments is the jet discharge rate Q. The mean discharge velocity U is written as

$$U = \frac{4}{\pi}\frac{Q}{D^2} \ . \tag{2.2}$$

The Reynolds number Re

$$Re = \frac{4}{\pi}\frac{Q}{\nu_j D} \tag{2.3}$$

is based on the jet discharge pipe diameter $D = 1.38$ cm, the kinematic viscosity of the jet liquid ν_j and the volumetric flow rate Q. The momentum *injection* rate M is based on the flow rate Q and the mean discharge velocity U

$$M = J/\rho_j = QU = \frac{4}{\pi}\frac{Q^2}{D^2} \tag{2.4}$$

where J the jet momentum and ρ_j the density of the jet liquid. Buoyancy flux B is written as

$$B = gQ\left(\frac{\rho_w - \rho_j}{\rho_w}\right) = gQ\left(\frac{\Delta\rho}{\rho_w}\right) \tag{2.5}$$

where g is the gravitational acceleration, ρ_w the density of the ambient water, and $\Delta\rho = \rho_w - \rho_j$. The Morton length ℓ_M is written as

$$\frac{\ell_M}{D} = \frac{M^{\frac{3}{4}}/B^{\frac{1}{2}}}{D} \tag{2.6a}$$

$$= \left(\frac{\pi}{4}\right)^{1/4}\left(\frac{\rho_w}{\Delta\rho}\right)^{1/2}\frac{\nu_j}{g^{1/2}D^{3/2}}\ Re \tag{2.6b}$$

The ℓ_M is used to gauge the effect of the buoyancy on the oil jets in the near field. Note that $\ell_M \to \infty$ for homogeneous jets for which $\Delta\rho \approx 0$.

The Capillary number for the oils' jets is written as

$$Ca = \frac{\mu_j U}{\sigma_{ow}} = \frac{4}{\pi}\frac{\mu_j Q}{\sigma_{ow} D^2} \tag{2.7}$$

where μ_j is the dynamic viscosity of the jet fluid. The Weber number is now written as

$$We = Ca \times Re = \frac{\rho_j U^2 D}{\sigma_{ow}} = \frac{16}{\pi^2}\frac{\rho_j Q^2}{\sigma_{ow} D^3}\ . \tag{2.8}$$

The Richardson number is also defined for reference

$$Ri = \frac{\Delta\rho}{\rho_w}\frac{gD}{U^2} \tag{2.9}$$

The Morton length scale in equation 2.6 may also be written in terms of the Richardson number as

$$\frac{\ell_M}{D} = \left(\frac{\pi}{4}\right)^{1/4} Fr^2\, Ri \tag{2.10}$$

where the Froude number, which is defined as $Fr = U/\sqrt{gD}$.

In preparation for discussing the turbulence characteristics of flows, we estimate the energy dissipation rate ϵ, [Hinze(1975)], at the exit of the discharge tube as

$$\epsilon = \left(\frac{4}{\pi}\right)^3 \frac{Q^3}{D^7} \tag{2.11}$$

and the Kolmogorov length scale η and wavenumber k_η based on the jet fluid is

$$\eta = \frac{1}{k_\eta} = \left(\frac{\nu_j^3}{\epsilon}\right)^{1/4} = Re^{-3/4} D \tag{2.12}$$

and the time scale

$$\tau = \left(\frac{\nu_j}{\epsilon}\right)^{1/2} = \frac{\pi}{4}\ Re^{-1/2}\ \frac{D^3}{Q}. \tag{2.13}$$

Table 2.2 lists U, the Reynolds and Richardson numbers, the estimates of the Morton lengths, and the Kolmogorov scales based on the parameters of the jets. Simultaneous imaging modes are also indicated in the table. The Kolmogorov length scale was used to non-dimensionalize the interface features of the jets, namely, the curvature spectra for the homogeneous water jet runs and droplet size-spectra in oil jet experiments. Table 2.3 provides the same parameters detailed above for runs [30-35].

liquid	ρ_j $[kg/m^3]$	ν_j $[m^2/s]$	σ_a $[N/m]$	σ_{ow} $[N/m]$	n
water	998.2	1×10^{-6}	7.28×10^{-2}	n/a	1.330
1cS silicone oil	816.5	1×10^{-6}	1.74×10^{-2}	1.90×10^{-2}	1.383
5cS silicone oil	916.3	5×10^{-6}	1.97×10^{-2}	1.68×10^{-2}	1.397

Table 2.1: Jet fluid properties at $20°C$. σ_a and σ_{ow} are the surface tension in air and interfacial tension in water of the jet liquids, respectively. σ_{ow}'s are estimated using the method suggested by [Girifalco & Good(1957)].

flow #	U $[m/s]$	Re		Ri		We		ℓ_M/D	η $[\mu m]$	**FR/exp.** $[fps]/[\mu s]$	**imaging mode**
					water jets						
1	0.46	0.59		69.4		-		∞	20.4		ScV/FV
2	0.94	1.20		16.8		-		-	12.0		ScV/FV
3	1.88	2.39		4.23		-		-	7.2	500/998	ScV/FV
4	3.39	4.31		1.30		-		-	4.6		ScV/FV
5	4.95	6.29		0.61		-		-	3.5		ScV/FV
6	5.69	7.22		0.46		-		-	3.1		ScV/FV
7	0.46	0.58		71.8		-		-	20.9		ScV/ScH
8	0.94	1.20		16.8		-		-	12.0		ScV/ScH
9	1.96	2.49	$\times 10^4$	3.90	$\times 10^{-5}$	-		-	7.0		ScV/ScH
10	2.82	3.58		1.88		-		-	5.3	1000/995	ScV/ScH
11	3.66	4.65		1.11		-		-	4.3		ScV/ScH
12	4.70	5.97		0.68		-		-	3.6		ScV/ScH
13	5.74	7.29		0.45		-		-	3.1		ScV/ScH
14	0.46	0.59		69.4		-		-	20.4		ScV/PIV
15	0.91	1.16		18.0		-		-	12.3		ScV/PIV
16	1.83	2.32		4.49		-		-	7.3	2000/494	ScV/PIV
17	3.62	4.60		1.14		-		-	4.4		ScV/PIV
18	4.20	5.33		0.85		-		-	3.9		ScV/PIV
					1cS-oil jets						
19	0.32	0.40		22.9		0.07		1.8	27.4		Shd/FV
20	0.63	0.80		5.72		0.27		3.5	16.3		Shd/FV
21	1.90	2.41	$\times 10^4$	0.63	$\times 10^{-2}$	2.43	$\times 10^3$	10.5	7.1	1000/498	Shd/FV
22	2.53	3.21		0.35		4.32		14.0	5.8		Shd/FV
23	3.17	4.02		0.22		6.80		17.5	4.9		Shd/FV
					5cS-oil jets						
24	0.32	0.80		10.3		0.08		2.6	91.5		Shd/FV
25	1.26	3.21		0.64		1.22		10.4	32.3		Shd/FV
26	1.58	4.02	$\times 10^3$	0.41	$\times 10^{-2}$	1.91	$\times 10^3$	13.0	27.4	1000/498	Shd/FV
27	1.90	4.82		0.28		2.75		15.6	23.9		Shd/FV
28	2.53	6.43		0.16		4.89		20.8	19.2		Shd/FV
29	3.16	8.03		0.10		7.63		26.0	16.3		Shd/FV

Table 2.2: Scope of the experiments. Flow numbers are used for identification in the discussion. Simultaneous imaging modes are indicated as pairs of FV-flow visualization, ScH-schlieren with horizontal knife edge, ScV-schlieren with vertical knife edge, Shd-shadowgraph, and PIV-particle image velocimetry.

flow #	U $[m/s]$	Re		Ri		We	ℓ_M/D	η $[\mu m]$	**FR/exp.** $[fps]/[\mu s]$	**imaging mode**
	water jets									
30	0.49	0.62	$\times 10^4$	62.7	$\times 10^{-5}$	-	∞	19.7	2000/497	ScV/FV
31	0.85	1.08		20.7		-	-	13.0		ScH/PIV
32	1.61	2.04		5.8		-	-	8.1		ScH/PIV
33	1.94	2.46		4.0		-	-	7.0		ScH/PIV
34	2.79	3.54		1.9		-	-	5.3		ScH/PIV
35	3.59	4.56		1.2		-	-	4.4		ScH/PIV

Table 2.3: Scope of the 2nd set of experiments between July-August 2020. Flow numbers are used for identification in the discussion. Simultaneous imaging modes are indicated as pairs of ScH-schlieren with horizontal knife edge and PIV-particle image velocimetry.

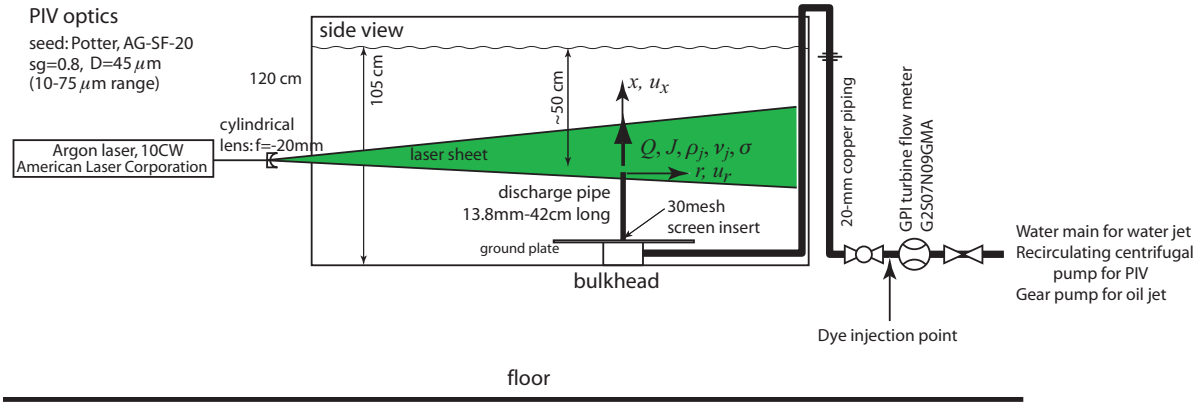

(a)

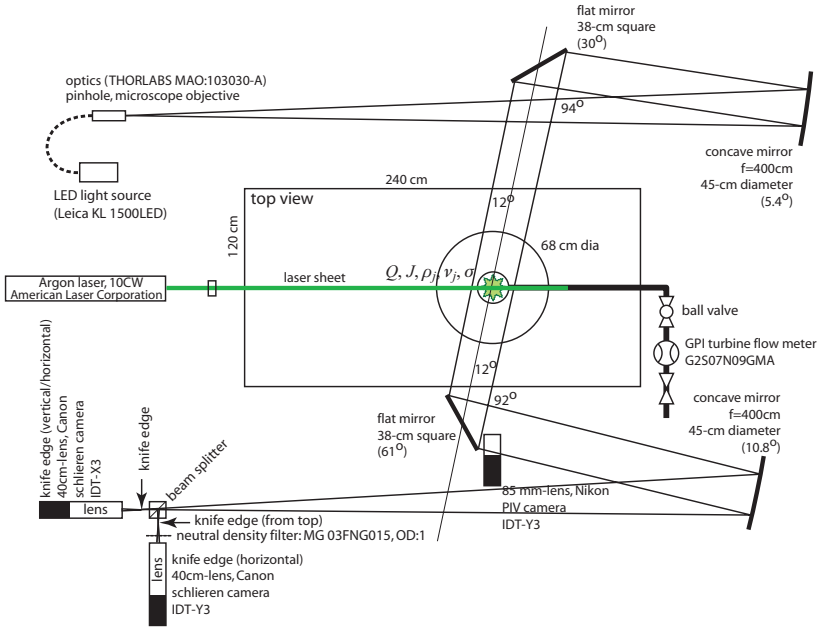

(b)

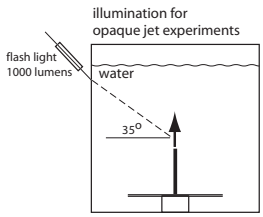

(c)

Figure 2.1: Experimental setup: (a) flow geometry, cross-sectional illumination, and (x, r) coordinate system and the corresponding velocity components (u_x, u_r) (side view) (b) schlieren system and camera positions (top view), and (c) illumination for interface visualization (end view).

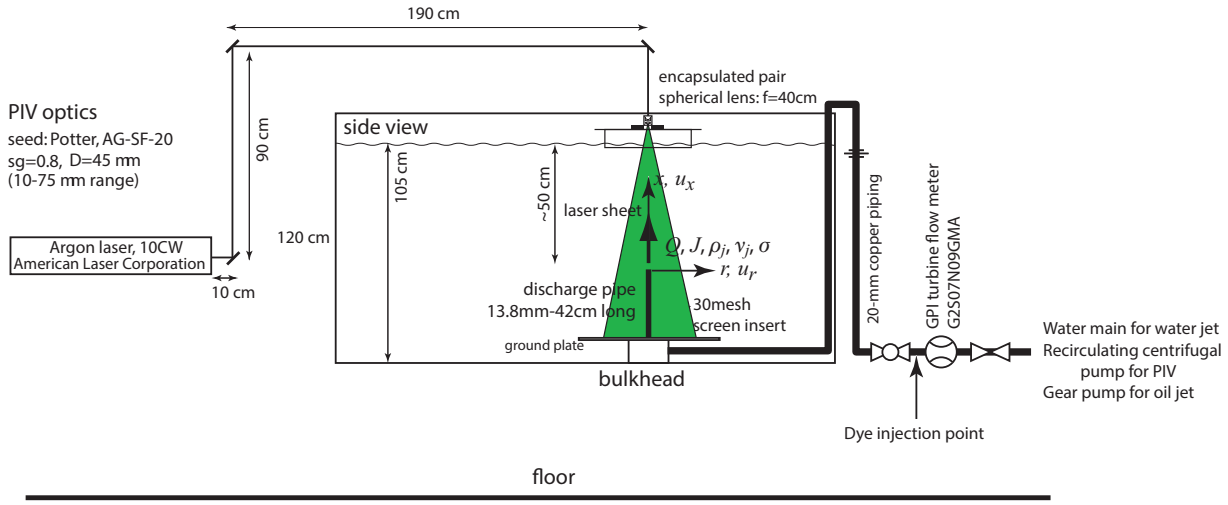

(a)

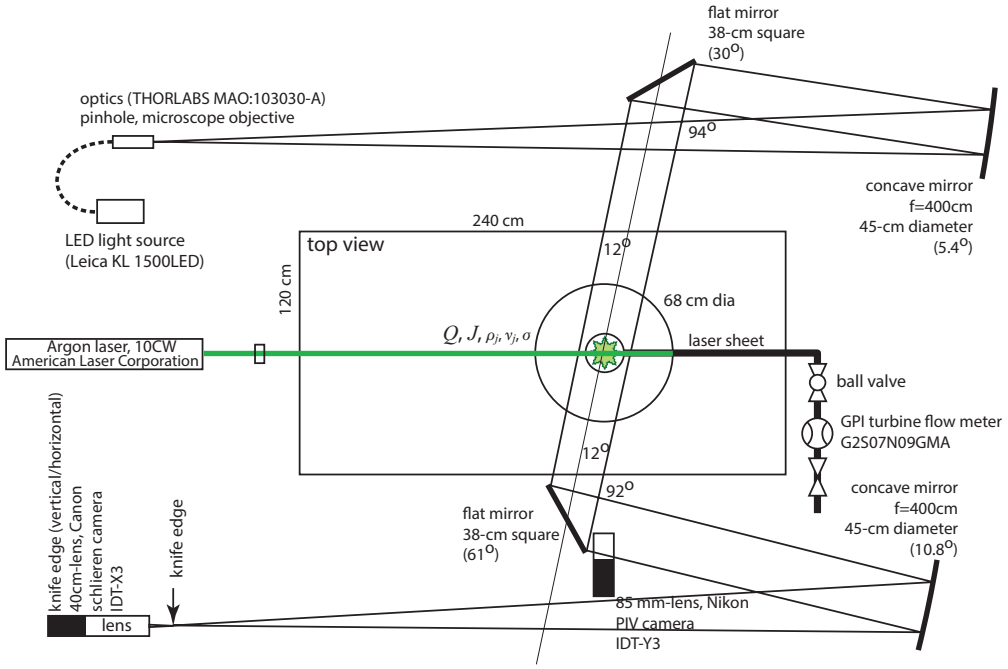

(b)

Figure 2.2: Experimental setup for second set of experiments: (a) flow geometry, cross-sectional illumination, and (x, r) coordinate system and the corresponding velocity components (u_x, u_r) (side view) (b) schlieren system and camera positions (top view), and

Chapter 3

Homogeneous Water Jets

3.1 Flow Visualization

3.1.1 Edge Visualization

Figure 3.1 shows sample flow images of fluorescent dyed homogeneous water jets at three Reynolds numbers. The discharge flows at the tube exit are evidently turbulent as the interfaces deform well within one diameter of the exit plane (cf. figure 1.1(b)). At the lowest Re (5.9×10^3) in frame (a), the jet-ambient fluid interface is sharply defined; the camera resolution seems to be sufficient to capture all flow surface details. At the intermediate Re (2.39×10^4) in frame (b), there is a stark decrease in the size of the interface features, as expected with increasing Reynolds number. At the highest Re (7.22×10^4) in frame (c), the image has become blurred. There are two obvious reasons for this: the expected size of the turbulence is getting smaller, hence falling out of the spatial resolution of the camera, and the exposure time of the camera is longer than the time scale of the finer scale interface features, hence blurring the images.

Figure 3.2 shows averages of 2048 images corresponding to about 4 seconds of the flows in figure 3.1. The length of the image sequence is not long enough to produce a smooth mean image at the lowest Reynolds number in frame (a), which is not unexpected. A study of the corresponding video sequence indicates that the outermost features of the jet fluid move very slowly compared to the features that are deeper in the jet. In fact, some of the jet fluid parcels seem to be nearly stagnant when they have moved away from the jet and into the ambient fluid. The length of the image sequence in frame (b) seems to be barely enough to generate a smooth average image. This aspect of the flow is discussed further below in connection with schlieren imaging. The averaged flow picture in frame (c), however, is smooth, indicating the four seconds of flow at this Reynolds number is sufficiently long to capture an adequate number of slow moving jet fluid parcels at the edge of the jet to obtain a meaningful average. The average jet half-spreading angle is estimated from the images to be about 12° at the the lowest Reynolds number (Flow 1) and about 8° at the highest Reynolds number (Flow 6). The half angle decreases monotonically with increasing Reynolds number.

3.1.2 Schlieren Visualization

Simultaneous flow visualization at the jet's edge and schlieren visualization through the jet are available for water jet experiments (Table 2.2). The schlieren images corresponding to those in figure 3.1 are shown in figure 3.3, at a slightly lower magnification. As opposed to the edge (shell) visualization, a schlieren image gives an integrated view of the jet along the light path, superimposing all scales of the jet. Frames (a) and (b) show much finer textures than the corresponding images in figure 3.1, as the result of projecting all the flow details across the jet onto a plane. The details get finer as the Reynolds number increases four-fold from (a) to (b). A further increase of three-fold in Re from (b) to (c) is expected to generate even finer details in the flow field in frame (c). However, the imaging capability of the camera is not able to capture these finer details. Hence only the large, slower moving features are recorded in the image.

The schlieren video sequences show nearly stagnant jet fluid parcels at the edge, along with very fast moving flow features in the interior of the jet. The human eye is able to distinguish these features that are moving at disparate speeds. To some limited degree, features moving at high speed below the *canopy* of slow moving outer features can also be identified in the shell visualization videos, but the opacity of the jet fluid limits the visible depth past the edge of the jet. A technique to separate these features based on their speeds by using a temporal filter will be discussed.

3.1.3 PIV

Figure 3.5 shows sample simultaneous schlieren and raw PIV images of the homogeneous water jet experiment, corresponding to Flow 16 at Reynolds number 2.32×10^4 in table 2.2. Also shown is the corresponding instantaneous PIV data as the magnitude of the planar component velocity vector $\mathbf{u} = (u_x, u_r)$, highlighting its spatial variation. Figure 3.6 shows averaged PIV measurements for Flow 16. The data are averaged over 2000 frames. Mean velocity, turbulence intensity, mean vorticity, and mean enstrophy are shown. Shown in figure 3.7 are selected mean velocity profiles for Flows 14, 15 and 16. The data are scaled with the local centerline velocity $U_0(x)$ and the local jet half-width $r_{1/2}(x)$ defined as $U_x(x, r_{1/2}) = U_0(x)/2$. Even at the near field, the jets seem to approach Gaussian profiles at these Reynolds numbers: 6,000, 12,000, and 24,000, respectively.

The work presented here focuses on two approaches for analyzing the scales on the surface of turbulent/non-turbulent interfaces: curvature analysis and length scale estimation. Video image sequences are sampled at intervals commensurate with the size of the region of interest (ROI) which are *square tiles* of order D employed during segmentation of the images, hence, a sampling interval of $\mathcal{O}(D/U)$.

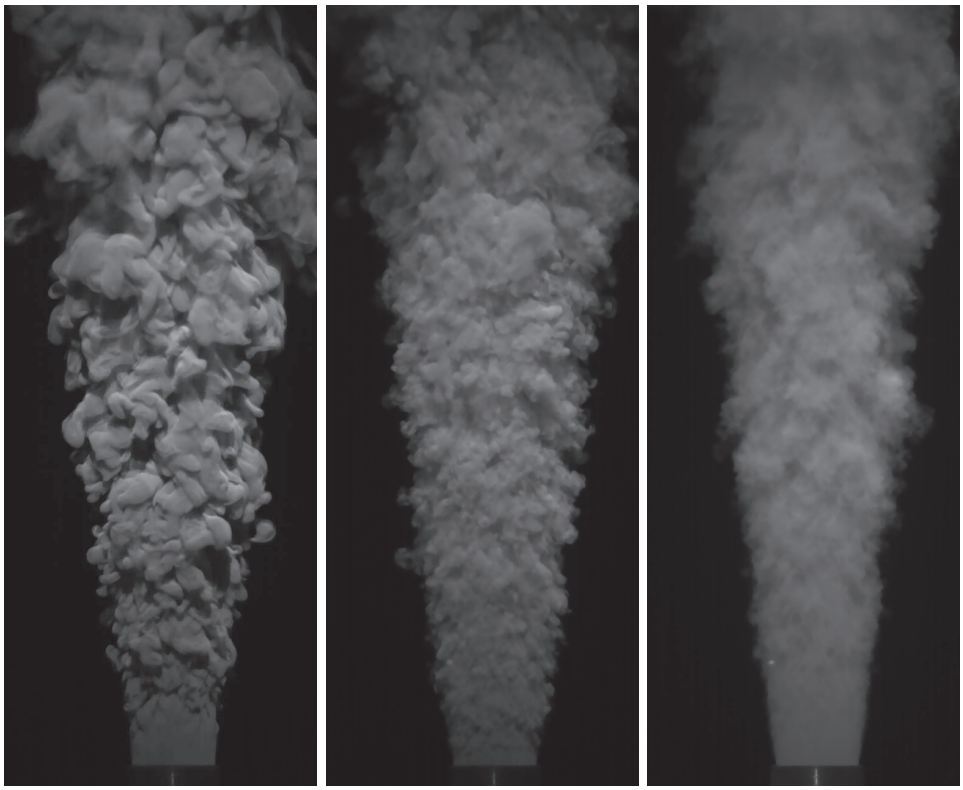

(a) $\mathrm{Re} = 0.59 \times 10^4$ (b) $\mathrm{Re} = 2.39 \times 10^4$ (c) $\mathrm{Re} = 7.22 \times 10^4$

Figure 3.1: Fluorescent water jet experiments: instantaneous images. Flows 1, 3 & 6.

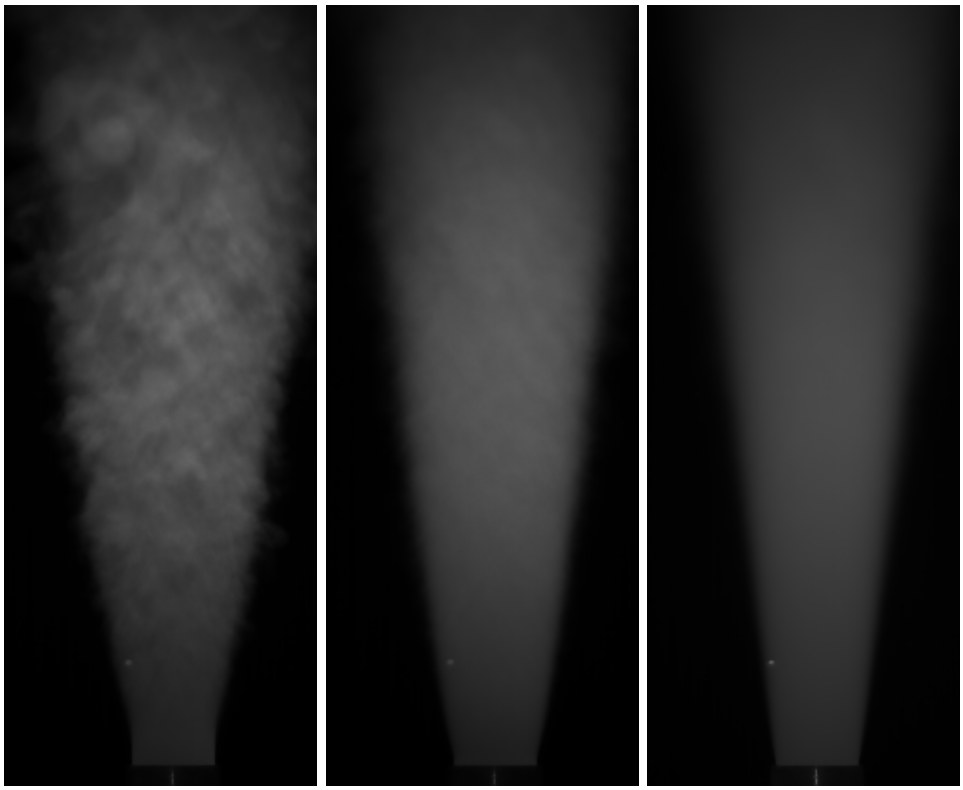

(a) Re $= 0.59 \times 10^4$ (b) Re $= 2.39 \times 10^4$ (c) Re $= 7.22 \times 10^4$

Figure 3.2: Fluorescent water jet experiments: averages of 2048 images: Flows 1, 3 & 6.

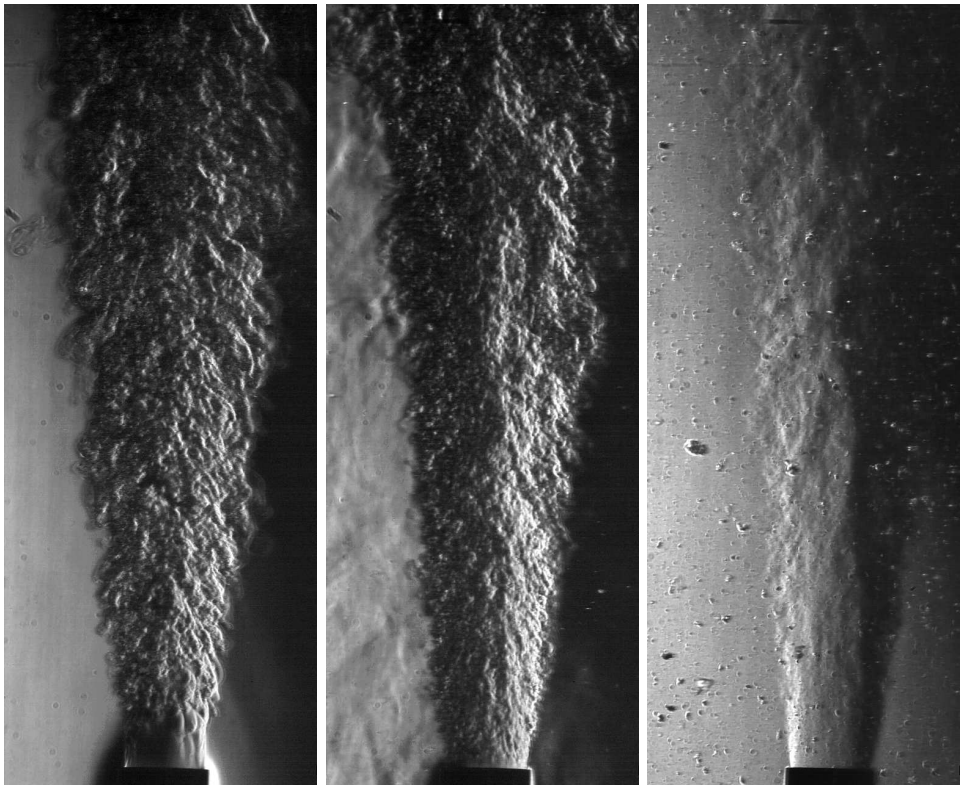

(a) $\mathrm{Re} = 0.59 \times 10^4$ (b) $\mathrm{Re} = 2.39 \times 10^4$ (c) $\mathrm{Re} = 7.22 \times 10^4$

Figure 3.3: Fluorescent water jet experiments: instantaneous schlieren images corresponding to the frames in figure 3.1; Flows 1, 3 & 6.

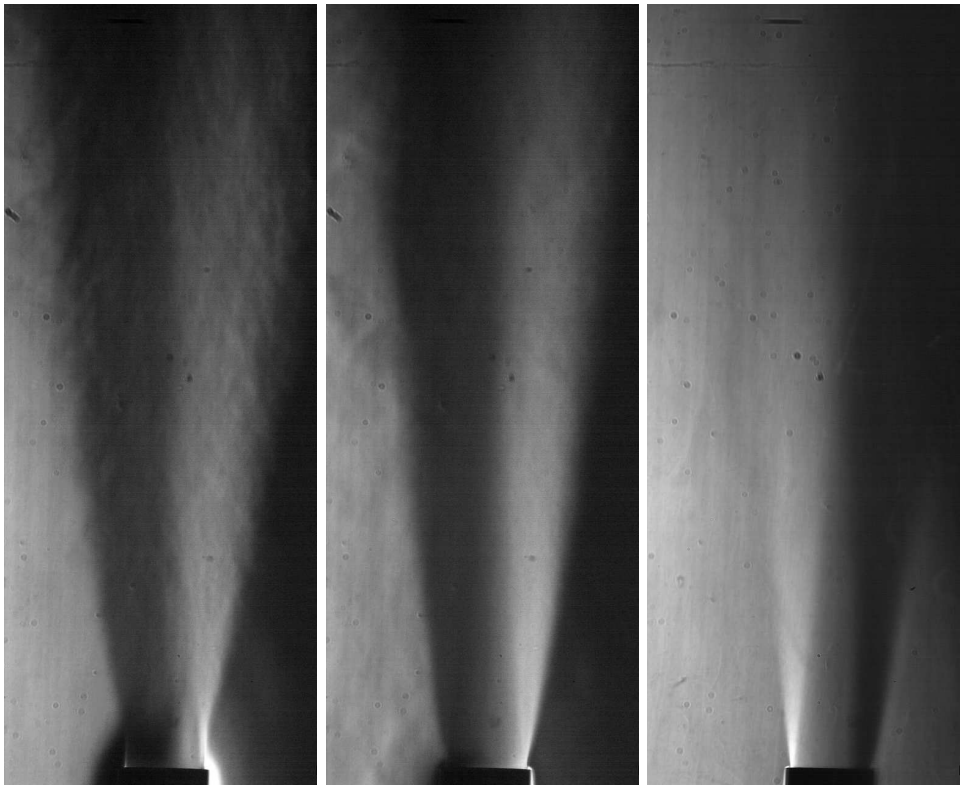

(a) $\mathrm{Re} = 0.59 \times 10^4$ (b) $\mathrm{Re} = 2.39 \times 10^4$ (c) $\mathrm{Re} = 7.22 \times 10^4$

Figure 3.4: Fluorescent water jet experiments: average of 2048 schlieren images corresponding to the frames in figure 3.2; Flows 1, 3 & 6.

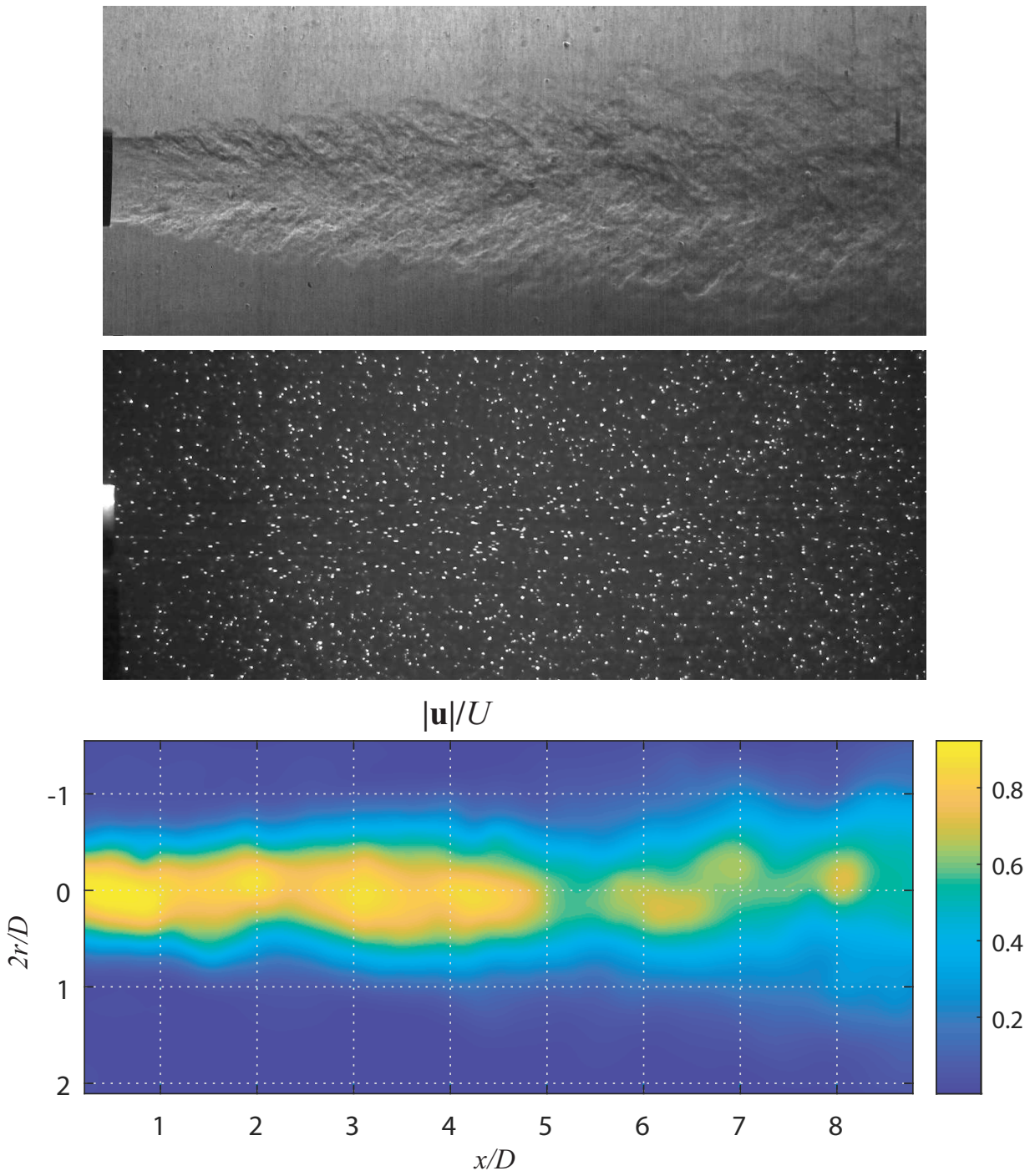

Figure 3.5: Sample simultaneous schlieren (top) and PIV (middle) images and velocity magnitude (bottom) corresponding to Flow 16 in Table 2.2. $U = 1.83$ m/s. The end of the discharge tube is visible on the left in the images.

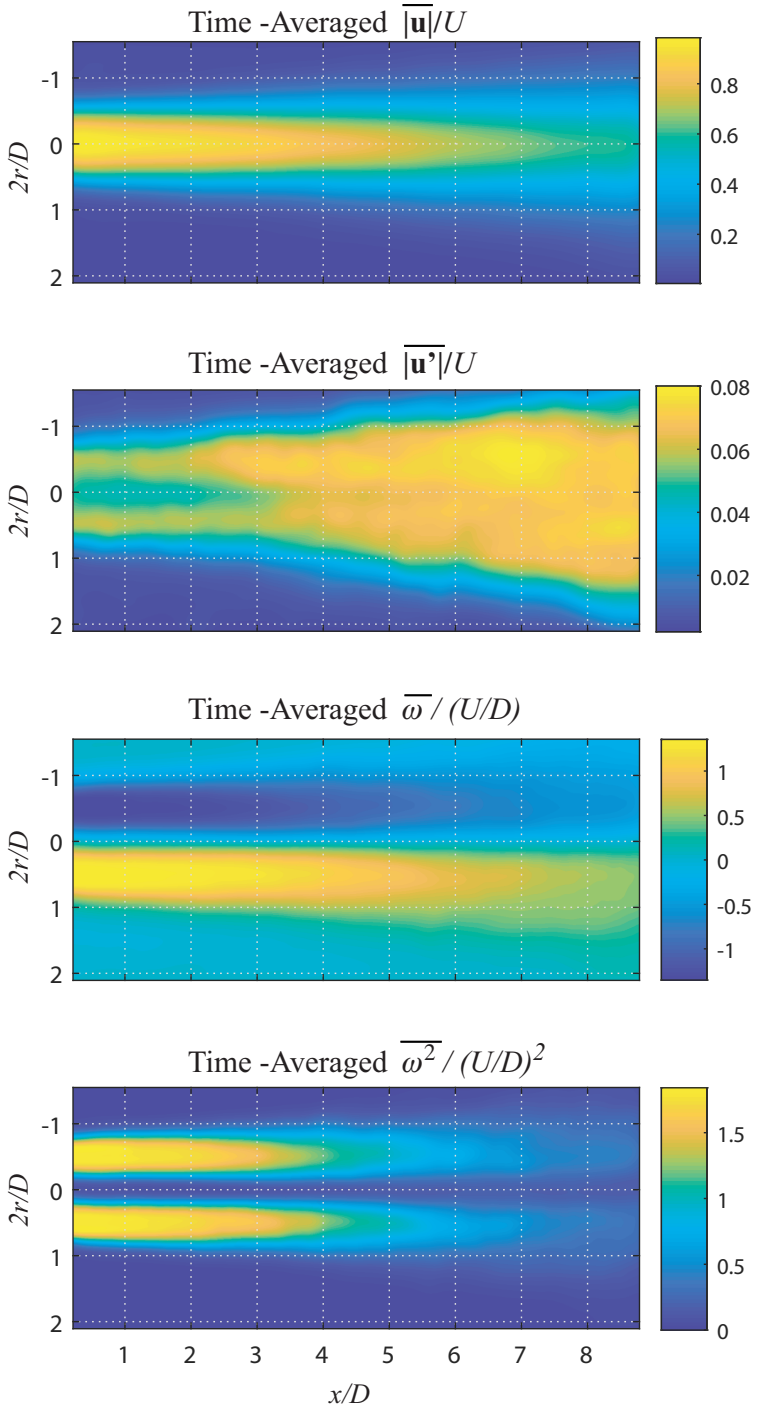

Figure 3.6: Average velocity, turbulence intensity, vorticity, and enstrophy in homogeneous water jet: $Re = 2.4 \times 10^4$. Flow 16 in Table 2.2, $U = 1.83$ m/s and $U/D = 133\ s^{-1}$.

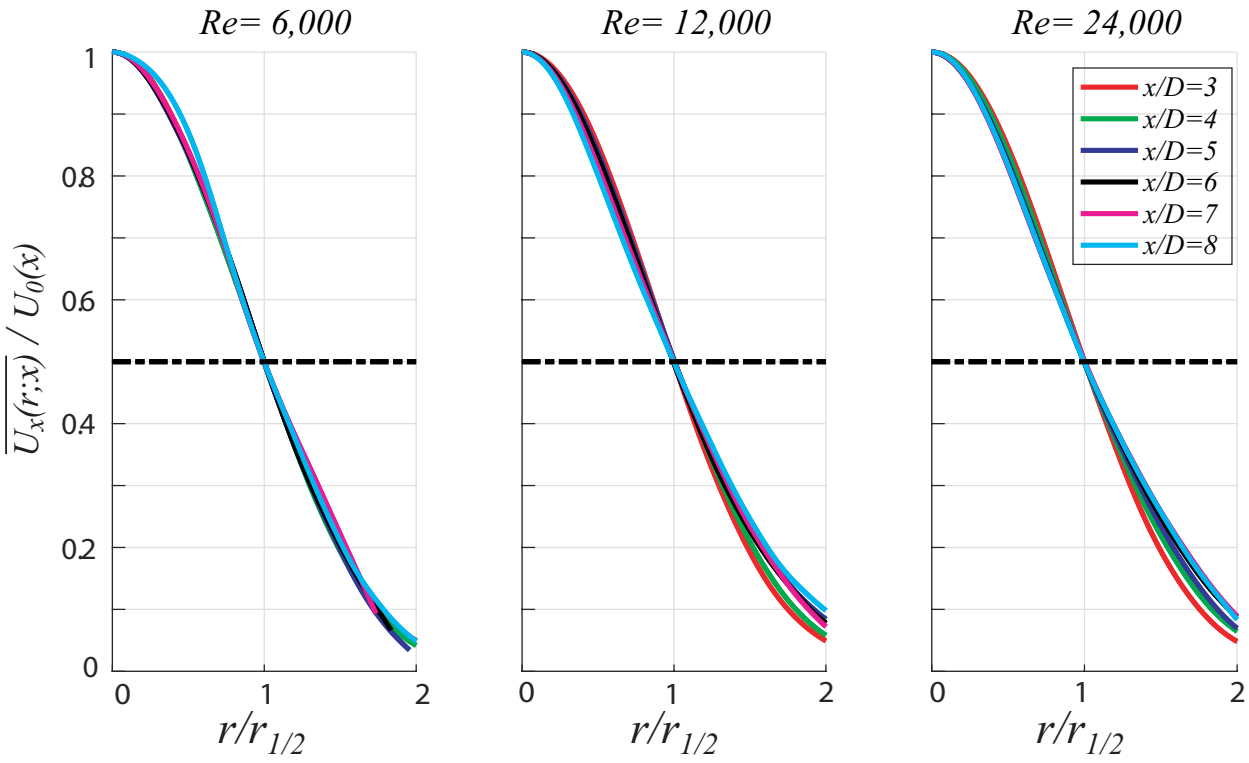

Figure 3.7: PIV Average velocity profiles in homogeneous water jets. Flows 14, 15 and 16.

3.2 Curvature Analysis

To be prepared for segmentation, images went through a number of pre-processing steps. During the capture process, illumination was done so as not to saturate the intensity value. This resulted in the intensity values existing in the lower half of the range. To study the edges of the features consistently between frames, an intensity scaling was implemented. The raw image is normalized by the maximum intensity value found in the image. This normalized image was then scaled by 250, corresponding to 98% of the full 8-bit greyscale range.

$$\mathcal{M} = max[I_{raw}] \tag{3.1a}$$

$$I_{norm} = \frac{I_{raw}}{\mathcal{M}} \tag{3.1b}$$

$$I_{scaled} = 250 \times I_{norm} \tag{3.1c}$$

As seen in 3.8, the contrast of the image was increased. This process does not attempt to address any non-uniformity in the spatial illumination. Then, the scaled images underwent the Canny edge detection process ([Canny(1987)]). The scaled image is first smoothed through a 5×5 Gaussian convolution kernel to arrive at smoothed images I_f in order to reduce the occurrence of noise-induced false edges. A sample of the smoothed images is shown in figure 3.9(a). The round Sobel edge detection operation ([Sobel & Feldman(1968)]) is carried out on the filtered image, I_f, which employs a centered finite difference approximation, S_h and S_v, for the first derivative in the vertical and horizontal directions to calculate image gradient. The gradient vector $\mathbf{G}$ in the filtered image are calculated via convolution as, respectively,

$$\mathbf{G} = (G_h,\ G_v) = (S_h,\ S_v) \circ I_f. \tag{3.2}$$

Finally, the magnitude I_g and the direction Θ of the image gradient vector are constructed as, respectively,

$$I_g = |\mathbf{G}| = \sqrt{G_h^2 + G_v^2} \quad \text{and} \quad \Theta = \operatorname{atan}\big(G_v/G_h\big). \tag{3.3}$$

This image gradient magnitude I_g is used to determine the locations of edges in an image, a sample of which is shown in figure 3.9(b). The direction of the gradient vector Θ is used for the non-maximum suppression process. The angle Θ is rounded to the closest 45° increment: i.e. 0°, 45°, 90°, or 135°. At a given pixel, the neighbors in directions perpendicular to the gradient direction are checked. If the pixel's gradient magnitude is greater than those of its neighbors, it is preserved and the neighbors are negated, or vice versa if the opposite occurs. The image gradient was binarized using the Otsu thresholding method [Otsu(1979), Sezgin & Sankur (2004)]. The Otsu thresholding method is an easily implemented cluster-based algorithm which selects threshold levels from the histograms of image segments, maximizing the separability of the resultant classes in grey levels. The images are then skeletonized through a morphological thinning process as discussed in [Jang & Chin(1990)], a sample of which is shown in figure 3.9(c), along with a detailed segment in frame (d). These edges are further examined to reject branches and segments shorter than 10 pixels. The resulting *edge image* is used for curvature analysis below, a sample of which is shown in figure 3.10 for the water jet at $Re = 6.22 \times 10^3$. For analyzing the curvature of the segments, the curves were parameterized by their $[x, y]$ position, as a function of the position along the length of the segment, s, beginning at the initial pixel, P_0, of the edge-curve $s(P_0) = 0$ or $s(x_0, y_0) = 0$. The

value of s was used to parameterize both the x_n and y_n for a given pixel, P_n. Distances between each of the following pixels, in order, was calculated:

$$ds_n(P_n) = ds(P_{n-1} - P_n) = \sqrt{(x_{n-1} - x_n)^2 + (y_{n-1} - y_n)^2} \tag{3.4}$$

Note that $ds_n = 1$ or $\sqrt{2}$ pixel. This definition of s leads to non-uniformity in the spacing between the values of s_n.

$$s_n = s(P_n) = \sum_{i=0}^{n} ds_i(P_i) \tag{3.5}$$

Per curve segment, a vector of these discrete (x_n, y_n) is constructed. Each of these was treated as a sampling of the function:

$$\mathbf{X}(s_n) = (X(s_n), Y(s_n)) = (x_n, y_n) = \mathbf{x}_n \tag{3.6}$$

at non-uniform sampling points along the length s.

The size of the analyzed edge curve segments range from $\mathcal{O}(10)$-$\mathcal{O}(10^2)$ data points in length. The position data innately has noise related to the discretization of a finite resolution image. A cubic smoothing spline is used to fit $\mathbf{x} = (x, y)$ with respect to position along the length of the segment. The process allows the splines to depart from the data points with a weighted penalization, trading off between the smoothness of the function versus the approximation of the data points' values by the curve. This is accomplished by finding $(\mathcal{X}, \mathcal{Y})$ that minimized the functionals $(\mathcal{L}_x, \mathcal{L}_y)$

$$(\mathcal{L}_x, \mathcal{L}_y) = p \sum_i \left[(x_i - \mathcal{X}(s_i))^2, (y_i - \mathcal{Y}(s_i))^2\right] + (1-p) \int \left[\left(\frac{d^2\mathcal{X}}{ds^2}\right)^2, \left(\frac{d^2\mathcal{Y}}{ds^2}\right)^2\right] ds, \tag{3.7}$$

This is a variant of the functional described in [Reinsch(1967)]. A smoothing parameter p, which ranges from $[0, 1]$, is employed to tune this trade off. In the case of $p = 0$, the result prioritizes smoothing, with a steep penalty for any oscillations, and returns a linear least square estimate of a fit; $p = 1$ returns an interpolating cubic spline. Using a cubic interpolating spline for $x(s_i)$ and $y(s_i)$ requires the spline to match the value at each point, which generates spurious oscillations of the curvature along a segment. For all segments $p = 1/2$ is used, which provides sufficient dampening of oscillations in the derivatives of the fit, while accurately capturing the path of the data points. The segment is then re-sampled at equispaced points along the lengths of the curve using the cubic smoothing spline fit. The number of points used to represent the segment is preserved.

The first and second derivatives, $(\mathcal{X}', \mathcal{Y}')$ and $(\mathcal{X}'', \mathcal{Y}'')$, with respect to s are calculated using 5 point centered finite difference kernels [Abramowitz & Stegun (1964)]. The two end points on each side of the segment were treated with a non-centered finite difference scheme, while matching the accuracy of the center scheme. The curvature along the segment is evaluated as

$$\kappa(s_i) = \frac{\mathcal{X}_i'\mathcal{Y}_i'' - \mathcal{Y}_i'\mathcal{X}_i''}{(\mathcal{X}_i'^2 + \mathcal{Y}_i'^2)^{3/2}} \tag{3.8}$$

Figure 3.11 illustrates the stages in analyzing segments for the homogeneous water jet of $Re = 6.22 \times 10^3$. Per segment, the discrete curvature measurement along its length is converted to

the measure of the curvature's magnitude in the segment, with respect to wavenumbers at which they occur. This is done by taking the discrete Fourier transform of the curvature vector for a segment $\kappa(s_i)$. The corresponding wavenumber is constructed with the inverse of the length between sampling points, Δs, with the number of sampling points, N. The value of Δs is constant per segment, as they are sampled at equispaced distances along the length of the segment.

$$k_j = j \times \frac{N}{\Delta s} \qquad 0 \leq j \leq \frac{N}{2} \tag{3.9}$$

$$\mathcal{K}_j = \mathcal{K}(k_j) = \mathcal{F}\big(\kappa(s_j)\big) \tag{3.10}$$

The amplitude of the curvature at a wavenumber is found by taking the length of the complex value of $\mathcal{K}(k)$ normalized by the length of the vector, N. If N is even, the highest mode is excluded.

$$\widetilde{\mathcal{P}}_j = \frac{|\mathcal{K}_j|}{N} \tag{3.11}$$

$$\mathcal{P}_j = \begin{cases} \widetilde{\mathcal{P}}_j, & j = 0 \\ \widetilde{\mathcal{P}}_j \times 2, & 0 < j \leq N/2 \end{cases} \tag{3.12}$$

$\mathcal{P}_j$ corresponds to the amplitude of the curvature signal at the wavenumber, k_j. This process is done for each segment in the image that exists in the region between $1 \leq x/D \leq 8$ downstream. Per homogeneous water jet run, the results reported are a collection of all segments captured through all the images used for that run.

Figure 3.12 shows the results of the curvature density calculations of the turbulent water jets. The curvature $|\kappa|$ is scaled with the local Kolmogorov wavenumber $k_\eta(x)$ and plotted against the wavenumber, which is nondimensionalized again with the Kolmogorov wavenumber and $Re^{3/4}$. Recalling the definition in equation 2.12, the wavenumber scaling simply amounts to writing kD. The data are sorted into 35 wavenumber bins and subsequently averaged to construct the curvature histograms of Fourier amplitudes for each Reynolds number in the figure. The averaging of curvature density about a wavenumber is done to construct 35 datum points per flow rate. The raw data are organized in respect to wavenumber; equal number of values are averaged. The horizontal dashed line at $|\kappa|/k_\eta = 0.10$ in the figure marks the boundary of where the period of the spectral component is spread over 6 or fewer pixels in images. Resulting trends below this threshold should be viewed with caution.

The packing of the data gives insight into which wavenumbers the results were clustered around. Highest amplitudes occur at lower wavenumbers: those easily picked out by the naked eye in the flow images. The figure also illustrates the prevalence of high wavenumbers with relatively small Fourier amplitudes. Thus, along the length of segments in figure 3.10, low wavenumbers are manifested as high amplitude curves and high wavenumbers as low amplitude curves. Beyond the dominant amplitudes, the curvature amplitudes at higher wavenumbers fall off at a rate of -7/3 and at the highest wavenumbers at a rate of -5/3 is observed.

The analysis of these results indicates that curvatures are relaxed at rates dependent on their magnitude, with higher curvature features not being sustained as long as lower curvature features. Smaller eddies decay faster than larger eddies, a quintessential feature of turbulent flows. These results, in general, may suffer from quantification noise introduced by the resolution of the image, where a line must be represented as discrete steps in pixel locations. The smooth spline fitting was used to inhibit this source of error, but occurrences of cusps in the segments as they are

detected by the algorithm may not be physically indicative of the continuous features. A scheme to validate or reject cusps would be desirable to help mitigate inaccuracies in the edge tracing. The spatial curvature measurements per segment also do not necessarily follow periodic boundary conditions at the end points, resulting in an occurrence of aliasing in the results of the DFT. The windowing applied to these signals, depending on the aggressiveness of the windowing, resulted in trend lines seen in figure 3.12 which were biased to approach the DFT result of the window used. Comparing results from the curvature signals that underwent a Hanning windowing to the results from un-windowed curvature signals lead to no immediate change in the trends; this allowed for simplification in presenting the results without windowing.

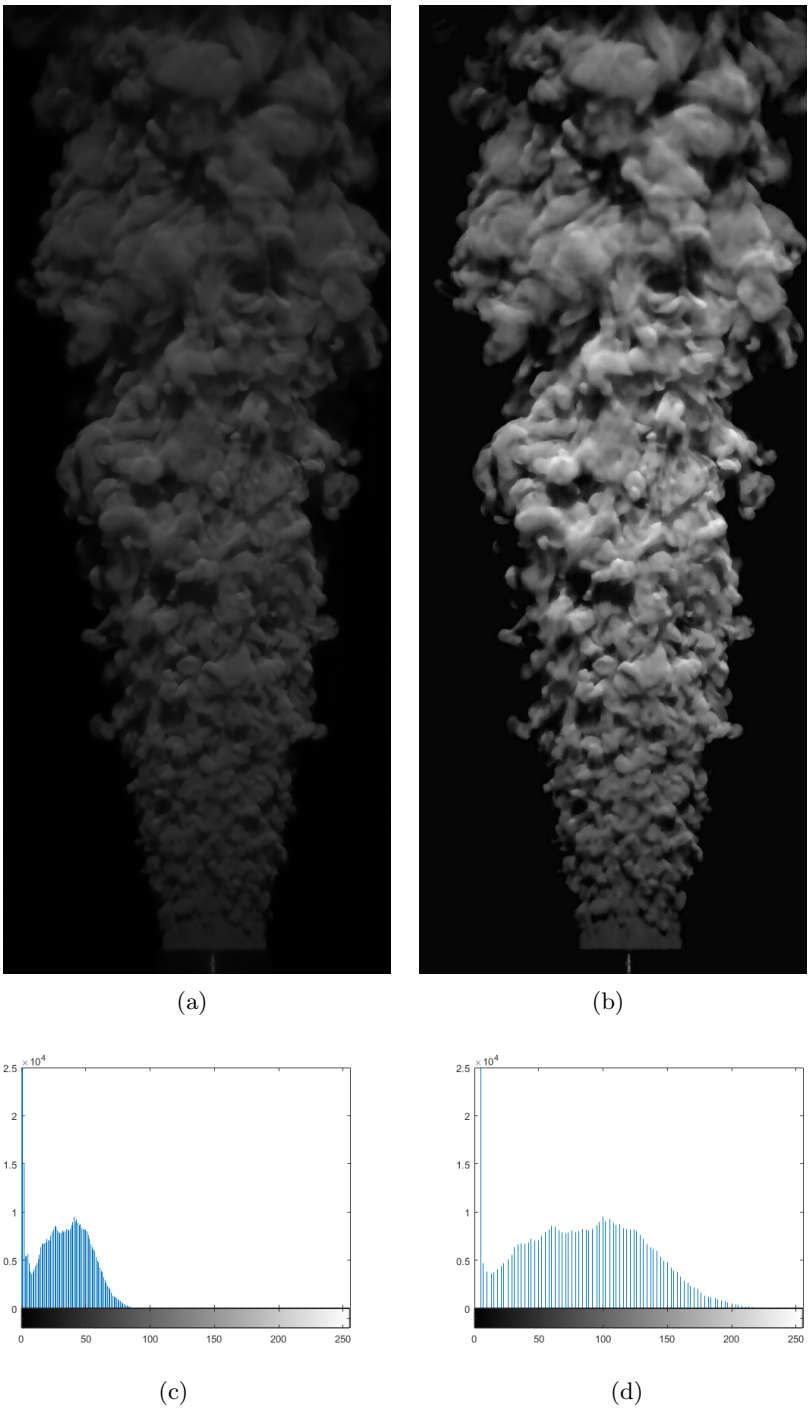

Figure 3.8: Sample homogeneous jet image demonstrating intensity adjustment: Re = 1.20×10^4 (a) raw image as recorded, (b) scaled to 98% of full range, (c) corresponding histogram for the intensity of the raw image, and (d) corresponding histogram for the scaled image

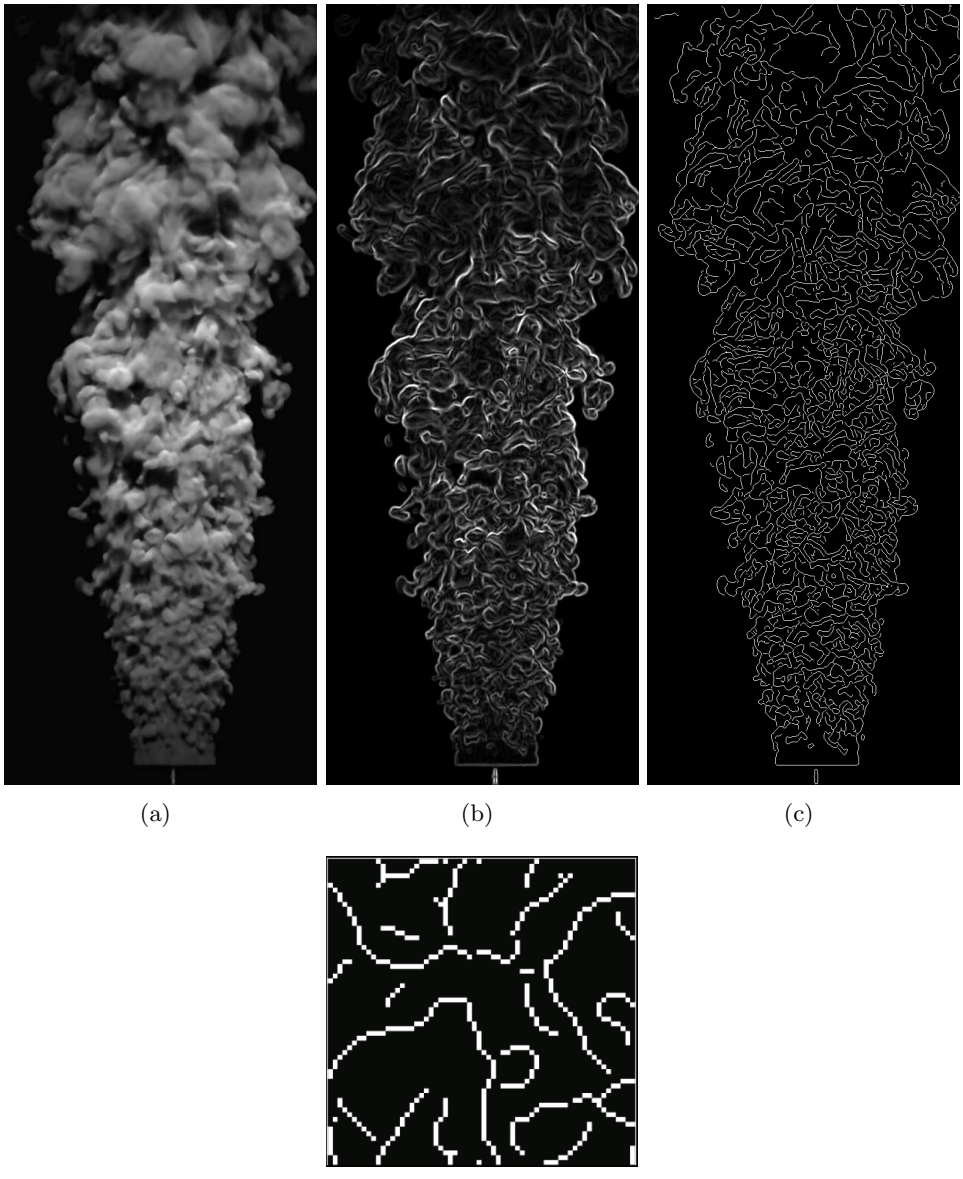

(a) (b) (c)

(d)

Figure 3.9: Sample homogeneous jet image demonstrating edge detection process: $\mathrm{Re} = 1.20 \times 10^4$. (a) a sample image from the video sequence after Gaussian filtering, (b) its intensity gradient magnitude, (c) thinned edges, and (d) details of edges from (c).

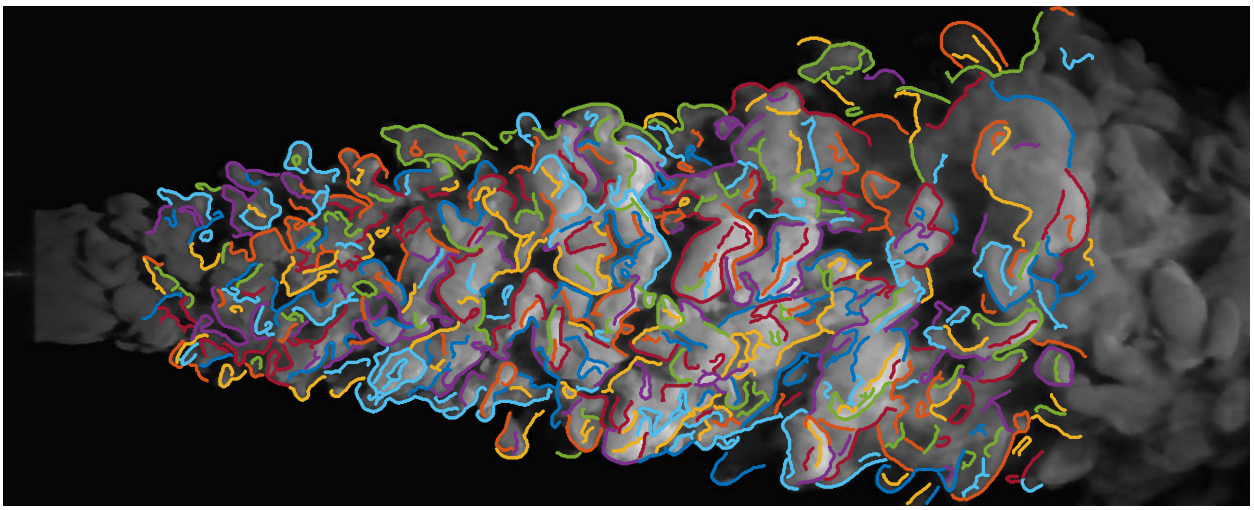

Figure 3.10: All curves found after the segmentation process for homogeneous turbulent jet of $Re = 6.22 \times 10^3$. Color is added to show segments.

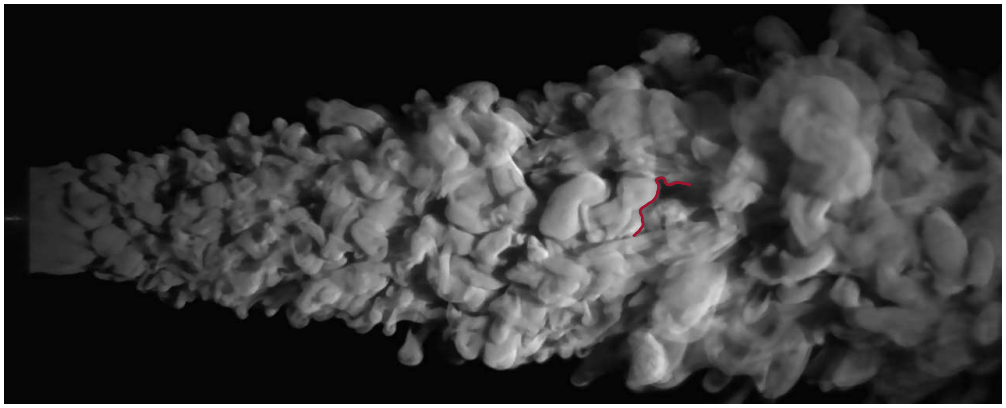

(a)

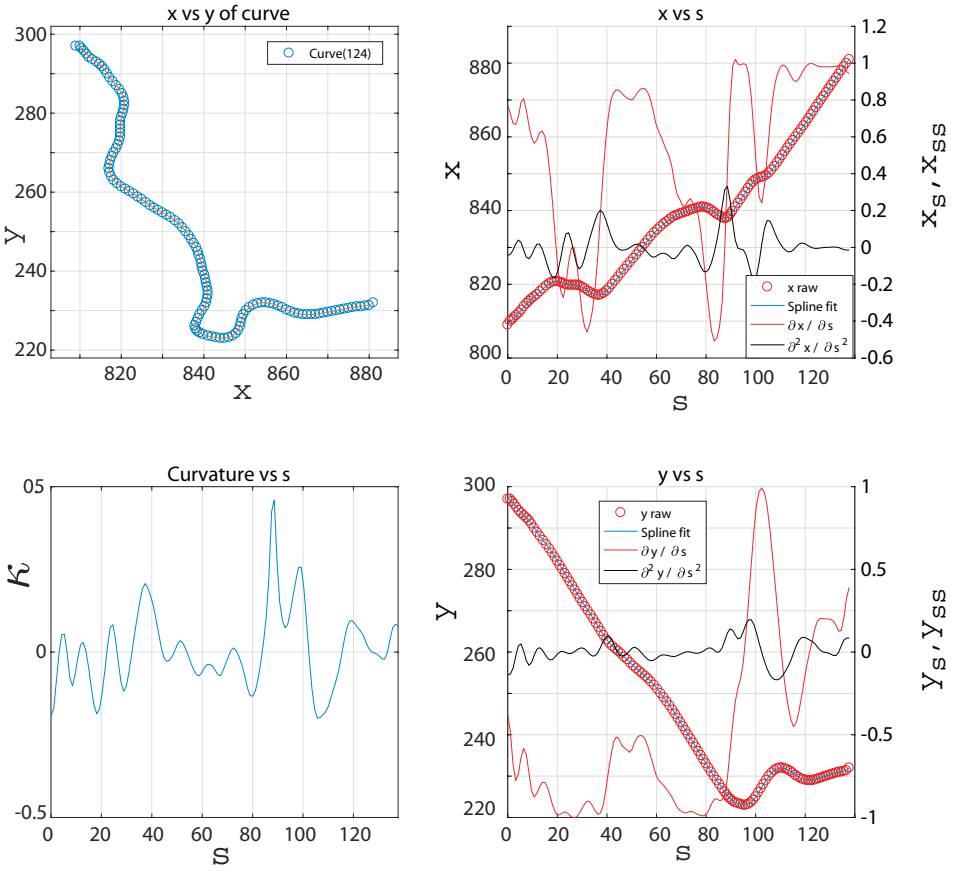

(b)

Figure 3.11: Sample homogeneous jet image demonstrating curvature analysis for Re $= 6.22 \times 10^3$ (a) Full view of image with a sample edge segment and (b) analysis. The edge segment in (a) is reflected horizontally and reproduced in the first frame of (b). The second and third frames (clockwise) of (b) show $x(s$ and $)y(s)$, and spline fits and their derivatives, respectively. Finally, the last fame shows the curvature from equation 3.8, along the length of the edge segment above it where one can easily match the corresponding features in both frames.

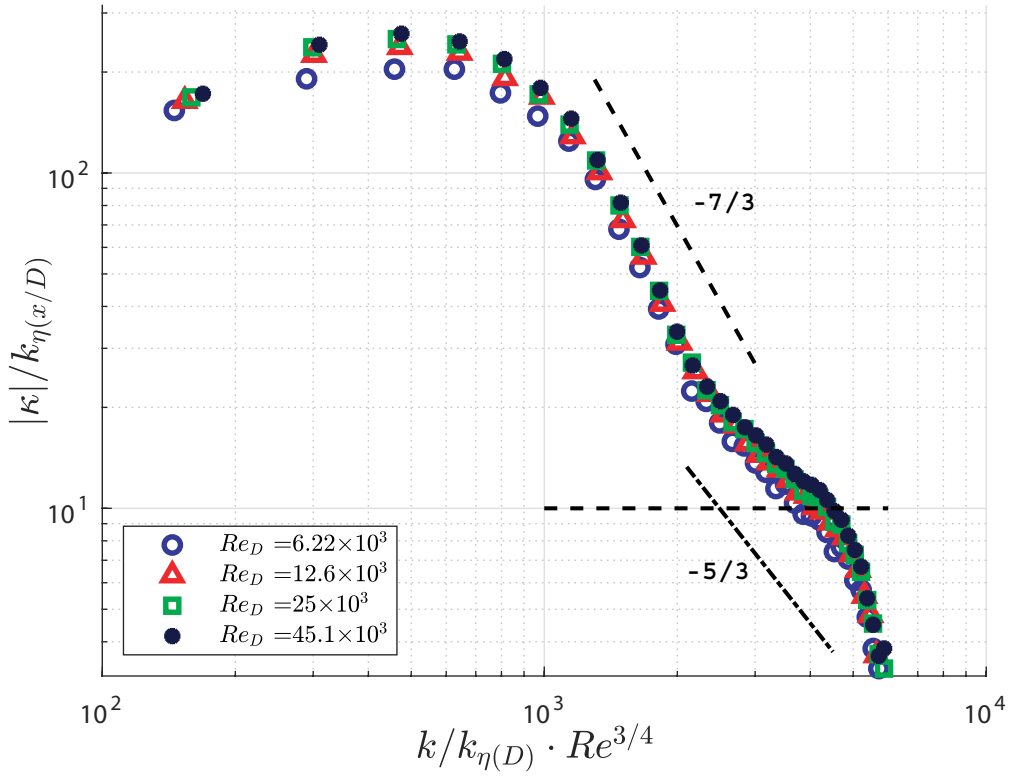

Figure 3.12: Curvature Density Spectrum $|\kappa|$ $[m^{-1}]$ with respect to wavenumber normalized by the pipe Kolmogorov wavenumber for the homogeneous jet experiments investigated. The horizontal dashed line corresponds to soft cut-off to the spatial resolution of the curvature signal.

3.3 Interfacial Length Scale

Interface length scales are extracted from the jet images. The images, however, suffer from spatially inhomogeneous illumination along the axis of the jet. To mitigate any bias from the waning illumination intensity, a contrast limited adaptive histogram equalization (CLAHE) technique is employed ([Pizer *et al.*(1987)]). The process consists of discretizing the image into a grid of tiles. These sub-regions form a mosaic of the original image, with divisions allowing 10 tiles along the length of the image and 4 across—tiling the image from 512×1280 pixels into a 10×4 array of 128×128 pixels square tiles. The size of the tile region is a parameter of the method that weighs which scales will have their contrast enhanced. For scales smaller than the tile, contrast is enhanced; for scales larger than the tile, contrast is reduced.

A histogram equalization was done per tile, matching to a Rayleigh PDF. Matching to a Rayleigh distribution has been found to be most suited to underwater imagery in image-based measurement literature [Eustice *et al.*(2002)]. The transform function per tile is faithfully valid for the center pixel of the tile. Figure 3.13 shows an illustration of the tiles separated by dashed green lines; the white dots indicate the center pixel of a tile. A bilinear interpolation was utilized to transform the remaining pixels for the internal tiles. A histogram equalization per pixel in the image provides a more faithful approach. However, this adds an appreciable amount of computational cost with no significant benefit to the resulting image after the equalization, even with current (2021) computing power of a workstation. Figure 3.14 shows sample results after the CLAHE operation on the homogeneous water jet runs at different Reynolds numbers. This adaptive histogram equalization returns noisy results when, within the tile region, the intensity values are homogeneous. The tile's histogram contains a strong peak, and the transformation function will map a narrow range of pixel values to the whole range of the result image. This causes the adaptive histogram equalization to amplify minute amounts of noise in the homogeneous regions of the image. This is notably seen in figure 3.15, where 75% of the pixels in the tile have an intensity value of 0. A stark difference can be observed when comparing against figure 3.16, where the intensity values of the pixels fall within an intensity range of ≈ 100. The interrogation region used to analyze the interfacial length scale, 3.17(c), marginally incorporates regions where noise amplification is seen. The auto-correlation reduces the weight that these fringe edges have on the final analysis.

Figure 3.18 illustrates the procedure to extract length scales from the images. The sample interrogation tile in frame (a), 256×256 pixels, is at $x/D = 3.42$ downstream from the discharge orifice of the jet for $Re = 25.0 \times 10^3$. The intensity field $I(x, y)$ is shown in frame (b) in isometric form. To prevent leakage in the 2D signal as it is taken into the Fourier domain, a 2D Tukey window (tapered cosine window) is applied to the interrogation region to construct a periodic boundary. This is constructed by extending the 1D Tukey window, $w(x)$ [Tukey(1967)]. The taper of the window is set to 64 pixels from the center of the interrogation region. The matrix product of the 1D Tukey window with its transpose is used as the 2D Tukey window, $W(x, y)$.

$$W(x, y) = w(x)\ w^T(y) \tag{3.13}$$

The window, $W(x, y)$, was then applied to the interrogation region, $I(x, y)$ through the element-wise multiplication (Hadamard/Schur product)

$$I_w(x, y) = W(x, y) \circ I(x, y) \tag{3.14}$$

Thus windowed image intensity is now $I_w(x, y)$.

The windowing process reduces the largest length scale that can be detected, restricted by the size of the window. When the radius of the jet is contained in the interrogation region for the initial steps, all scales that exist within are able to be estimated. Interrogation regions further downstream of the jet do not capture the whole jet profile, preventing the detection of features comparable in scale to the full jet diameter. The Tukey windowed form of the intensity data in figure 3.18(b) is shown in figure 3.18(c).

The auto-correlation of the windowed region is calculated using a $2D$ DFT

$$R(\bar{\mathcal{X}}) = \mathcal{F}^{-1}\big(\mathcal{I}(\bar{k})\mathcal{I}^{*}(\bar{k})\big), \tag{3.15}$$

where $\mathcal{I}(\bar{k}) = \mathcal{F}\big(I_w(\bar{x})\big)$ and $\bar{k} = [k_x, k_y]$ is the wave vector. The auto-correlation $R(\bar{\mathcal{X}})$ is shown in figure 3.18(d). The second derivatives of $R(\bar{\mathcal{X}})$ at the center peak are used to estimate the streamwise and cross-stream length scales (λ_x, λ_y), respectively. These derivatives are evaluated using a centered 5-point finite difference kernel [Abramowitz & Stegun (1964)]. The length scales are written as

$$(\lambda_x, \lambda_y) = \left(\left[\frac{1}{2}\left|\frac{\partial^2 R(0,0)}{\partial \mathcal{X}^2}\right|\right]^{-\frac{1}{2}}, \left[\frac{1}{2}\left|\frac{\partial^2 R(0,0)}{\partial \mathcal{Y}^2}\right|\right]^{-\frac{1}{2}} \right), \tag{3.16}$$

which amounts to fitting two orthogonal osculating parabolas at the peak $R(0,0) = 1$ in figure 3.18(e). The average of the longitudinal and transverse length scales,

$$\lambda = \frac{1}{2}\big(\lambda_x + \lambda_y\big) \tag{3.17}$$

is reported to give insight into the growth trend of the structures in the case of the homogeneous water jet. The 256×256 pixels interrogation tiles were stepped along the axis of the jet in 64 pixel increments, the first one centered at $x/D = 3.42$, and the last one at $x/D = 7.54$, for a range of $Re \approx 6000 - 45000$.

Figure 3.19 shows the interfacial length scale for the water jets: the length scale ratio λ_x/λ_y in frame (a) and the averaged interfacial length scale λ in frame (b). The ratio λ_x/λ_y , extracted from the zero crossings of the osculating parabolas from equation (3.16) is effectively unity—regardless of x/D and Reynolds number, which attests to the isotropy at the interface. Figure 3.19(c) shows the ratio of the interfacial length scale to the local Taylor microscale, $\lambda/\tilde{\lambda}_g$, where the local Taylor microscale $\tilde{\lambda}_g$ is estimated from the RMS fluctuations of shear strain rates deduced from the PIV measurements [Pope(2000)]. In figure 3.19(a), a monotonic increase with x/D of the averaged interfacial length scales is seen for all Reynolds numbers. The rate at which these scales increase is seen to be inversely related to the jets' Reynolds number. The ratio, $\lambda/\tilde{\lambda}_g$, is uniform over the measurement domain and monotonically increases with Reynolds number at a diminishing rate.

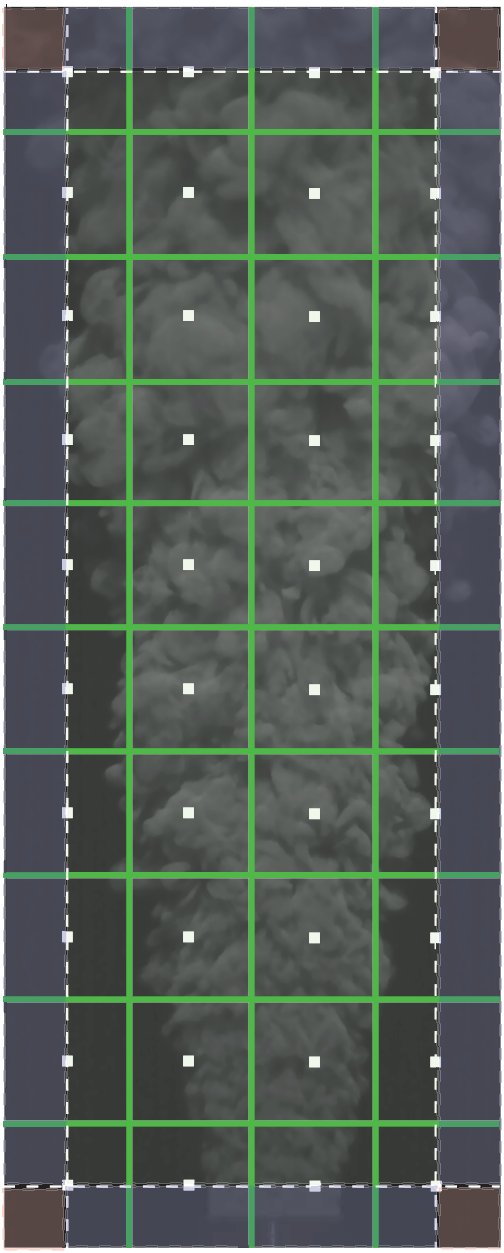

Figure 3.13: The white dot denotes the pixel where the histogram equalization transform is calculated using the 128 pixel region. Pixels in the blue region use a linear interpolation of the neighboring transforms and the red regions rely only on the nearest transform neighborhood. The center region uses a bilinear interpolation method for estimating the transform of the neighboring pixels.

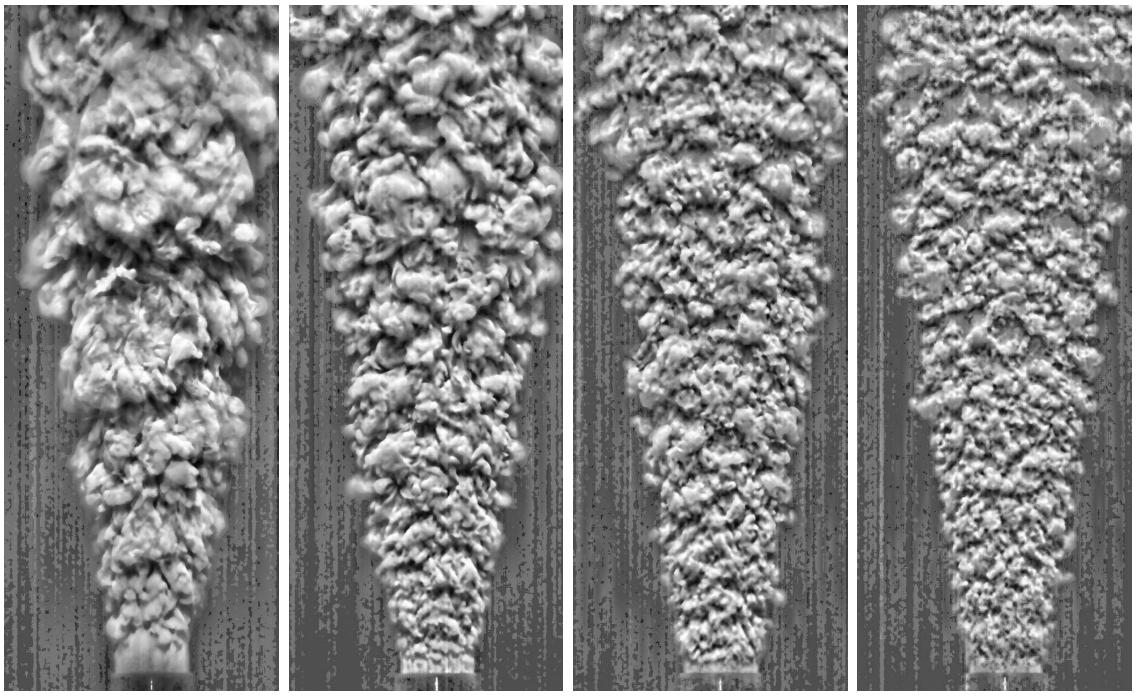

(a) $Re = 6.22 \times 10^3$ (b) $Re = 12.6 \times 10^3$ (c) $Re = 25.0 \times 10^3$ (d) $Re = 64.5 \times 10^3$

Figure 3.14: Sample images of CLAHE on fluorescent homogeneous water jets.

(a) Raw Image Tile

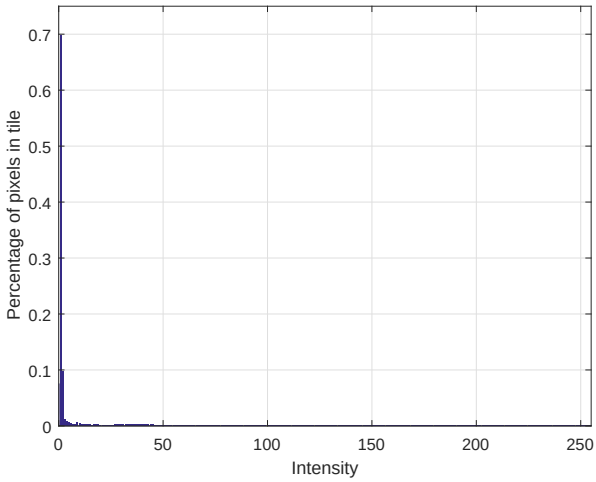

(b) Raw Image Tile Histogram

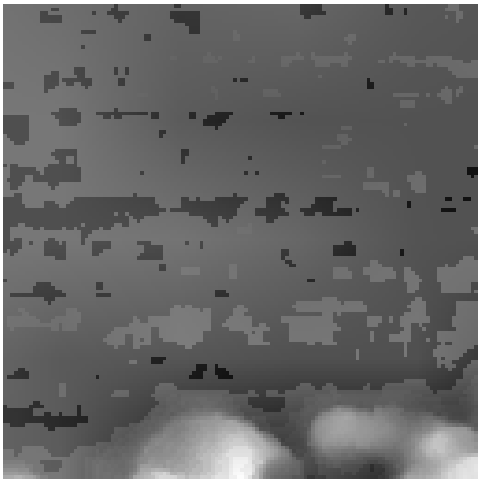

(c) Equalized Image Tile

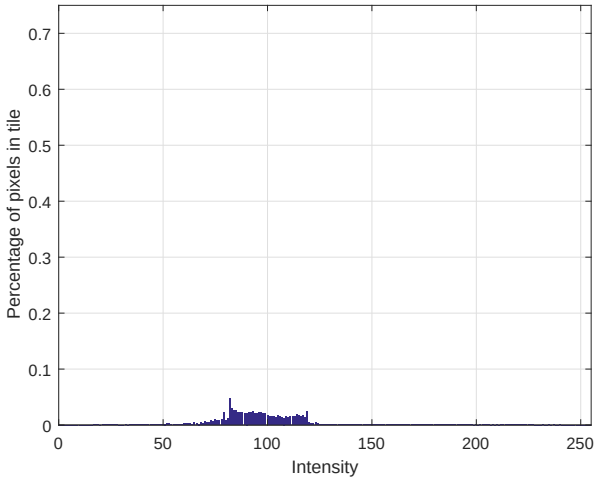

(d) Equalized Image Tile Histogram

Figure 3.15: Example tile processed during CLAHE with undesirable outcomes

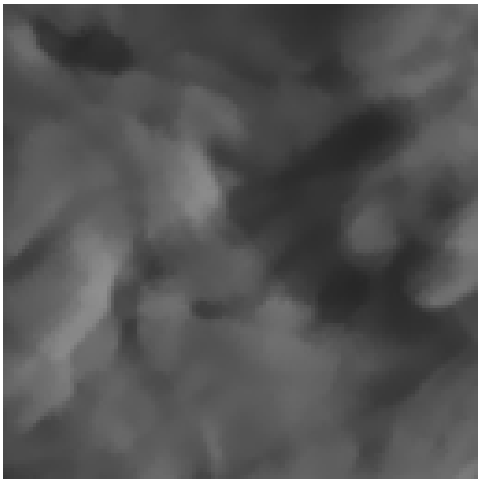

(a) Raw Image Tile

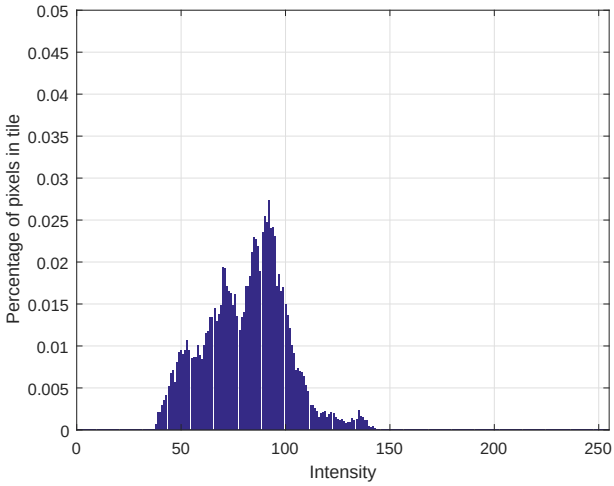

(b) Raw Image Tile Histogram

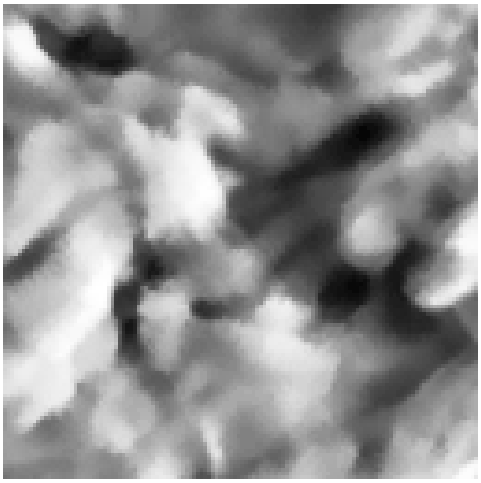

(c) Equalized Image Tile

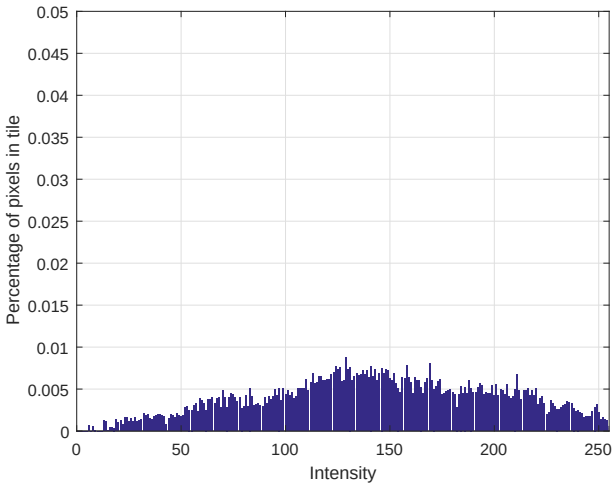

(d) Equalized Image Tile Histogram

Figure 3.16: Example tile processed during CLAHE with desirable outcomes

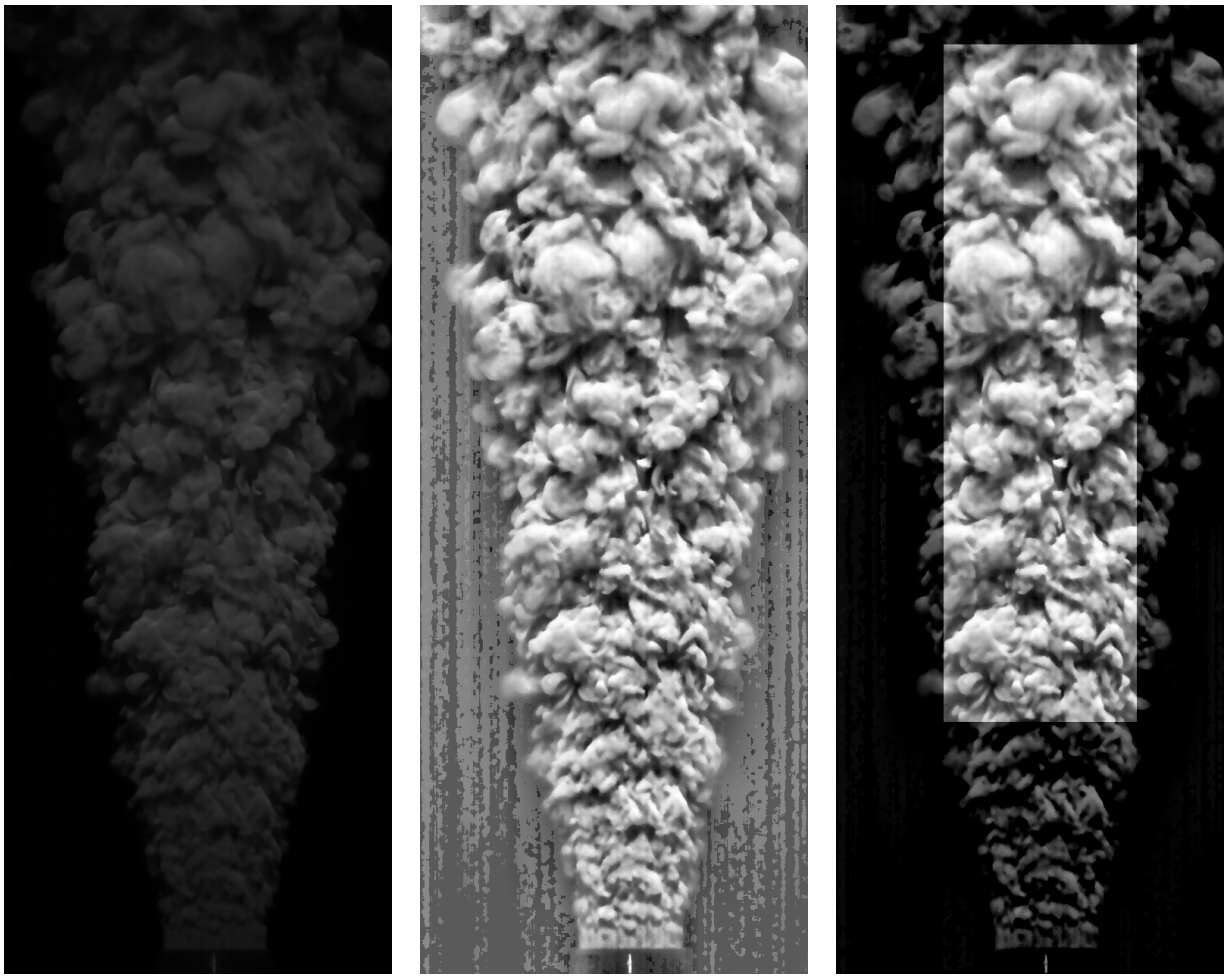

(a) Raw Image

(b) CLAHE'd Image

(c) Interrogation Path - Brighten Rectangular Region

Figure 3.17: Image comparison after the CLAHE Process

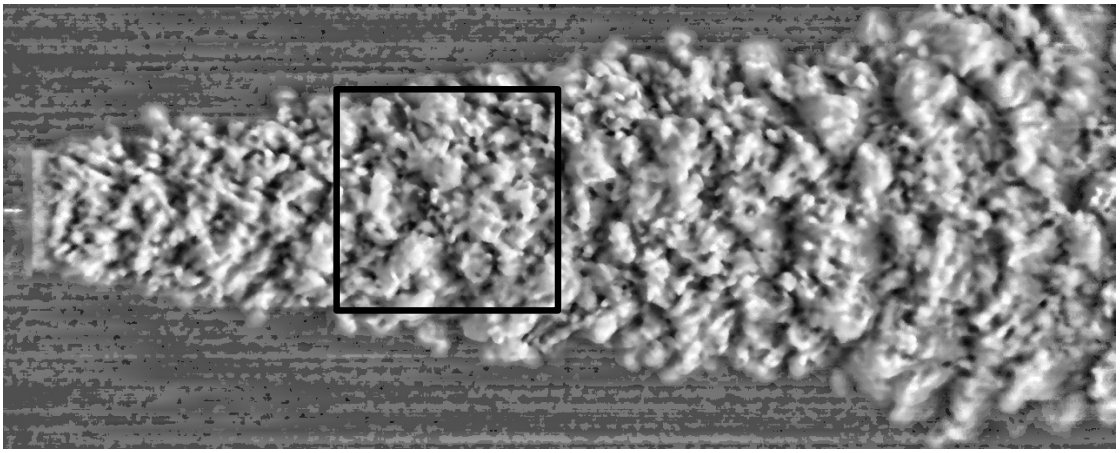

(a)

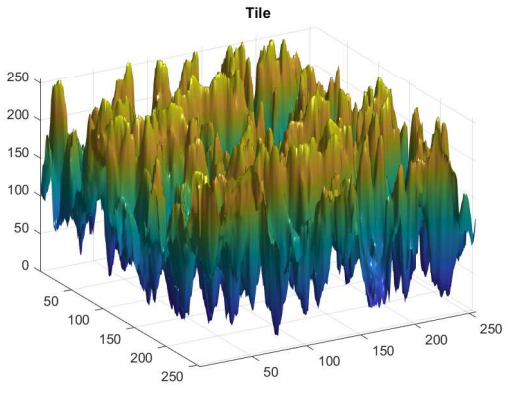

(b)

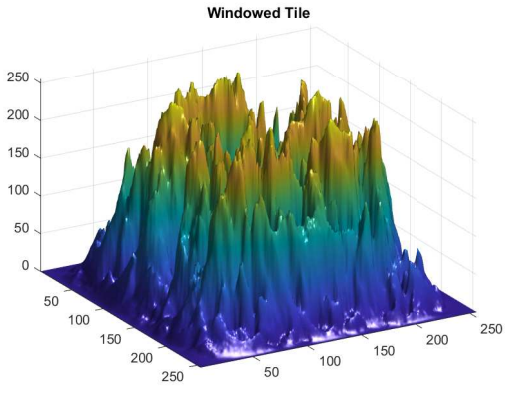

(c)

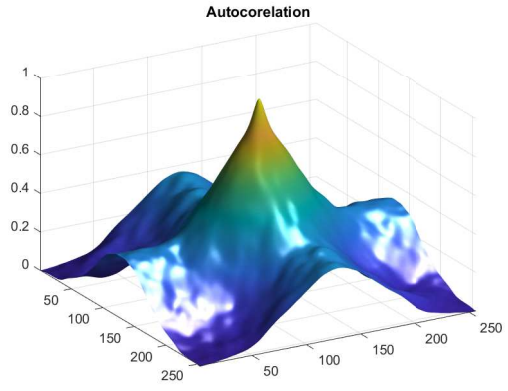

(d)

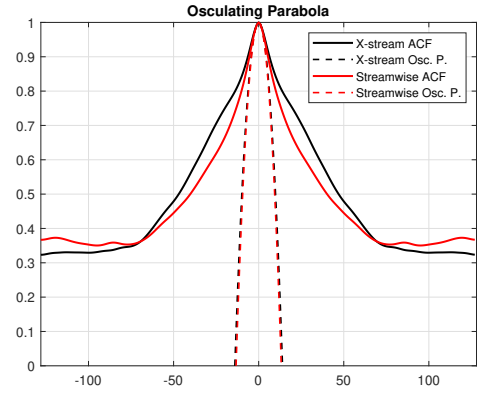

(e)

Figure 3.18: Processing steps for the interrogation region of the homogeneous jet at $Re = 25.0 \times 10^3$ at $x/d = 3.42$, (a) a sample interrogation region along the jet, (b) raw intensity array, (c) (c) interrogation tile's intensity values after 2D Tukey windowing , (d) the results of the 2D autocorrelation of the windowed tile, and (e) the cross-stream(red dashed) and stream-wise(black dashed) osculating parabola to the autocorrelation (solid with same respective color)

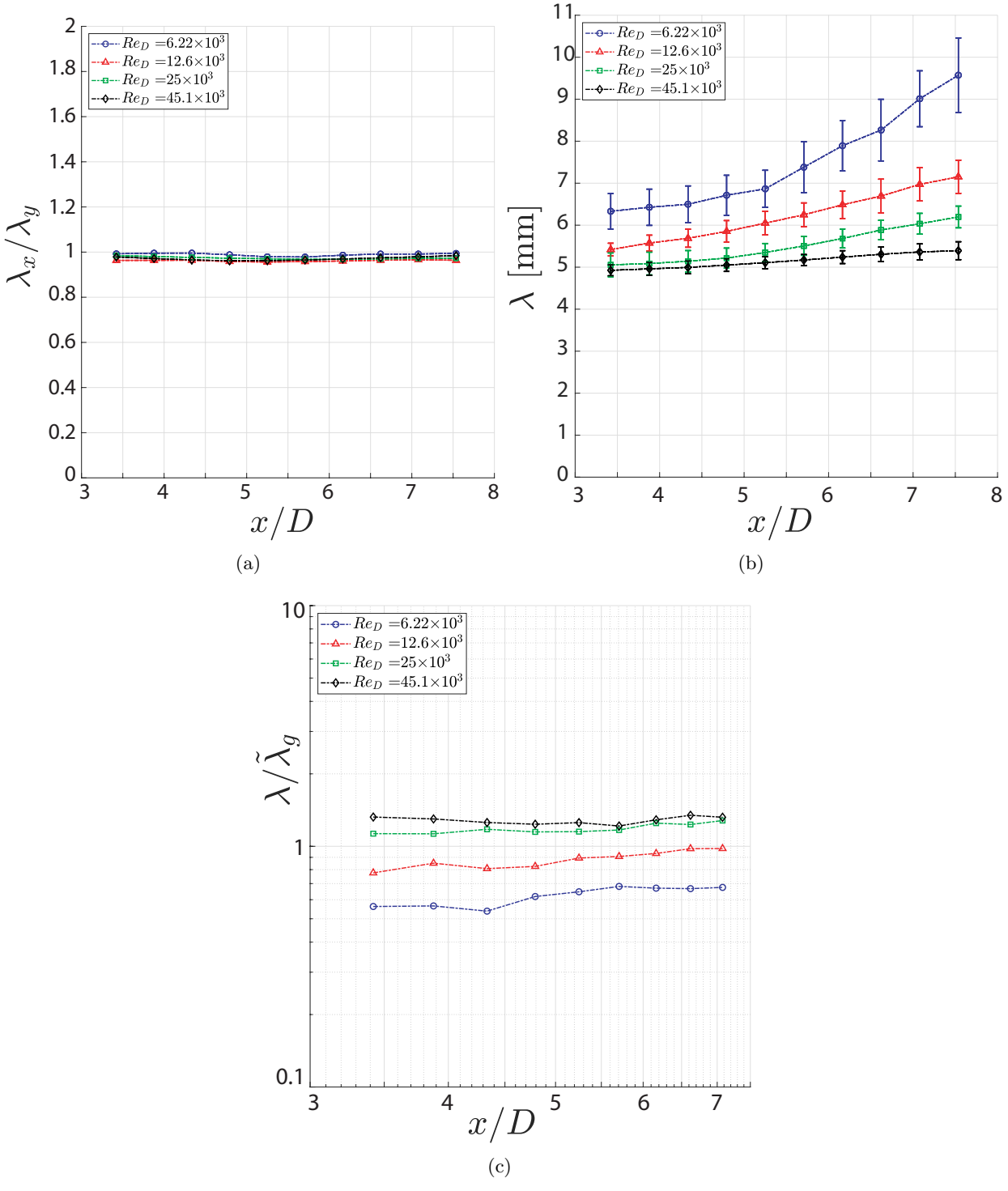

Figure 3.19: Interfacial length scale results for water jet: (a) length ratio λ_x/λ_y, (b) mean length scale $\lambda = (\lambda_x + \lambda_y)/2$ and (c) interface length scaled with the Taylor microscale $\lambda/\tilde{\lambda}_g$.

3.4 Internal length scales

Schlieren visualization provides an illustration of density fluctuation by refracting light. Images produced using this method provide a range of scales to be observed, each layered upon one another. When viewed in sequence, the human eye can separate and faintly observe features moving as they advect along at various speeds. It is difficult, however, to isolate the motion of features with the eye. The work presented here describes an approach for extracting more information from established image-based measurement techniques for investigating turbulent flows, predominately focused on high-speed schlieren video recordings of turbulent jets. It is difficult to isolate scales and motion in a schlieren recording because it captures the superposition of density variations. To address this challenge, it is helpful to temporally filter the signal using a Pixelwise Time Filter(PixTiF). The filter chosen for this application is a band-pass filter to isolate features moving at a particular rate. When features are isolated according to a desired band, the scales associated with the features are quantified. This process tries to provide a framework for extracting quantifiable results from a measurement technique that has been primarily qualitative for turbulent flows. PixTiF is similar to to the temporal filtering treatment in [Chitanont *et al.*(2015)] as applied to schlieren images to visualize sound waves of a known frequency. Chitanont's work used both temporal and spatial filters to isolate known sound wave patterns weakly present in the raw schlieren images. Spatial filtering is not discussed in the work presented here because the very thing being investigated is the unknown ranges of scales within the turbulent jets.

The length scale of a visible feature in a flow field can be estimated using image-based measurements. When looking at greyscale images, any feature traversing a point corresponding to a pixel in the captured image will cause the intensity of that pixel value to fluctuate. As a feature moves through it, a pixel's intensity value will vary: transitioning from the initial intensity of the local background, to the value at the edge of the feature, to the values along lines through the feature, to an edge intensity value of the feature, before reverting back to the local background value. In simplified terms, a single pixel's temporal recording of the feature's intensity can be said to loosely resemble a Tukey window profile. The temporal duration of the pulse is tied to the persistence of the feature at that pixel location. Let us assume the feature was primarily experiencing advection with minimal deformation for the time scale of it traversing the pixel location. The duration of the square pulse will be dependent on the velocity at which the feature was being advected, along with the length scale of the line segment of the feature that was observed by the pixel.

In opaque turbulent jet experiments, features at the edge of the dyed shells can be seen. As the outer shells move, faster motion can be seen beneath, towards the core of the jet. To effectively quantify the flowrate using surface feature motion, the ejected outer shells need to be considered because they conceal the motion of rolling eddies that can be used to estimate the velocity profile and flowrate of the jet. Being able to determine flowrate despite the obscuring influence of surface features would be invaluable to first responders of accidental oil leaks, where ROV video recordings may be the only measurement available to them. Additionally, quick flowrate measurements allow first responders to assess the amount of containment or dispersive resources they would need to deploy to mitigate environmental and economical damages. PixTiF could effectively remove the signatures of the slower moving outer shells to provide easier access to quantify the features that would be more pertinent to track.

3.4.1 PixTiF (Pixelwise Time Filter)

PixTiF is a processes that temporally filters an image deck. Comparative metrics of time based between CPU to GPU processing were tested on a desktop with an i9-9900K with 64GB of DDR4 3200MHz and a NVDIA RTX 2070.

Within the image deck, the process treats a single pixel's intensity measurements in time as a signal. This time signal, independent of neighboring pixels, is taken into the frequency domain, through a discrete Fourier transform, to be filtered and returned back to the time domain, illustrated in figure 3.20.

The full image deck is held in RAM as an unsigned integer 8 3D array. The dimensions of the array correspond to the resolution of the image: nx and ny representing the width and height of the image in pixels, respectively. The width of the image is effectively aligned with the axis along the jet while the height is aligned with the radial direction of the jet. The depth of the array, nz, corresponds to the number of frames in the deck. The full recording length of $nz = 2048$ frames was used for each of the experimental runs presented. The raw image height of $ny = 512$ pixels was preserved, while the image width was reduced to $nx = 1024$ pixels.

Due to limited amount of memory tied to most commercial GPU, the PixTiF must process spatially discretized sub-decks of the original image deck to be tiled into a full image deck that has been temporally filtered. The sub-deck consists of square cuts of the image that maintain all the time content, $ns \times ns \times nz$. The value of ns is power of 2, which was chosen based on the memory limitations of the GPU. To process the image-decks for these experiments on a NVDIA RTX 2070, an $ns = 256$ was set to prevent running out memory on this device. A smaller ns can be selected for graphics cards with smaller available memory.

To prepare to filter the image deck, a band-pass kernel is constructed. A band-pass filter was used to isolate features moving with a corresponding frequency signature. The band-pass filter is represented by a Gaussian curve with a user-selected center frequency, f_c, and width, f_w, similar to the standard deviation of a normal distribution. The centers used are represented as percentages of the Nyquist frequency, f_c/f_{Nyq}, of the video recording; the width used was set to $f_w = f_{Nyq}/48 = f_{Nyq} \cdot 0.021$ of the bin range to the Nyquist frequency. This value was selected to minimize the overlap of frequency content between neighboring f_c/f_N values while maximizing the width to preserve as much of the signal being isolated as possible. Figure 3.35 illustrates the locations and width of the band-pass regions for the primary results discussed. In §3.4.7, results are presented illustrating the sweep of f_w tested and its impact on the results, or lack thereof. The filtering kernel is constructed once, as it is the same for all sub-decks in the image deck being processed.

$$\mathcal{G}(f) = \exp\left(-\left(\frac{f_c - f}{f_w}\right)^2 \right) \tag{3.18}$$

The filtering kernel is calculated for frequencies up to the Nyquist frequency bin, $nz/2$, then it is mirrored and appended, returning a 1D array nz values long. This 1D array is used to populate the $ns \times ns \times nz$ band-pass kernel. The kernel is constructed in the work-space using CPU accessible memory. Once completed, the filtering kernel is converted into a GPU array object.

The process then steps into a loop to iterate through sub-regions of the image space. Per iteration of the loop, the spatially discretized sub-deck is converted into a GPU array object. The discrete Fourier transform of the GPU sub-deck array is calculated in the array dimensions

corresponding to the time signal. The GPU array sub-deck, in the frequency domain, is element-wise multiplied with the GPU array filter kernel. The filtered sub-deck is returned to the time domain, through the use of the inverse discrete Fourier transform.

$$\tilde{I}_{i,j}(t) = \mathcal{F}^{-1}\Big(\mathcal{F}\big(I_{i,j}(t)\big) \circ \mathcal{G}(f)\Big) \tag{3.19}$$

The filtered array sub-deck, $\tilde{I}_{i,j}(t)$, is transferred from the GPU's memory to the local workspace, into CPU accessible memory. The filtered sub-deck is then allocated to its corresponding location in a pre-allocated filtered image deck array. The GPU array variables created in the loop are recycled, limiting the number of instances of unique arrays to avoid GPU memory limits.

The PixTif process is done to isolate features moving with certain speed in the image deck. GPU processing is leveraged to reduce the time required to complete the filtering process by $\mathcal{O}(10^2)$, including the conversion from the local work-space to the GPU's memory.

3.4.2 Qualitative Observations

Figures 3.21-3.23 show sample frames for Flows [30, 32, 35] at Reynolds number 0.62×10^4, 2.04×10^4 and 4.56×10^4; presenting a raw schlieren frame along with the frame after being filtered using $f_c/f_{Nyq} = 0.125$, 0.25, 0.375, and 0.50. The intensity values of the filtered images have been shifted and stretched to fill the 8-bit range, as in Eq.3.1. Video sequences of these images provide a greater depth of visualization, but are not shown here due to the size restrictions of this submission.

Figure 3.21(a) shows the sample set of images for the $Re = 0.62 \times 10^4$ run. Throughout figure 3.21(b-e), a cascade of scales are seen separated based on the filter center, with larger scales noted at the lower f_c values and finer features noted at the higher f_c values. A sequence of frames shows features translating with higher apparent speed for the higher f_c values. At lower f_c values, the motion of the features can be tracked as they travel downstream. It should be noted for the lower Reynolds number flows, including $Re = 6,200$, the motion at higher f_c should be observed cautiously. For example, in figure 3.21(d-e), motion appears as shimmering fluctuations when compared to the more coherent motion of the lower f_c, seen in figure 3.21(b-c).

Figure 3.22(a) shows the sample set of images for the $Re = 2.04 \times 10^4$ run. This shows a similar trend of the visual scales decreasing for increasing filter center. When compared to the lower Reynolds number flow at the same f_c, the higher Reynolds number flow has visually larger features at every f_c. At lower f_c values, the motions of the features are still clear and can visually be followed for some distance downstream. The downstream motions of the features at higher f_c are more trackable when compared to the lower Reynolds number flows. The features no longer have a shimmering quality that was noted for the lower Reynolds numbers flows and the image has a better signal to noise ratio.

Figure 3.23(a) shows a sample schlieren image from the $Re = 4.56 \times 10^4$ run. The features in figure 3.23(b) are separated by significantly larger distances in the streamwise direction when compared with 3.21(b). For all f_c presented, the features can be visually tracked as they advect downstream with strong signal to noise ratio.

At lower Reynolds number flows, features arising from higher frequency fluctuations are less present in the flow. Images of lower Reynolds number flows filtered at the higher f_c lack strong coherent trackable features, where strength relates to the intensity of the signal compared to the background noise, as illustrated in figure 3.21(d-e).

Figure 3.24 presents dashed line graphics to elucidate chevrons within frames for (a) $Re =$

2.04×10^4 filtered at $f_c/f_{Nyq} = 0.0625$, (b) $Re = 2.46 \times 10^4$ filtered at $f_c/f_{Nyq} = 0.125$, and (c) $Re = 4.56 \times 10^4$ filtered at $f_c/f_{Nyq} = 0.25$. These arrowhead-like structures are seen within certain ranges of Reynolds number and filter center values. The sample images were taken from a range of Reynolds numbers at various filter center values to illustrate the visual similarities between the patterns of these different flows when filtered differently. Recurrent patterns suggest some connection across these scales.

Once this process is completed, each image in the deck is passed through a Canny edge detection algorithm detailed in §3.2 without local non-maxima suppression. For visualization purposes, the value range of the output is remapped to an 8-bit level range and each frequency range is assigned a color.

Figure 3.25 presents a sample image set for $Re = 2.46 \times 10^4$. The image set contains (a) a raw image of a sample frame and the results of it being temporally filtered at f_c/f_{Nyq} =(b) 0.125, (c) 0.25, (d) 0.375, and (e) 0.50, with Canny edge detection subsequently applied. Each filter center was colorized to facilitate the visual inspection of similarities and differences in between the f_c/f_{Nyq} values. Figure 3.25(f) shows the RGB summed result of (b-e), where saturation to a white tone indicates multiple signals summed at that pixel location. A qualitative observation when comparing (b-e) shows the scale of features and the spacing between the features decreasing as f_c/f_{Nyq} is increased. The features in frames (b-e) appear similar, as a cascade of coffee-bean features with scales that decrease with increasing f_c/f_{Nyq}.

Figure 3.26 presents a sample image set for $Re = 4.56 \times 10^4$. Similar trends across f_c/f_{Nyq} are observed as in figure 3.25. When comparing between the two flows for a set f_c/f_{Nyq}, an increase in the size and distance between features is seen with the increase in Reynolds number. Similar trends to figure 3.25 are observed, where the length scale of the coffee-bean features decrease with increasing f_c/f_{Nyq}.

3.4.3 Internal Length Scale Estimation

For this investigation, schlieren image sequences are used, as to visualize the index of refraction variations through the jet, providing an image related to the directional derivative of density of the fluid in the jet. The knife edge was set horizontally, normal to the jet axis, to produce higher contrast for variations in the streamwise direction of the turbulent jet. Once the raw schlieren recording is filtered in time, a range of distinct length scales are observed when viewing results at different temporal frequency filter ranges. The features tend to present as chevrons, waves, or patches advecting with a similar speed. In order to proceed, it is necessary to quantify the scale of these features, in the streamwise direction, as they vary with f_c and Re.

The scales of the jet are investigated within a subregion of the total field of view. This subregion is a section of the image cropped to [512x128], with the larger dimension of the subregion aligned with axis of the jet, starting at 2 diameters downstream of the jet's discharge location.. The region is concatenated with its mirror along the streamwise direction. The mirror image is appended at the downstream edge of the image region, sample illustrations of which can be found in figure 3.27(c) and 3.28(c). The mirroring is done to create a periodic intensity signal in the streamwise direction, circumventing the need to window before taking the discrete Fourier transform. Again, the primary goal for this investigation is to interrogate the streamwise length scales.

Three methods are used to extract the length scale isolated by the PixTif process for different f_c/f_{Nyq} per run. Two of the methods utilize the autocorrelation of the streamwise signal. The interrogation region is long in the streamwise direction and narrower in the cross-stream

direction. The centerline of the 2D autocorrelation in the streamwise direction is examined. Sample autocorrelations can be seen in figure 3.30 for $Re = 10.8 \times 10^4$ and figure 3.32 for $Re = 3.54 \times 10^4$, where f_c/f_{Nyq} =(a) 0.125, (b) 0.25, (c) 0.375, and (d) 0.50 filtered with $f_w/f_{Nyq} = 0.021$. The autocorrelation shown here is an average over all the sampled frames.

The first approach uses osculating parabolas to estimate a $\lambda_{x,osc}$, as found for the streamwise component of Eq. 3.16. The $\lambda_{x,osc}$ provides a scale more commensurate with the streamwise width of the features. The length of $\lambda_{x,osc}$ can be noted as the black bar in figure 3.30 and 3.32 at the end of the black dashed osculating parabola.

The second approach uses the peak-to-trough distance to estimate a length scale referred to as $\lambda_{x,p2t}$, the distances of maximum dissimilarity of the feature measurement. The $\lambda_{x,p2t}$ provides a scale of the spacing between these features. The length of $\lambda_{x,p2t}$ can be noted as the red bar in figure 3.30 and 3.32 in between red dashed vertical lines at the peak and trough of the autocorrelation.

For both approaches using the autocorrelation of the interrogation regions, a subset of all the frames in the image deck is used. This subset is sampled from the full deck in time intervals related to the volumetic flow rate for the run, the capture rate of the recording, and the streamwise length of the interrogation region. An average $\lambda_{x,osc}$ and $\lambda_{x,p2t}$ are recorded along with their respective measured standard deviations.

The third approach uses same the region of the PixTiF'ed frame and calculates its Fourier transform in the streamwise direction. Each row—at a single cross-stream location and time, along the streamwise direction—is investigated as a signal in wave space. This provides a representation of the prominence of wavenumbers in the streamwise direction of the spatial signal. The wavenumber corresponding to the maximum amplitude is found per these interrogated lines. The wavenumbers associated with the maximum amplitude are then averaged over all the cross-stream locations in time and space for each Reynolds number and f_c/f_{Nyq}. The mean values are reported as $k_{x,max}/k_{x,Nyq}$, where $k_{x,Nyq} = \dfrac{2\pi}{2\Delta x}$ is based on the physical spatial resolution of the image, $\Delta x = 95\mu$ m per pixel.

3.4.4 Preliminary Validation: Synthetic Data

To validate the process, the methods are tested on a synthetic data set. A synthetic image deck was constructed with a summation of 6 sine waves at varying frequencies set at the particular filter bands of $f_c/f_{Nyq} = 0.125$, 0.25, 0.375, 0.50, 62.5,and 0.75. A raw image of the interrogation region of the synthetic image can be seen in figure 3.33(a). While their temporal frequencies are different, each sine wave has the same amplitude and wavelength.

Resulting decks from the filtering process with band-passes centered at $f_c/f_{Nyq} = 0.125$, 0.25, 0.375, and 0.50, as seen in figure 3.33(c,e,g,i), captured the independent waves advecting at their respective velocities, allowing for them to be tracked independently. Results from filters with ranges that did not capture the specified frequencies of the sine waves produced images with sporadic speckled noise with no effective signal, as seen in figure 3.33(b,d,f,h).

The length scale estimated by the osculating parabola and peak-to-trough approaches was consistent at each f_c/f_{Nyq}, as expected. The osculating parabola's resulting λ values are in good agreement with the quarter wavelength of the synthetic waves, while the peak-to-trough λ returns the half wavelength. This check provides an orienting framework for reviewing the results when the process is applied on the actual recordings.

3.4.5 Quantitative Measurements

Both figures 3.36 and 3.39 present the results for $\lambda_{x,osc}/D$ and $\lambda_{x,p2t}/D$, respectively, for flow numbers 30-35 in 2.3, where D corresponds to the internal pipe diameter as measured in the recordings, physically 13.8mm and 145pixels in the recordings. Both $\lambda_{x,osc}/D$ and $\lambda_{x,p2t}/D$ monotonically decrease when measured at higher f_c/f_{Nyq}. A result that caused pause, as it was not expected, was that for a fixed f_c/f_{Nyq}, the measured scale of $\lambda_{x,osc}/D$ and $\lambda_{x,p2t}/D$ increases along with increasing Reynolds number.

Although $\lambda_{x,osc}/D$ and $\lambda_{x,p2t}/D$ both increase with increasing Reynolds number and monotonically decrease when measured at higher f_c/f_{Nyq}, they do so at different rates. Figures 3.37 and 3.40 present this same result as a flooded contour plot. The general trends presented in the contour plots provide some insight into the possible dependencies of $\lambda_{x,osc}/D$ and $\lambda_{x,p2t}/D$ on Reynolds number and f_c/f_{Nyq}. Figure 3.38 presents the results for $\lambda_{x,osc}$ normalized by $\left(D \cdot Re^{1/3} \cdot (f_c/f_{Nyq})^{-1/2}\right)$, collapsing the scales onto a bounded line between $[0.9 - 1.1] \times 10^{-2}$, laying close to unity with a factor of 100. Figure 3.41 presents the results for $\lambda_{x,p2t}$ normalized by $\left(D \cdot Re^{1} \cdot (f_c/f_{Nyq})^{-1}\right)$, collapsing the scales well within a bounded line between $[1 - 1.1] \times 10^{-4}$ for all Reynolds numbers and f_c/f_{Nyq}.

For both the osculating and peak-to-trough plots, the scale of the bars represents the standard deviation of the measured mean length scale normalized by their respective factors of their reported values.

Figure 3.42(a-f) presents the prominence as it varies with $k_x/k_{x,Nyq}$ for runs [30-35]. Prominence is defined here as the magnitude of the wavenumbers divided by the maximum magnitude of $f_c/f_{Nyq} = 0.125$ per run. The maximum of $f_c/f_{Nyq} = 0.125$ was used because it was the greatest value with respect the other filter ranges. The prominence provides some insight into the relative intensity amplitudes of the spatial signal in the temporally filtered images, akin to a relative signal to noise ratio for a given run's illumination. The vertical dashed lines indicate the location of $k_{x,max}/k_{x,Nyq}$ for a run at a f_c/f_{Nyq}. Figure 3.43 provides the same information as a flooded contour plot to provide another visualization of the results. A general trend can be observed: lower Reynolds number flows have a wider wavenumber spectrum but have a narrower frequency range when compared to the higher Reynolds number flows. When played in a sequence, the lobe narrows in $k_x/k_{x,Nyq}$ range and widens in f_c/f_{Nyq}.

Figure 3.44 shows $k_{x,max}/k_{x,Nyq}$ as it varies with f_c/f_{Nyq} and Re, presented as a flooded contour. The value $k_{x,max}$ is the wavenumber where the maximum magnitude/prominence is located. Figure 3.44(b) is qualitatively consistent with the trends seen in figure 3.37 and 3.40, considering the inverse relation between wavelength and wavenumber.

When isolated based on their temporal signatures, observations of the homogeneous water jet show that the length scales of internal features increase with Reynolds number. As the Reynolds number increases the temporal signatures of the features, within the jet, can be seen populating higher frequency modes. Ongoing work is anticipated to incorporate the results from the simultaneously captured PIV recordings with the internal scales measured in the schlieren images.

3.4.6 Filter Width Variation

Figures 3.45-3.51 and 3.52-3.58 are comparable to figures 3.35-3.41. They each present results for band-pass filter widths between $f_w/f_{Nyq} = 0.016$ in figures 3.45-3.51, $f_w/f_{Nyq} = 0.021$ in figures 3.35-3.41, and $f_w/f_{Nyq} = 0.031$ in figures 3.52-3.58. The wavelengths in the results appear to be relatively insensitive to f_w/f_{Nyq} when selecting within this range. These sets of figures have been

added here to provide some insight into how varying the filter width parameter alters the results. Within this range, the maximum relative difference in with respect to $f_w/f_{Nyq} = 0.021$ was:

$$\left|\left|\frac{\lambda_{x,osc}(Re, \frac{f_c}{f_{Nyq}}, \frac{f_w}{f_{Nyq}}) - \lambda_{x,osc}(Re, \frac{f_c}{f_{Nyq}}, \frac{f_w}{f_{Nyq}} = 0.021)}{\lambda_{x,osc}(Re, \frac{f_c}{f_{Nyq}}, \frac{f_w}{f_{Nyq}} = 0.021)}\right|\right|_\infty = 0.015 \tag{3.20}$$

for the osculating length scale and :

$$\left|\left|\frac{\lambda_{x,p2t}(Re, \frac{f_c}{f_{Nyq}}, \frac{f_w}{f_{Nyq}}) - \lambda_{x,p2t}(Re, \frac{f_c}{f_{Nyq}}, \frac{f_w}{f_{Nyq}} = 0.021)}{\lambda_{x,p2t}(Re, \frac{f_c}{f_{Nyq}}, \frac{f_w}{f_{Nyq}} = 0.021)}\right|\right|_\infty = 0.033 \tag{3.21}$$

for the peak-to-trough length scale. When selecting the filter width, the main consideration was maximizing the preserved range while minimizing the overlap. Future investigations in this area could evaluate the suitability of a Gaussian band-pass when compared to other filters. A Gaussian band-pass was chosen for this investigation due to its ubiquity and versatility.

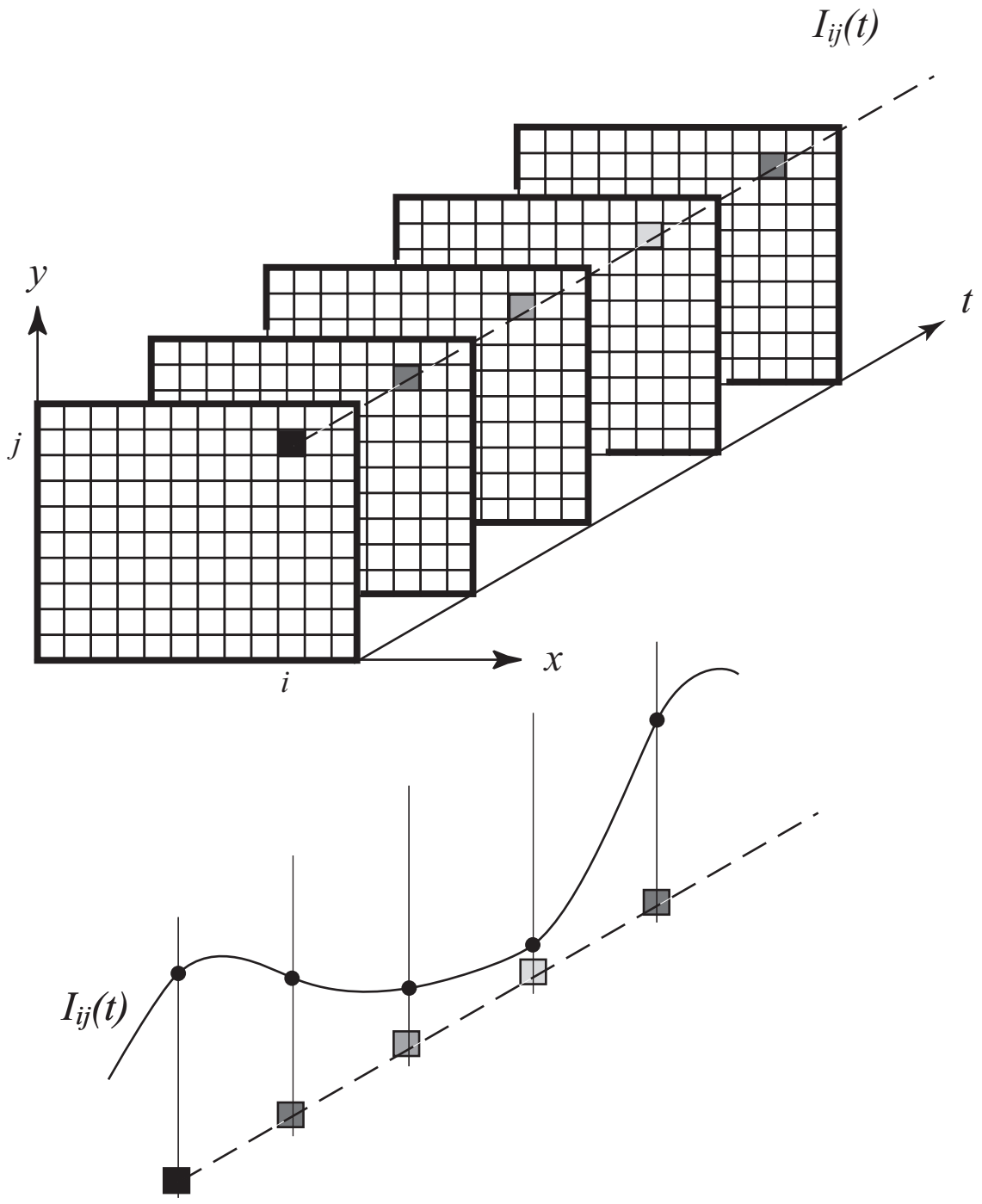

Figure 3.20: A visual representation of the pixelwise temporal signal of a video recording. The temporal filtering process detailed for sub-decks stored in GPU arrays is in essence represented by the pixelwise illustration.

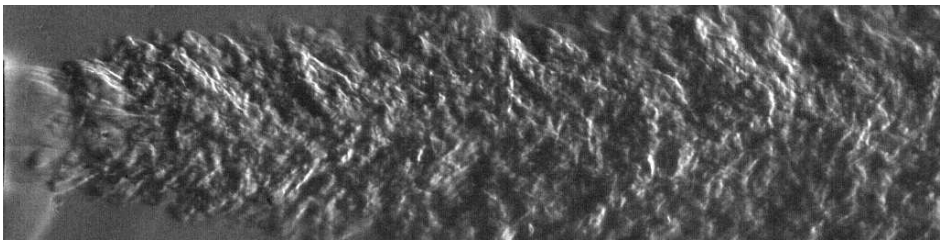

(a)

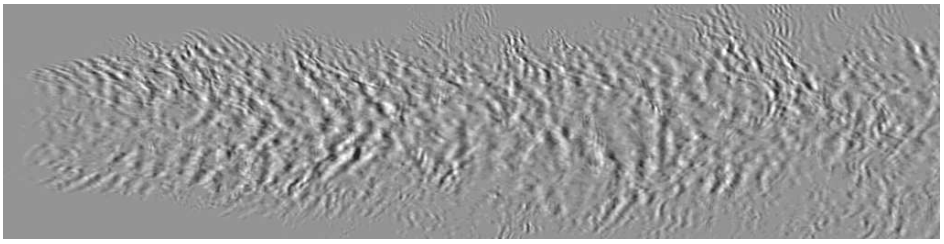

(b)

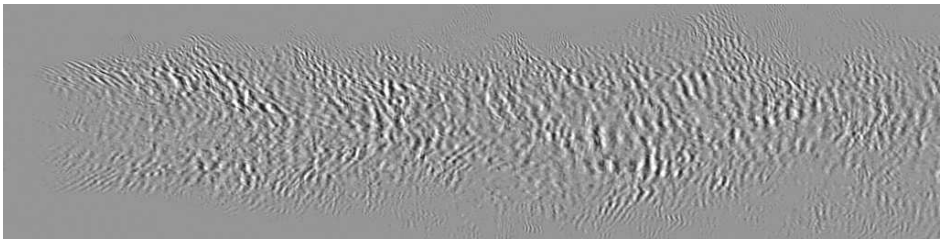

(c)

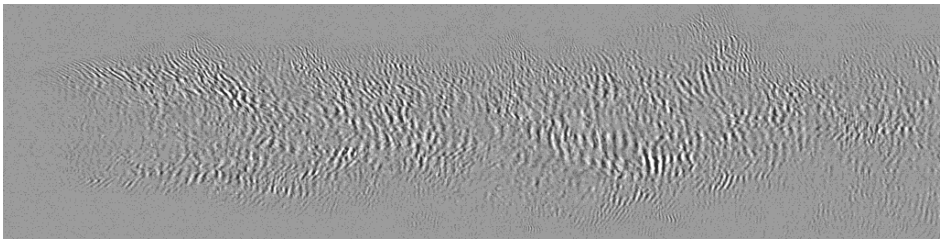

(d)

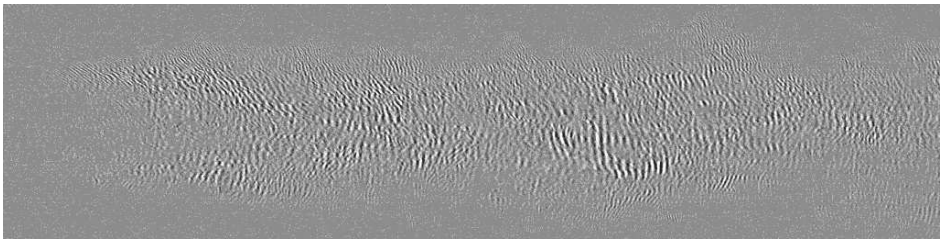

(e)

Figure 3.21: Sample image set for $Re = 0.62 \times 10^4$. The image set contains (a) raw sample frame and the filtered results from f_c/f_{Nyq} =(b) 0.125, (c) 0.25, (d) 0.375, and (e) 0.50. $f_w/f_{Nyq} = 0.021$ for this set.

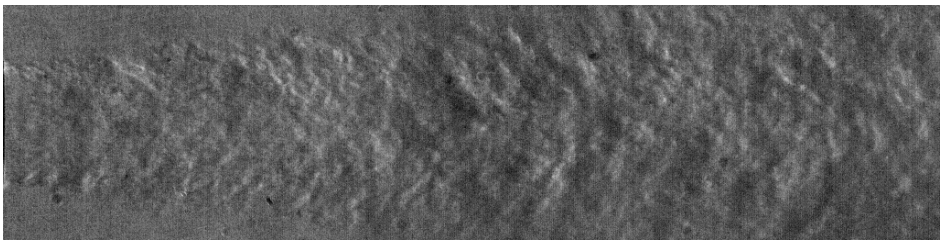

(a)

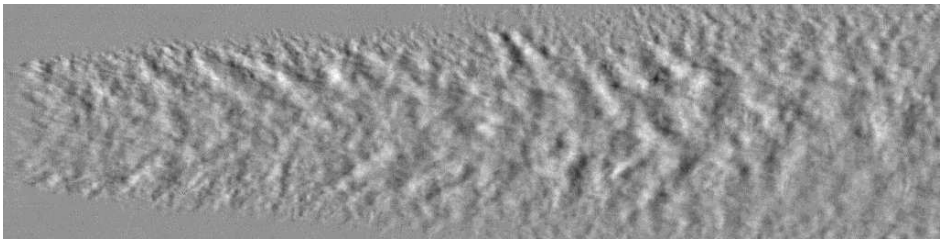

(b)

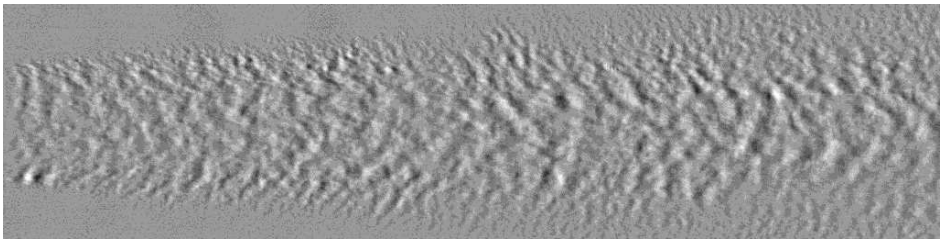

(c)

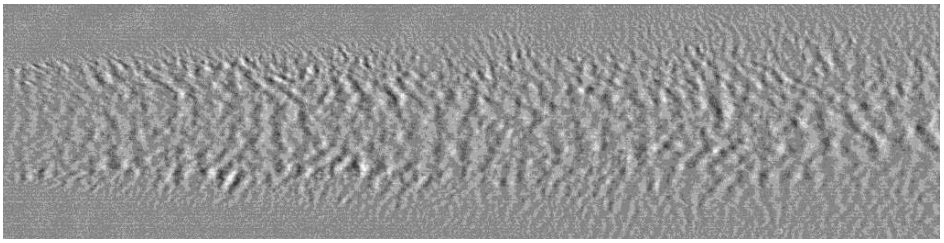

(d)

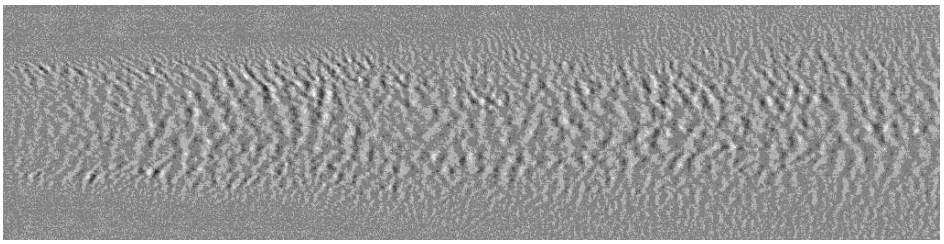

(e)

Figure 3.22: Sample image set for $Re = 2.04 \times 10^4$. The image set contains (a) raw sample frame and the filtered results from f_c/f_{Nyq} =(b) 0.125, (c) 0.25, (d) 0.375, and (e) 0.50. $f_w/f_{Nyq} = 0.021$ for this set.

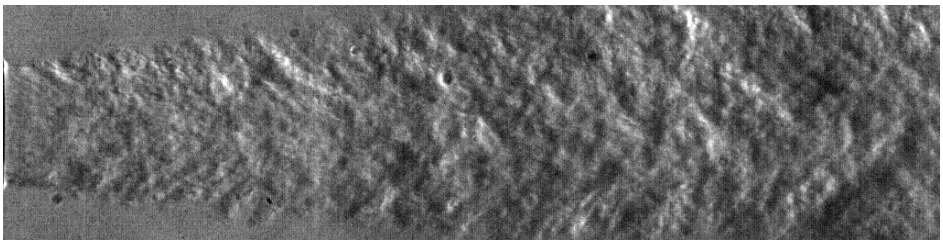

(a)

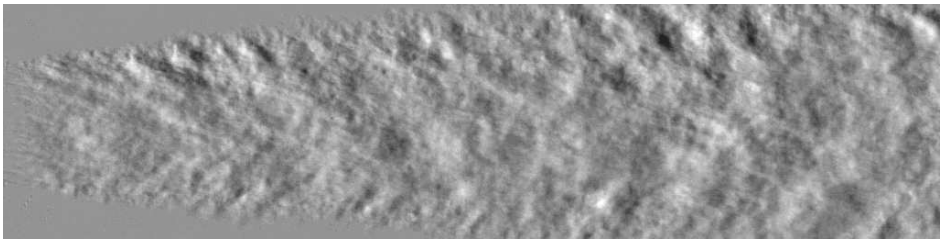

(b)

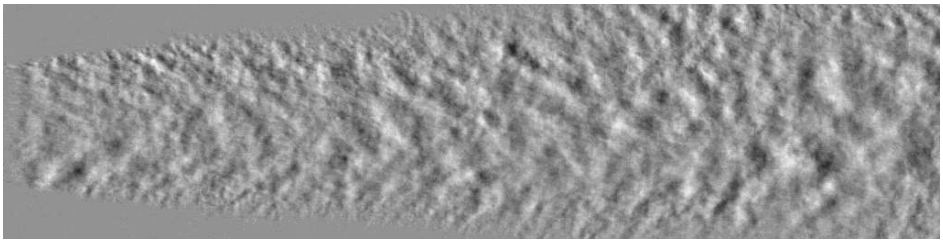

(c)

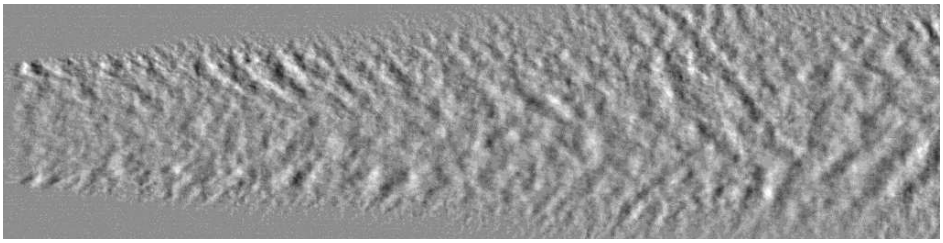

(d)

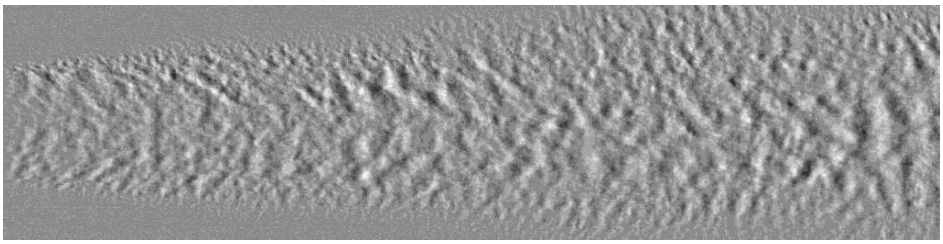

(e)

Figure 3.23: Sample image set for $Re = 4.56 \times 10^4$. The image set contains (a) raw sample frame and the filtered results from f_c/f_{Nyq} =(b) 0.125, (c) 0.25, (d) 0.375, and (e) 0.50. $f_w/f_{Nyq} = 0.021$ for this set.

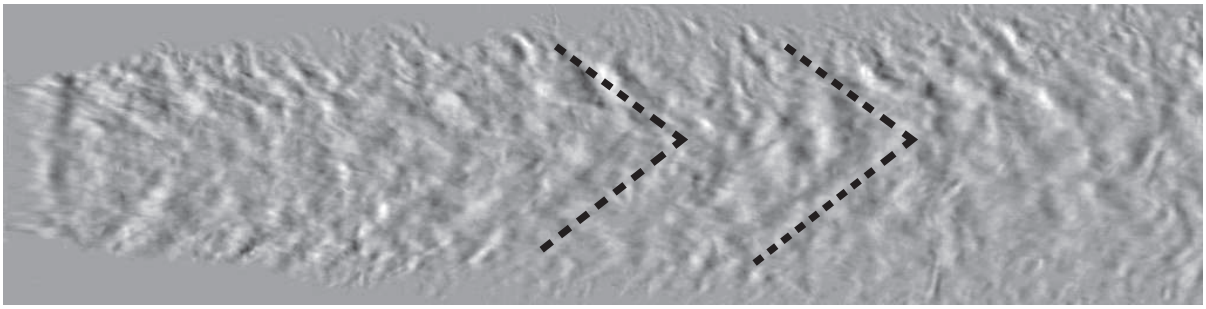

(a) Re = 2.04×10^4

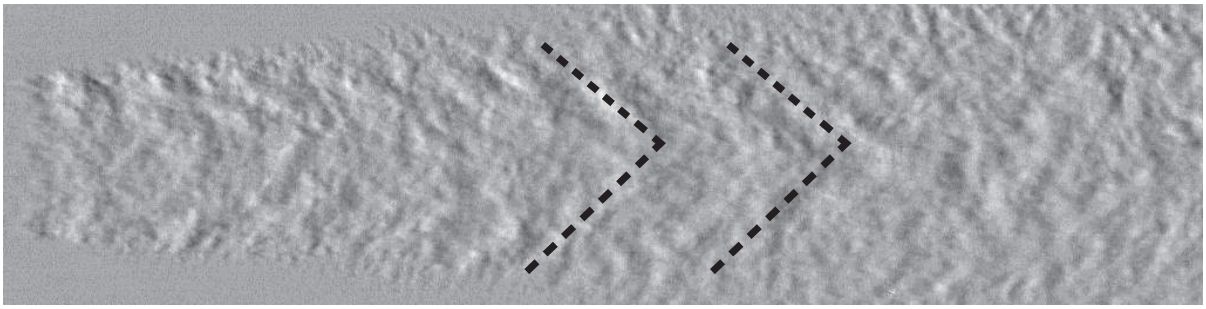

(b) Re = 2.46×10^4

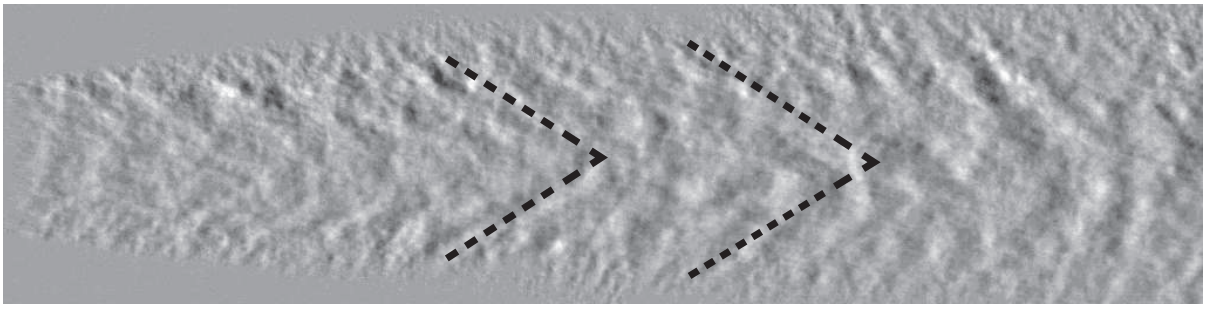

(c) Re = 4.56×10^4

Figure 3.24: The image set contains a frame from (a) run 32 filtered at $f_c/f_{Nyq} = 0.0625$, (b) run 33 filtered at $f_c/f_{Nyq} = 0.125$, and (c) run 35 filtered at $f_c/f_{Nyq} = 0.25$ with chevrons visually placed. $f_w/f_{Nyq} = 0.021$ for this set.

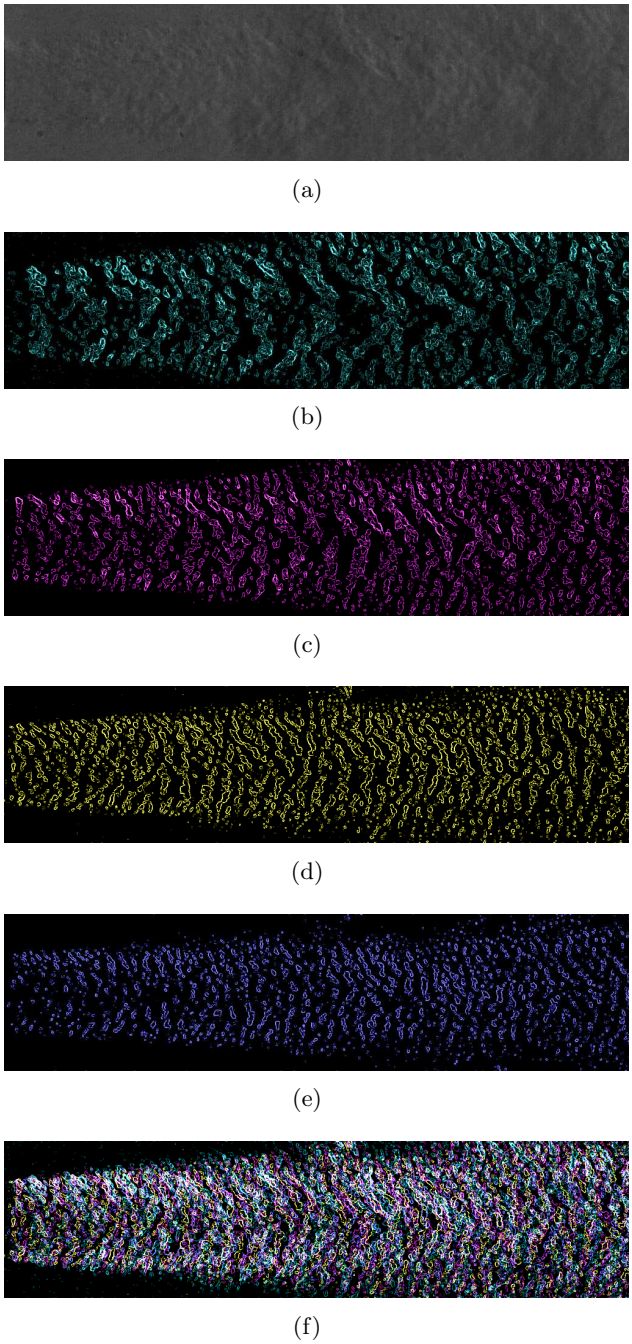

Figure 3.25: Sample image set for $Re = 2.46 \times 10^4$. The image set contains (a) raw sample frame and the temporally filtered results from f_c/f_{Nyq} =(b) 0.125, (c) 0.25, (d) 0.375, and (e) 0.50 after applying a Canny edge detection an colorized for viewing facilitation. (f) is RGB summed result of (b-e), pixel locations, where a white tone indicated multiple signals summed at that pixel location, saturating it to white. $f_w/f_{Nyq} = 0.021$ for this set.

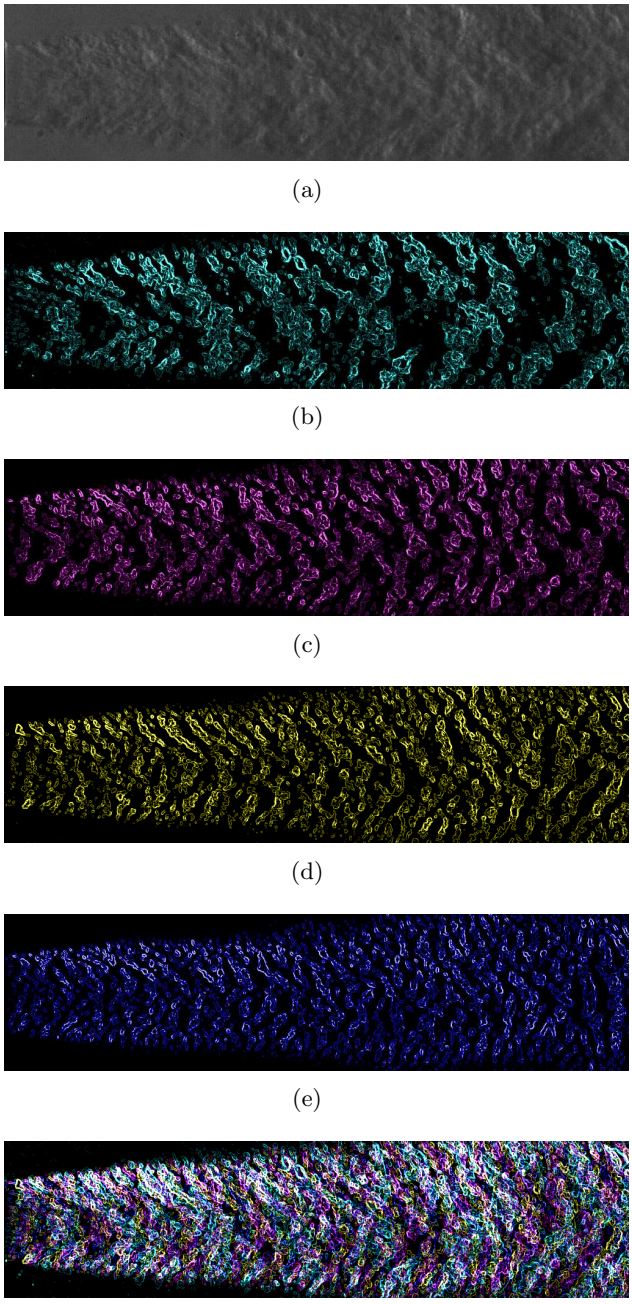

(a)

(b)

(c)

(d)

(e)

(f)

Figure 3.26: Sample image set for $Re = 4.56 \times 10^4$. The image set contains (a) raw sample frame and the temporally filtered results from f_c/f_{Nyq} =(b) 0.125, (c) 0.25, (d) 0.375, and (e) 0.50 after applying a Canny edge detection an colorized for viewing facilitation. (f) is RGB summed result of (b-e), pixel locations, where a white tone indicated multiple signals summed at that pixel location, saturating it to white. $f_w/f_{Nyq} = 0.021$ for this set.

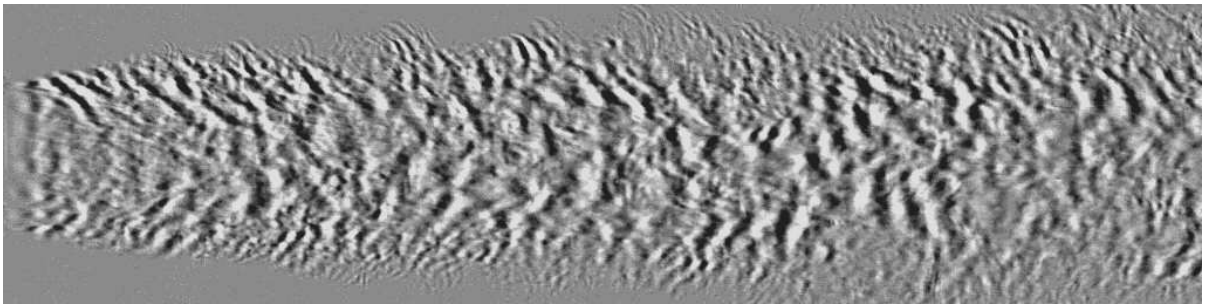

(a)

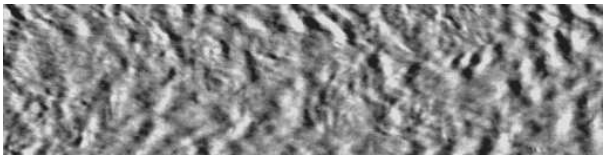

(b)

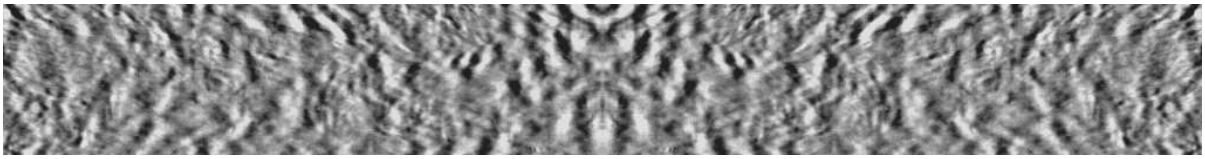

(c)

Figure 3.27: Sample image set for $Re = 1.08 \times 10^4$ at frame 1024. The image set contains the (a) full view of jet profile (b) the interrogation region, and (c) the stitched mirror of the interrogation region to prepare a periodic signal in the stream-wise direction prior to calculation of the autocorrelation. This image is temporally filter using $f_w/f_{Nyq} = 0.125$ and $f_w/f_{Nyq} = 0.021$.

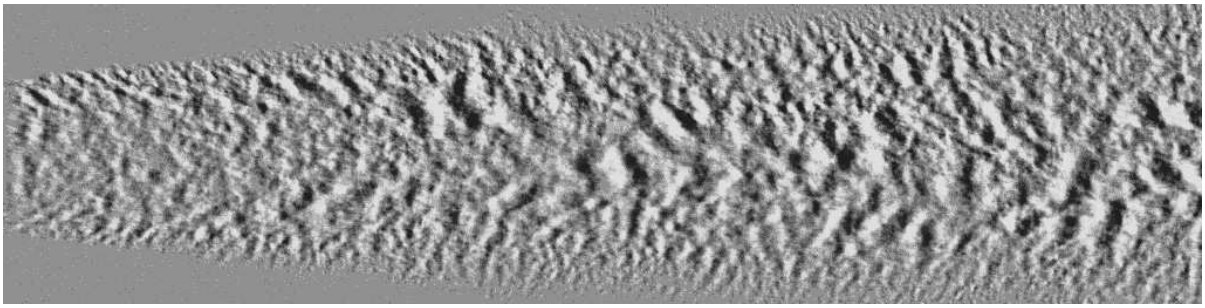

(a)

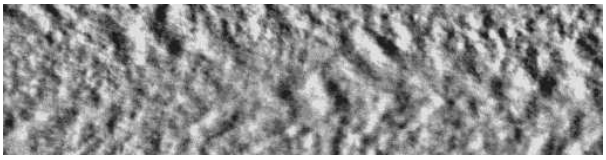

(b)

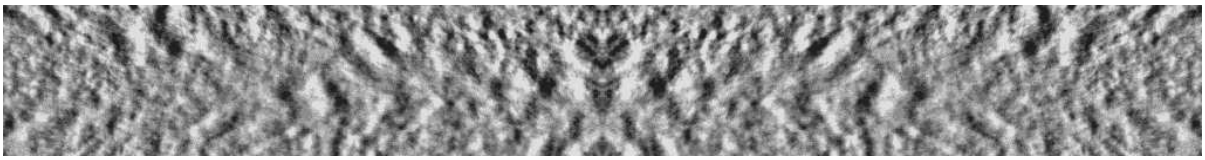

(c)

Figure 3.28: Sample image set for $Re = 3.54 \times 10^4$ at frame 1024. The image set contains the (a) full view of jet profile (b) the interrogation region, and (c) the stitched mirror of the interrogation region to prepare a periodic signal in the stream-wise direction prior to calculation of the autocorrelation. This image is temporally filter using $f_w/f_{Nyq} = 0.375$ and $f_w/f_{Nyq} = 0.021$.

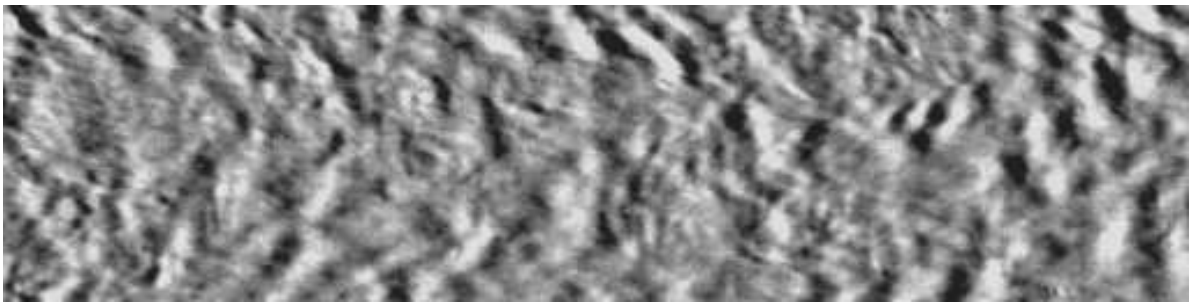

(a)

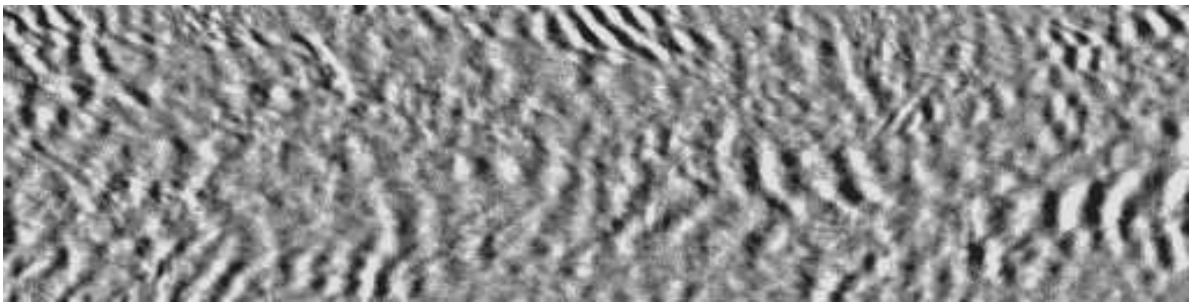

(b)

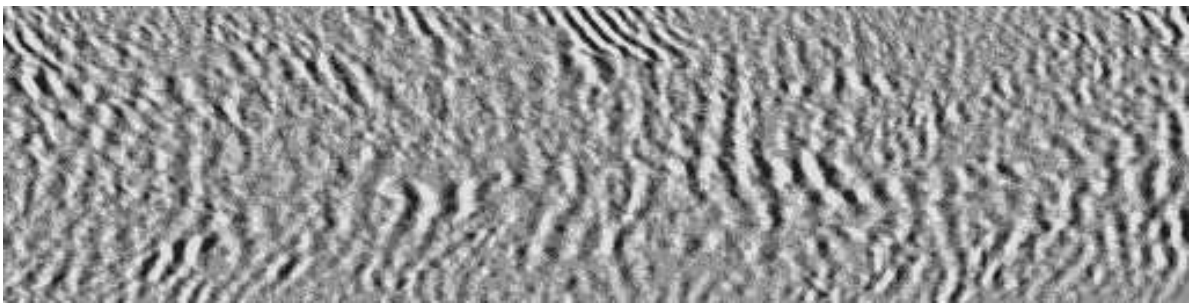

(c)

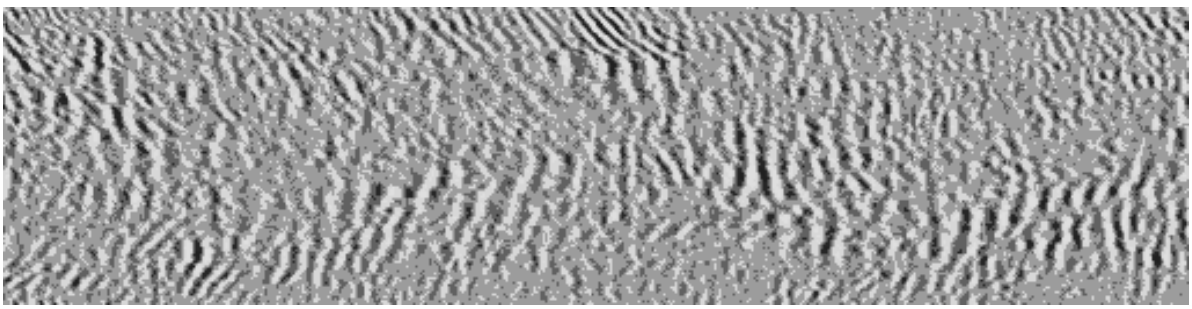

(d)

Figure 3.29: Sample interrogation region $Re = 1.08 \times 10^4$ at frame 1024. Showing f_c/f_{Nyq} =(a) 0.125, (b) 0.25, (c) 0.375, and (d) 0.50 with $f_w/f_{Nyq} = 0.021$.

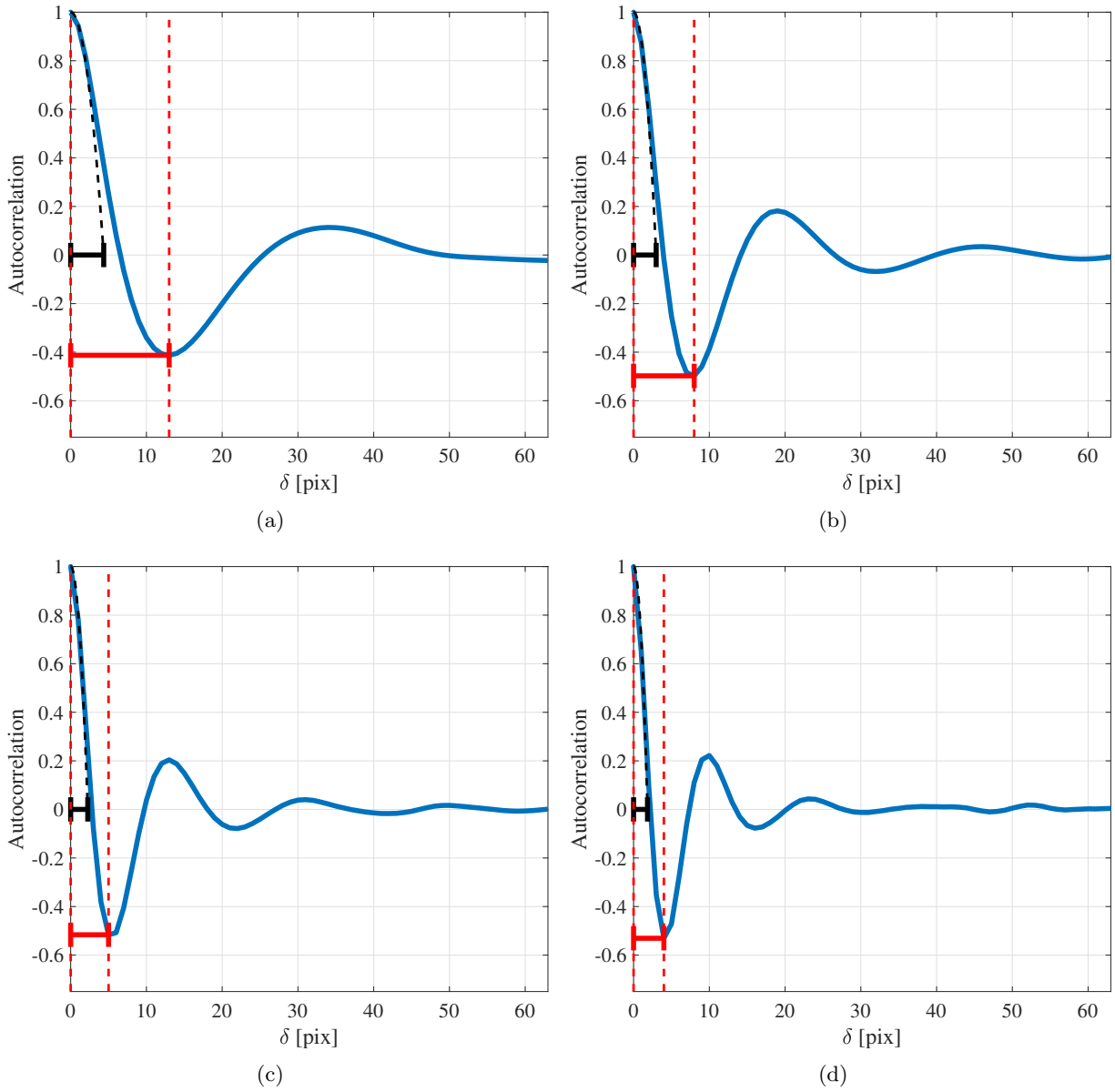

Figure 3.30: Autocorrelation of the mirrored interrogation region $Re = 1.08 \times 10^4$ averaged over all sampled frames. The black bar indicates the measured length scale using the osculating parabola. The red bar indicates the measured peak-to-trough length scale. Showing f_c/f_{Nyq} =(a) 0.125, (b) 0.25, (c) 0.375, and (d) 0.50 with $f_w/f_{Nyq} = 0.021$.

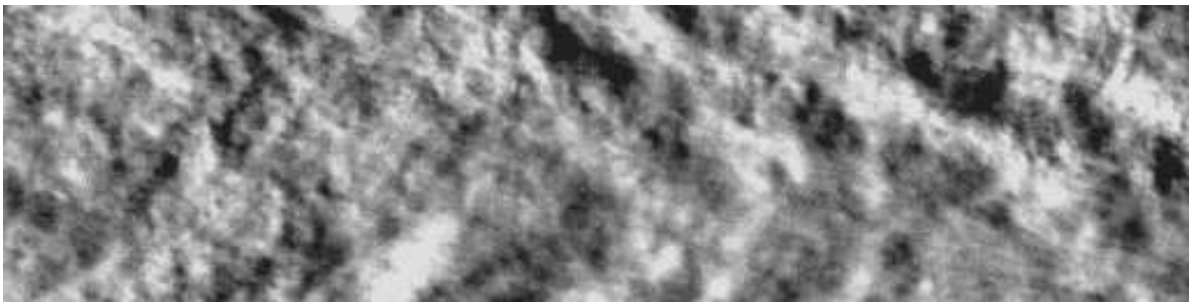

(a)

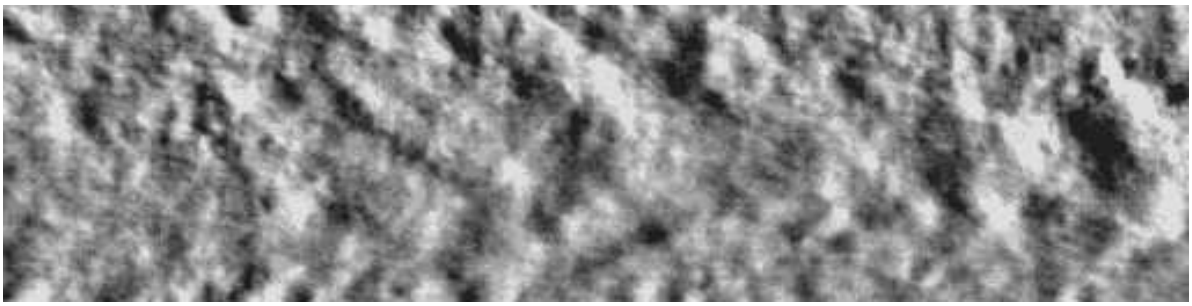

(b)

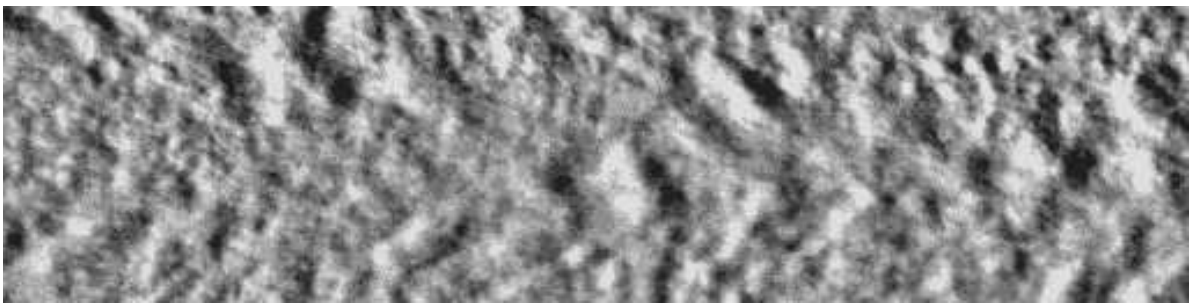

(c)

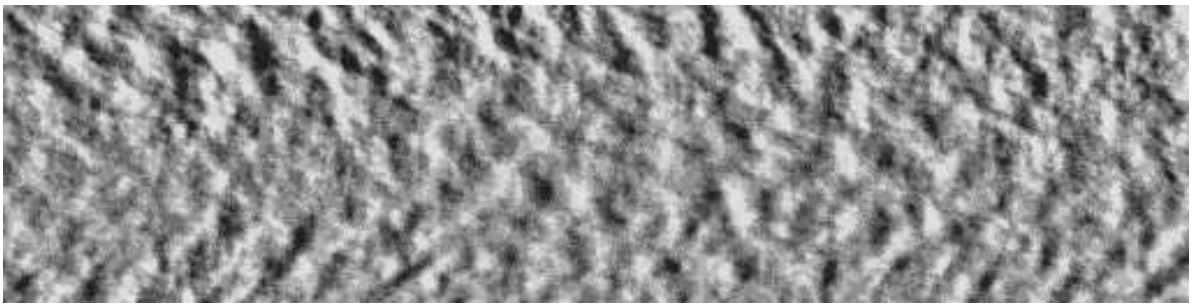

(d)

Figure 3.31: Sample interrogation region $Re = 3.54 \times 10^4$ at frame 1024. Showing f_c/f_{Nyq} =(a) 0.125, (b) 0.25, (c) 0.375, and (d) 0.50 with $f_w/f_{Nyq} = 0.021$.

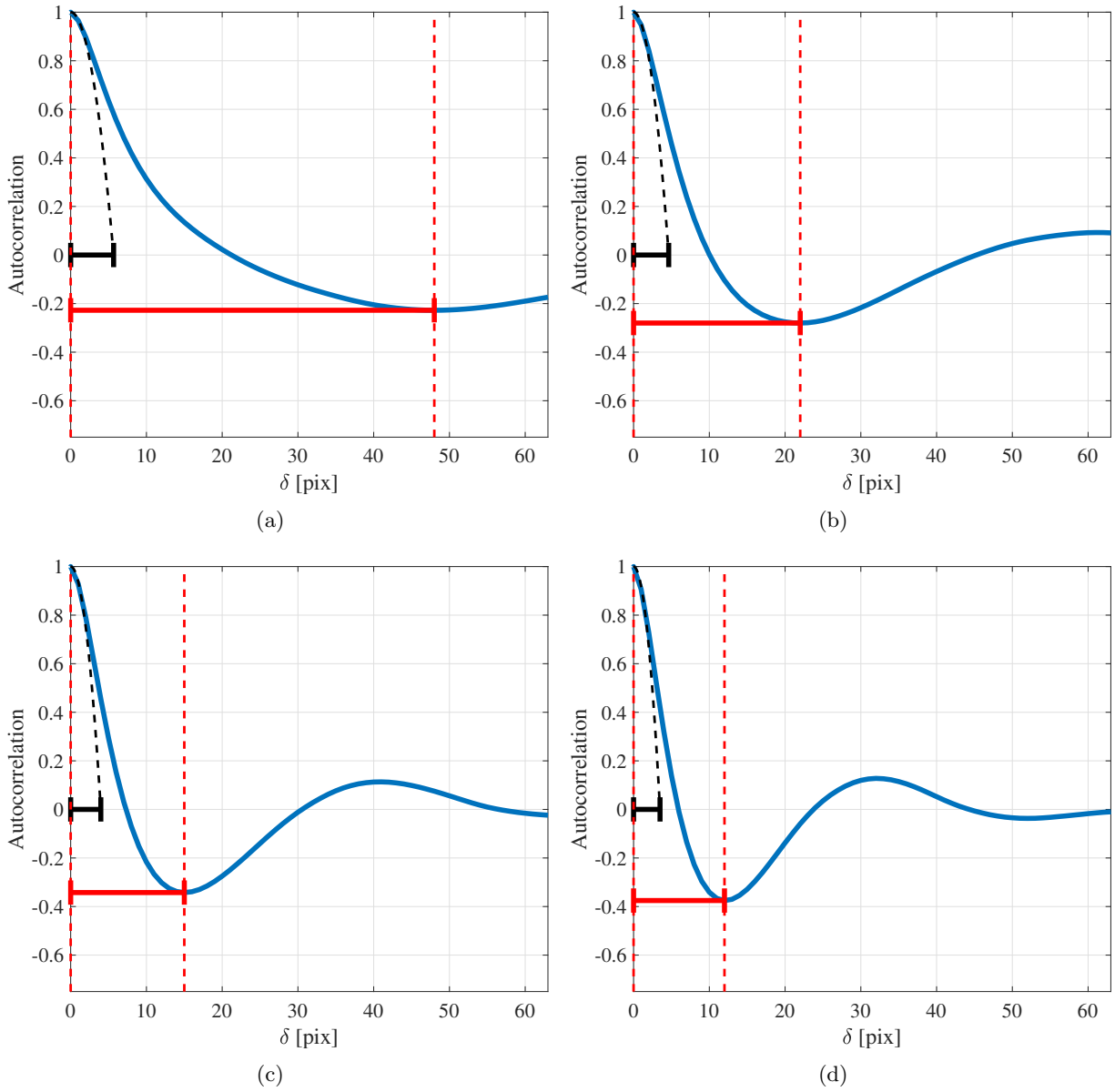

Figure 3.32: Autocorrelation of the mirrored interrogation region $Re = 3.5 \times 10^4$ averaged over all sampled frames. The black bar indicates the measured length scale using the osculating parabola. The red bar indicates the measured peak-to-trough length scale. Showing f_c/f_{Nyq} =(a) 0.125, (b) 0.25, (c) 0.375, and (d) 0.50 with $f_w/f_{Nyq} = 0.021$.

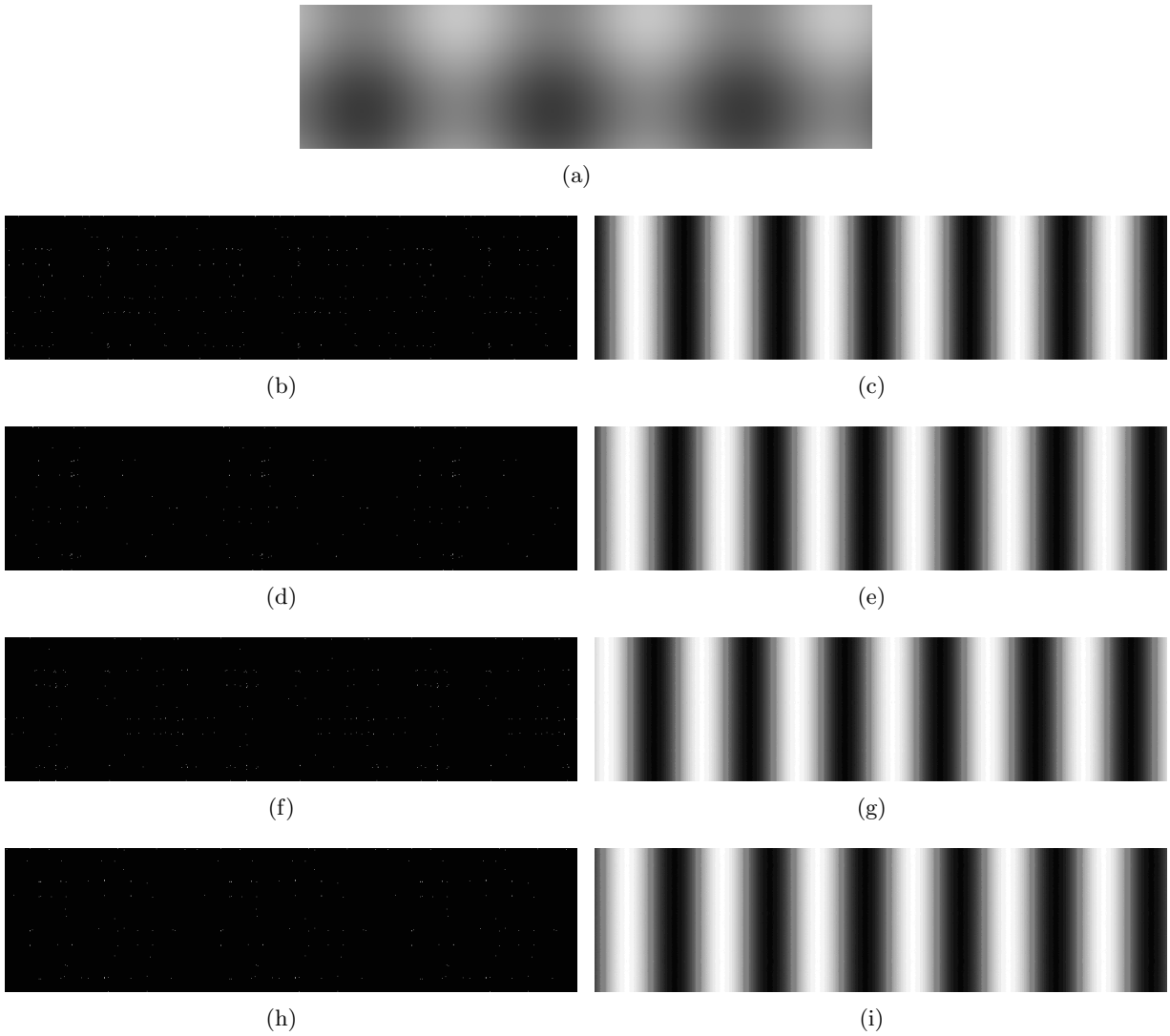

Figure 3.33: Sample interrogation region for the synthetic image deck at frame 1024. Showing (a) raw image, f_c/f_{Nyq} = (b) 0.0625, (c) 0.125, (d) 0.1875, (e) 0.25, (f) 0.3125, (g) 0.375, (h) 0.4375, and (i) 0.50, with $f_w/f_{Nyq} = 0.021$.

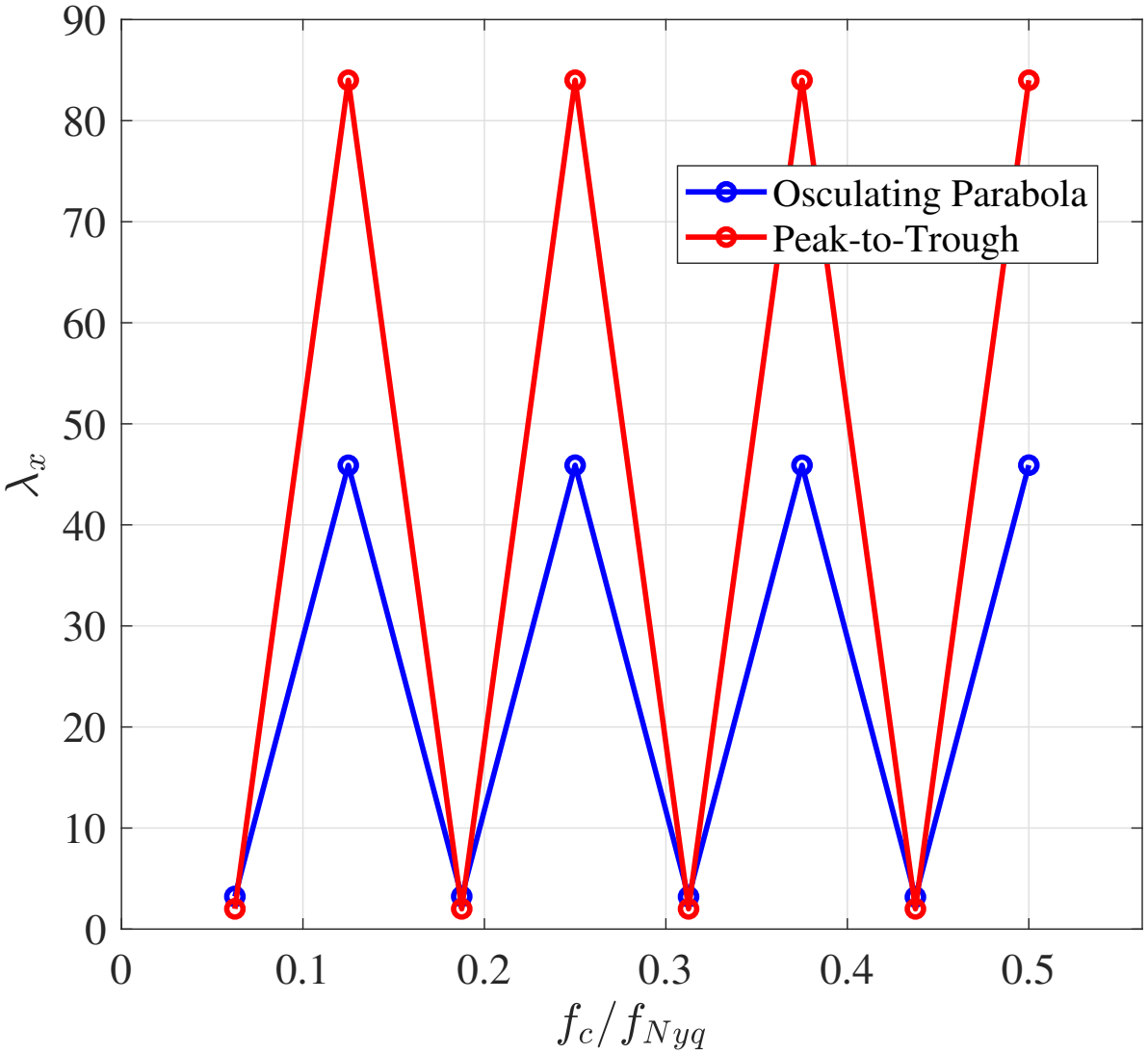

Figure 3.34: Streamwise length scales as measured through autocorrelation using osculating parabolas and peak-to-trough λ plotted against f_c/f_{Nyq} for the synthetic data set. $f_w/f_{Nyq} = 0.021$.

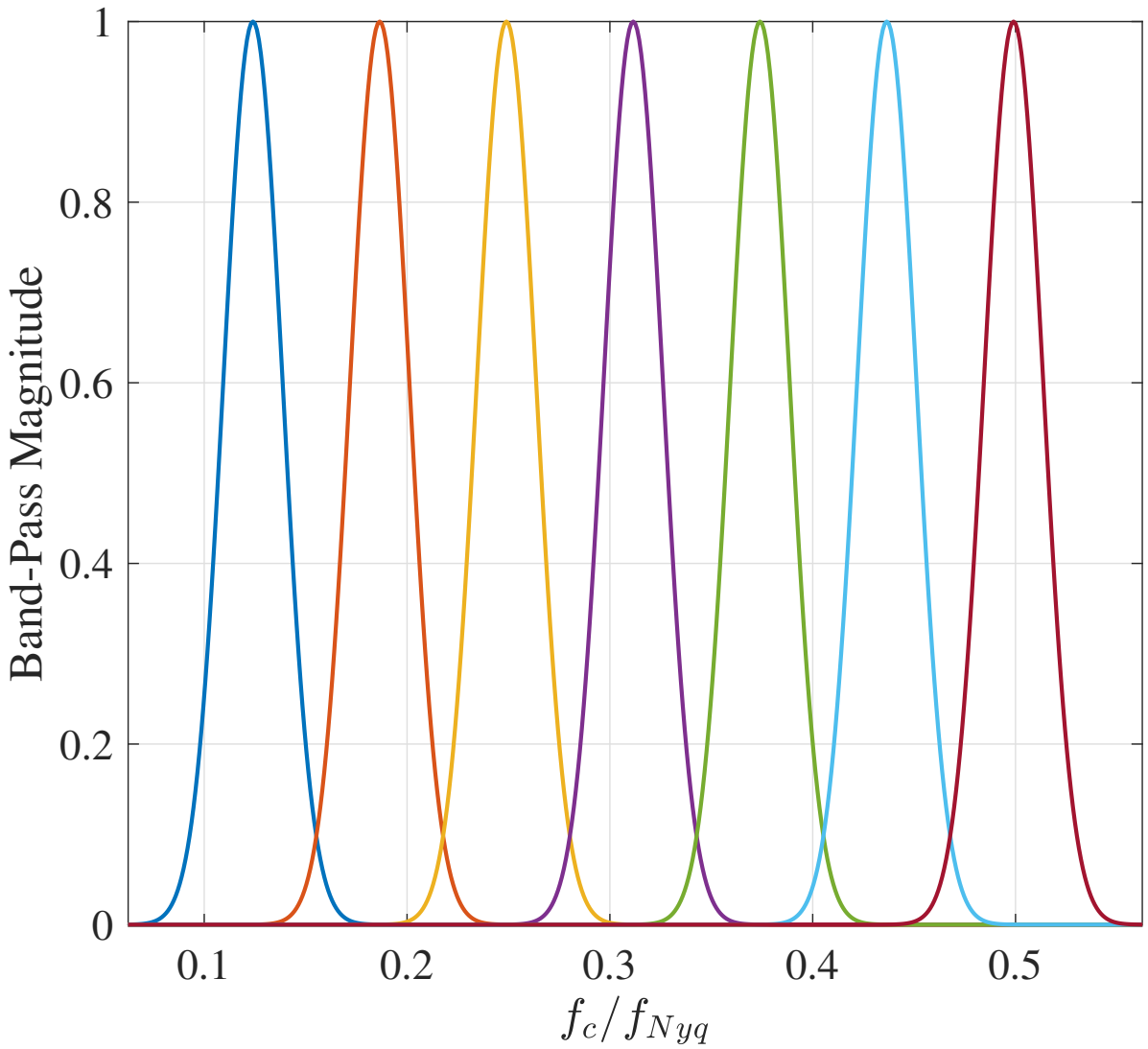

Figure 3.35: Illustration of band-pass filters used in PixTiF process - demonstration the centers and the widths normalized by the Nyquist Frequency associated with the image capture rate, $f_w/f_{Nyq} = 0.021$.

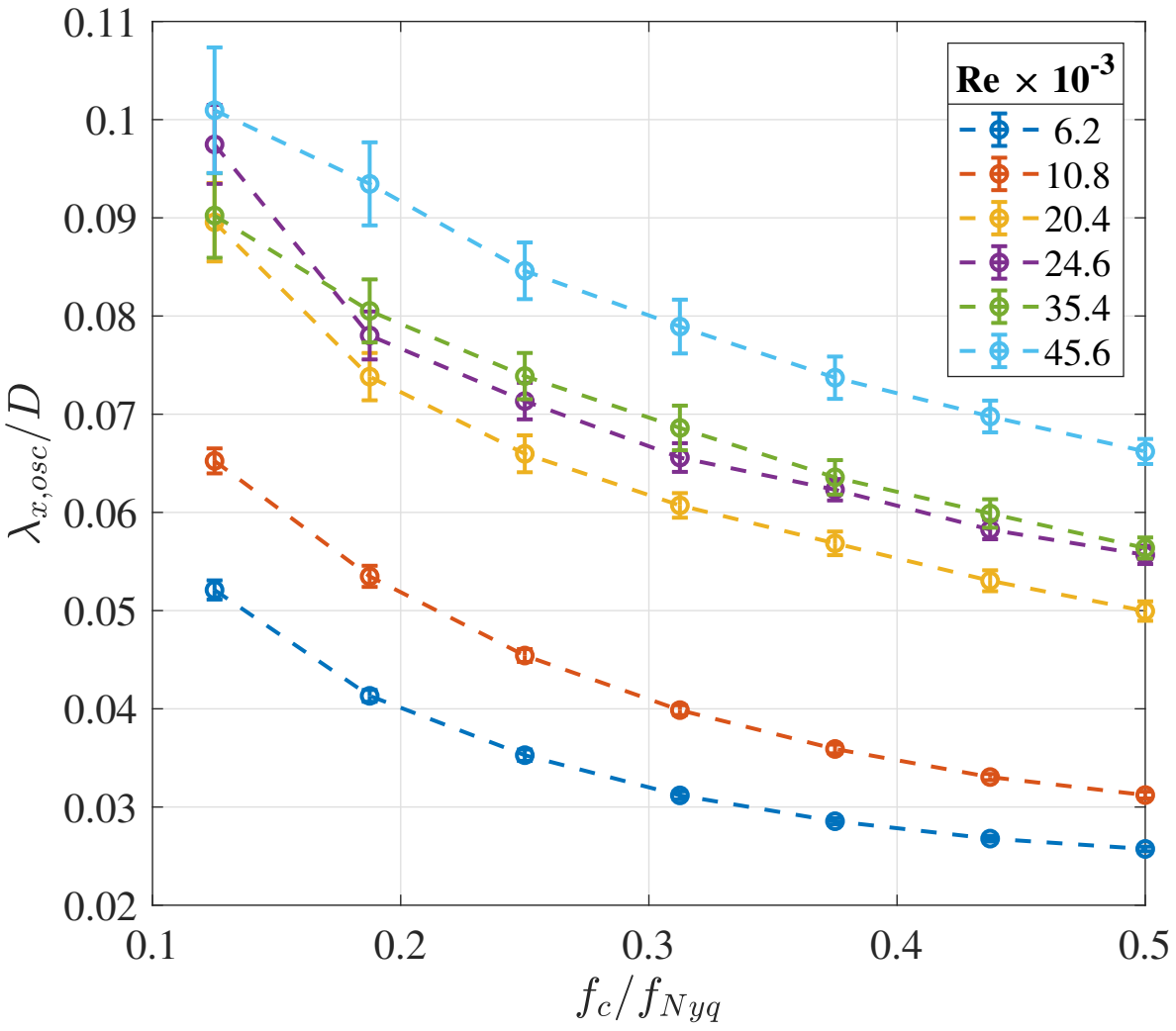

Figure 3.36: Streamwise length scales as measured through auto correlation osculating parabola of $\lambda_{x,osc}/D$ plotted against f_c/f_{Nyq} for different Reynolds Numbers. $f_w/f_{Nyq} = 0.021$ for this set.

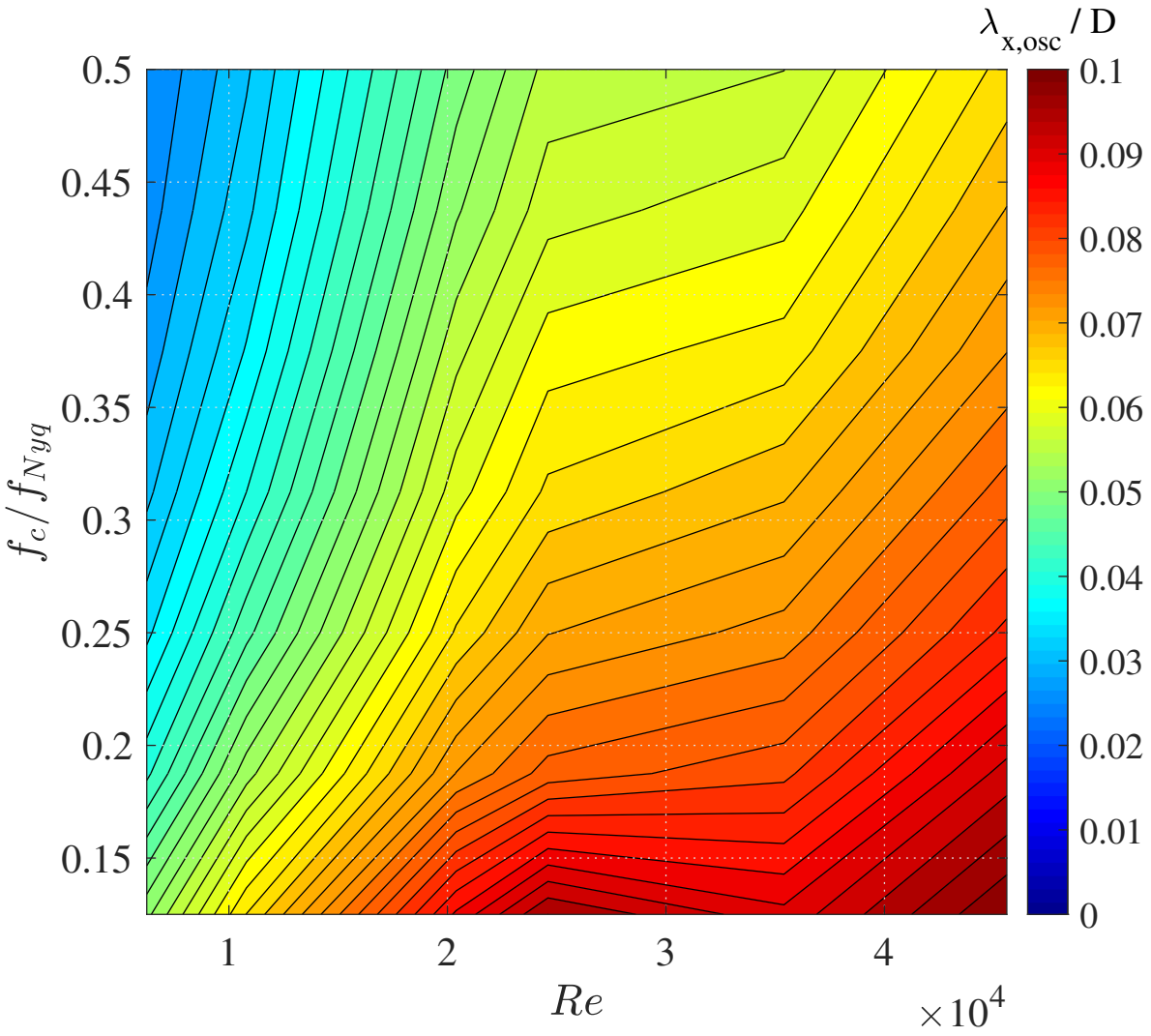

Figure 3.37: Flooded contour plot illustrating streamwise length scales as measured through auto correlation osculating parabola of $\lambda_{x,osc}/D$ as a function of f_c/f_{Nyq} and Reynolds Numbers, Re. $f_w/f_{Nyq} = 0.021$ for this set.

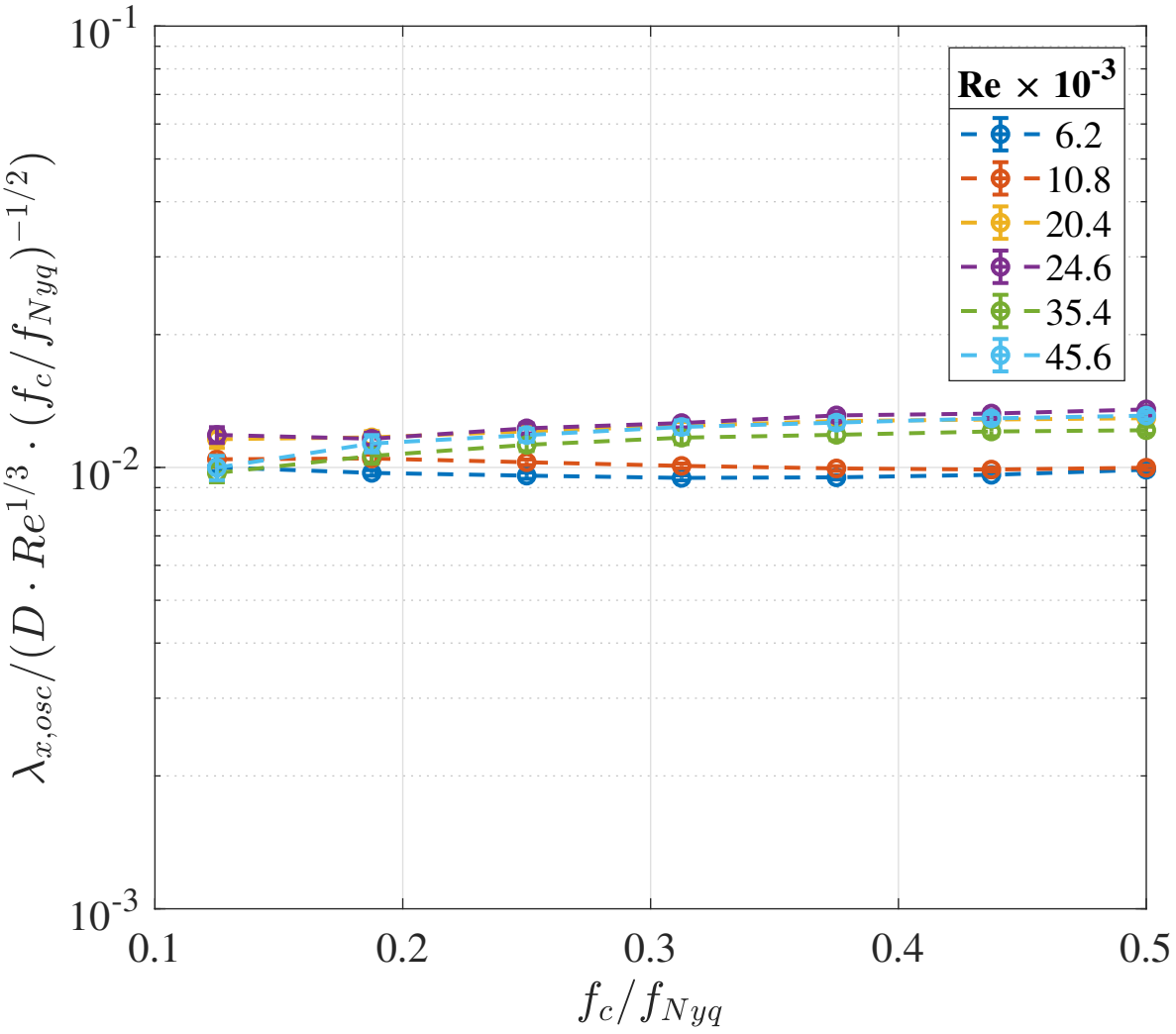

Figure 3.38: Normalized streamwise length scales as measured through auto correlation osculating parabola of $\lambda_{x,osc}/\left(D{\cdot}Re^{1/3}{\cdot}(f_c/f_{Nyq})^{-1/2}\right)$ plotted against f_c/f_{Nyq} for different Reynolds Numbers. $f_w/f_{Nyq} = 0.021$ for this set.

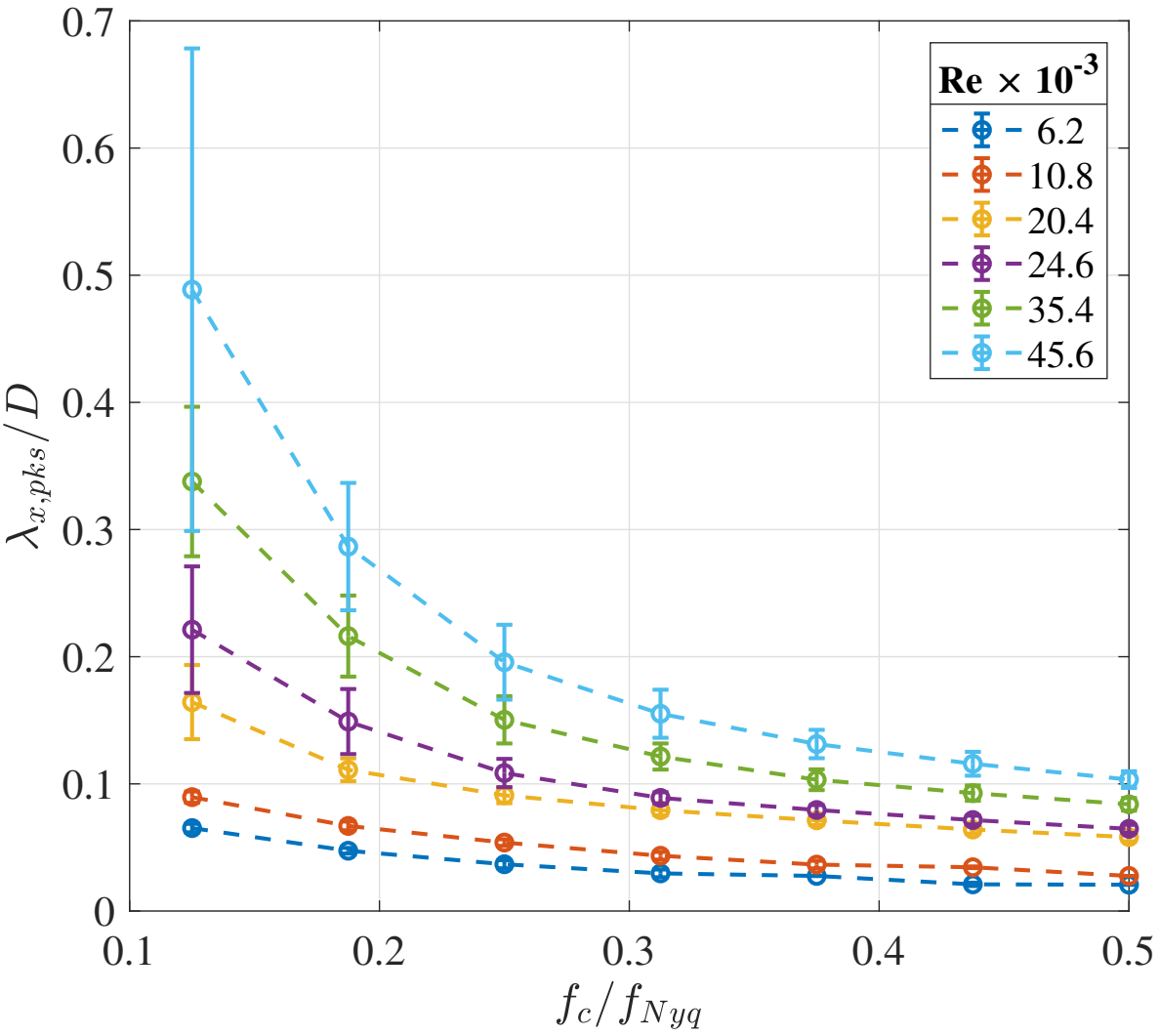

Figure 3.39: Streamwise length scales as measured through auto correlation peak-to-trough of $\lambda_{x,pks}/D$ plotted against f_c/f_{Nyq} for different Reynolds Numbers. $f_w/f_{Nyq} = 0.021$ for this set.

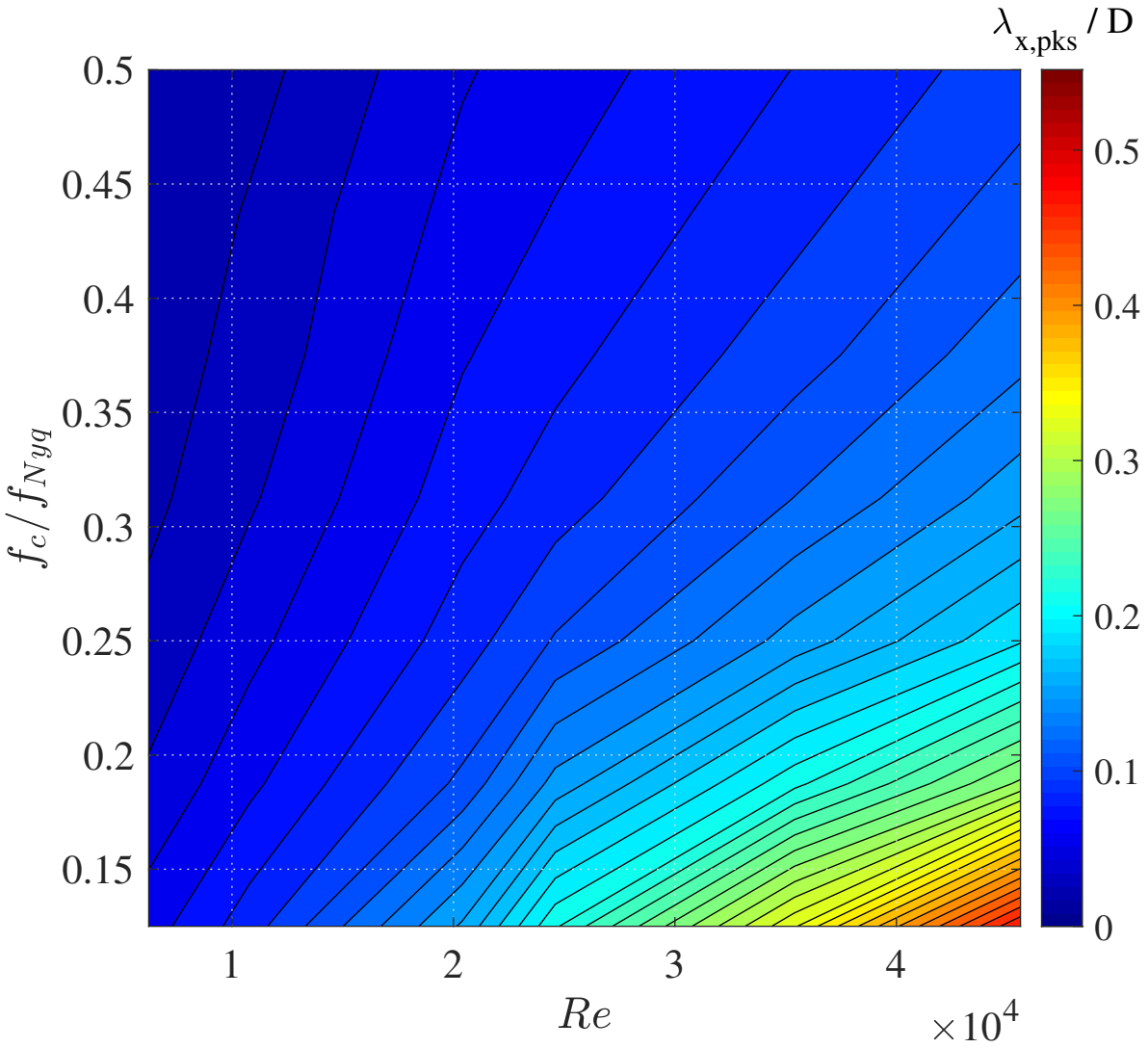

Figure 3.40: Flooded contour plot illustrating streamwise length scales as measured through auto correlation peak-to-trough of $\lambda_{x,pks}/D$ as a function of f_c/f_{Nyq} and Reynolds Numbers, Re. $f_w/f_{Nyq} = 0.021$ for this set.

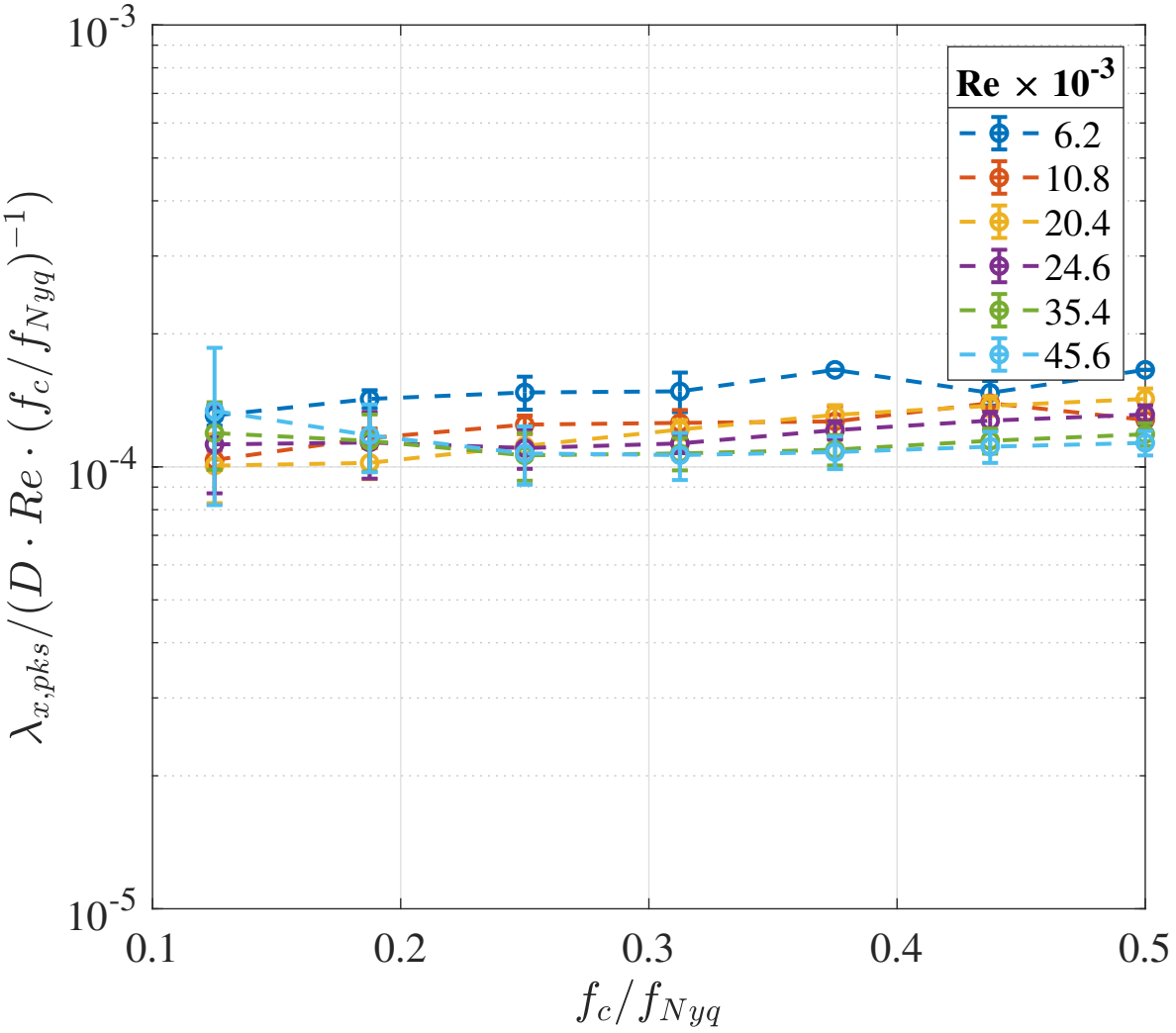

Figure 3.41: Normalized streamwise length scales as measured through auto correlation peak-to-trough of $\lambda_{x,pks}/\left(D \cdot Re \cdot (f_c/f_{Nyq})^{-1}\right)$ plotted against f_c/f_{Nyq} for different Reynolds Numbers. $f_w/f_{Nyq} = 0.021$ for this set.

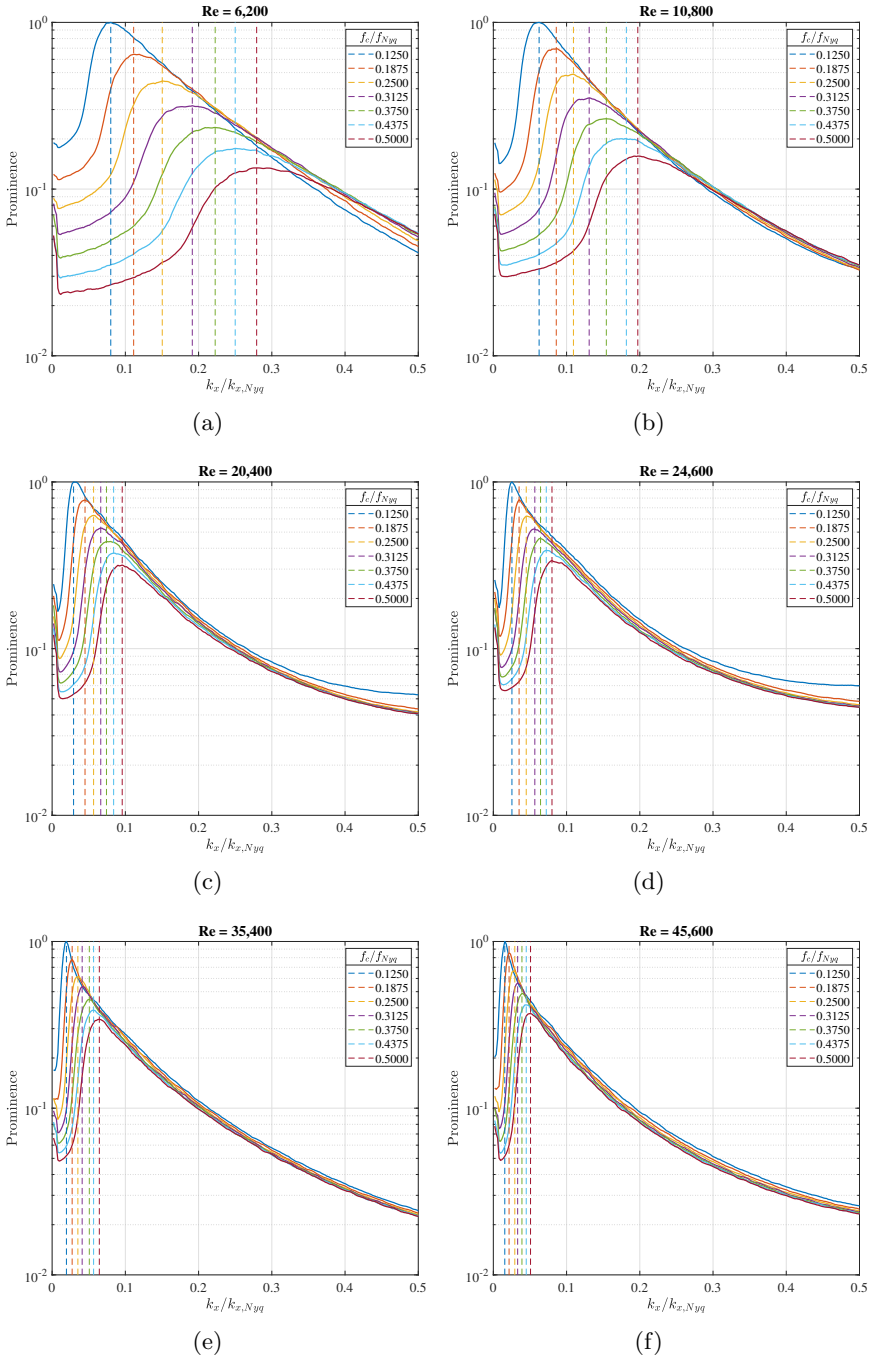

Figure 3.42: Results for streamwise wavenumber prominence as it varies $k_x/k_{x,Nyq}$ and f_c/f_{Nyq} and for $Re =$ (a) 0.62×10^4, (b) 1.08×10^4, (c) 2.04×10^4, (d) 2.46×10^4, (e) 3.54×10^4, and (f) 4.56×10^4 as a solid line plot. Prominence is defined as magnitude of the wavenumber bin divided by the maximum bin magnitude of $f_c/f_{Nyq} = 0.125$ per run. Vertical dashed line indicate the location of $k_{x,max}/k_{x,Nyq}$ colored by respective f_c/f_{Nyq}. $f_w/f_{Nyq} = 0.021$ for this set.

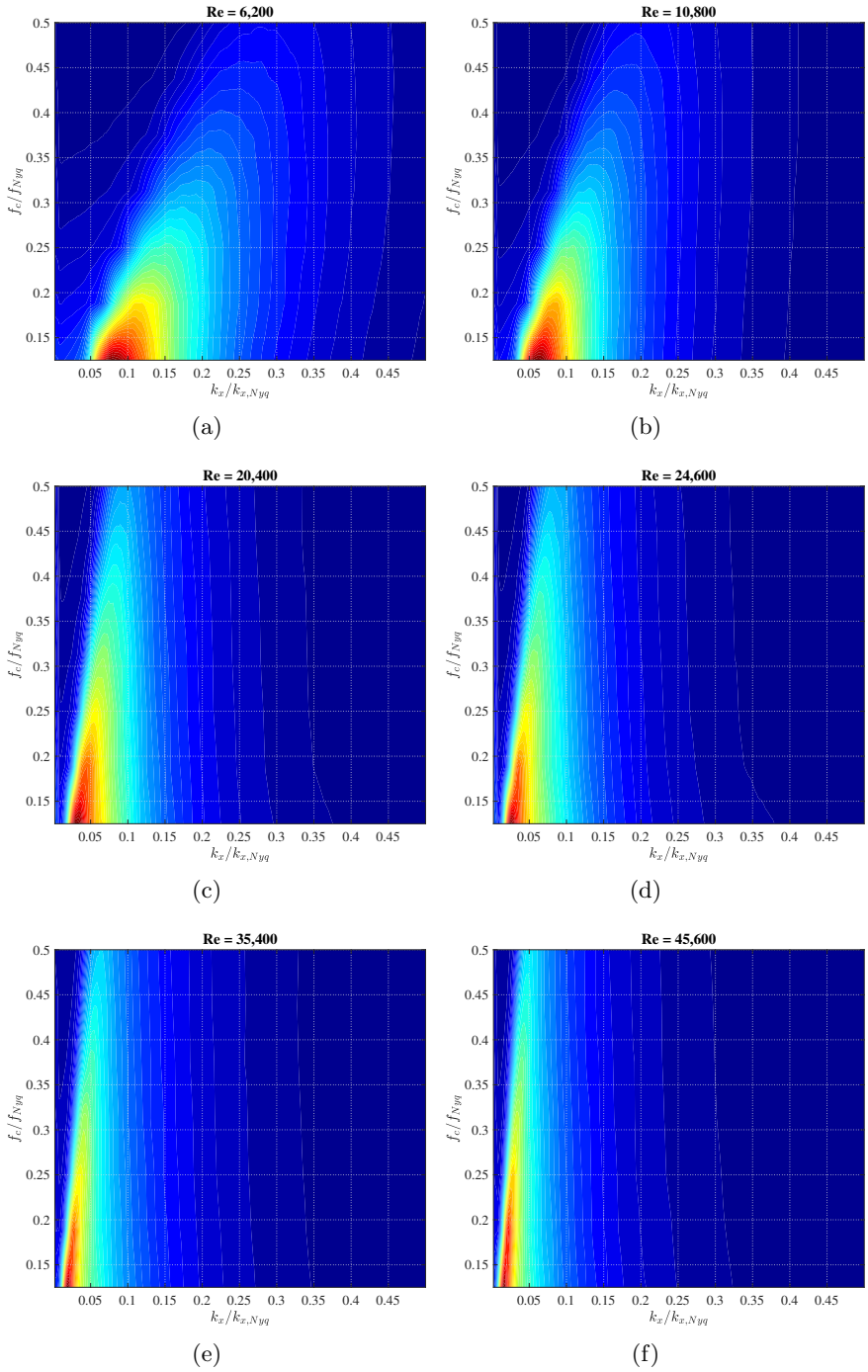

Figure 3.43: Results for streamwise wavenumber prominence as it varies $k_x/k_{x,Nyq}$ and f_c/f_{Nyq} and for $Re =$ (a) 0.62×10^4, (b) 1.08×10^4, (c) 2.04×10^4, (d) 2.46×10^4, (e) 3.54×10^4, and (f) 4.56×10^4 as a flooded contour plot. The color map is scale is equal the Prominence. $f_w/f_{Nyq} = 0.021$ for this set.

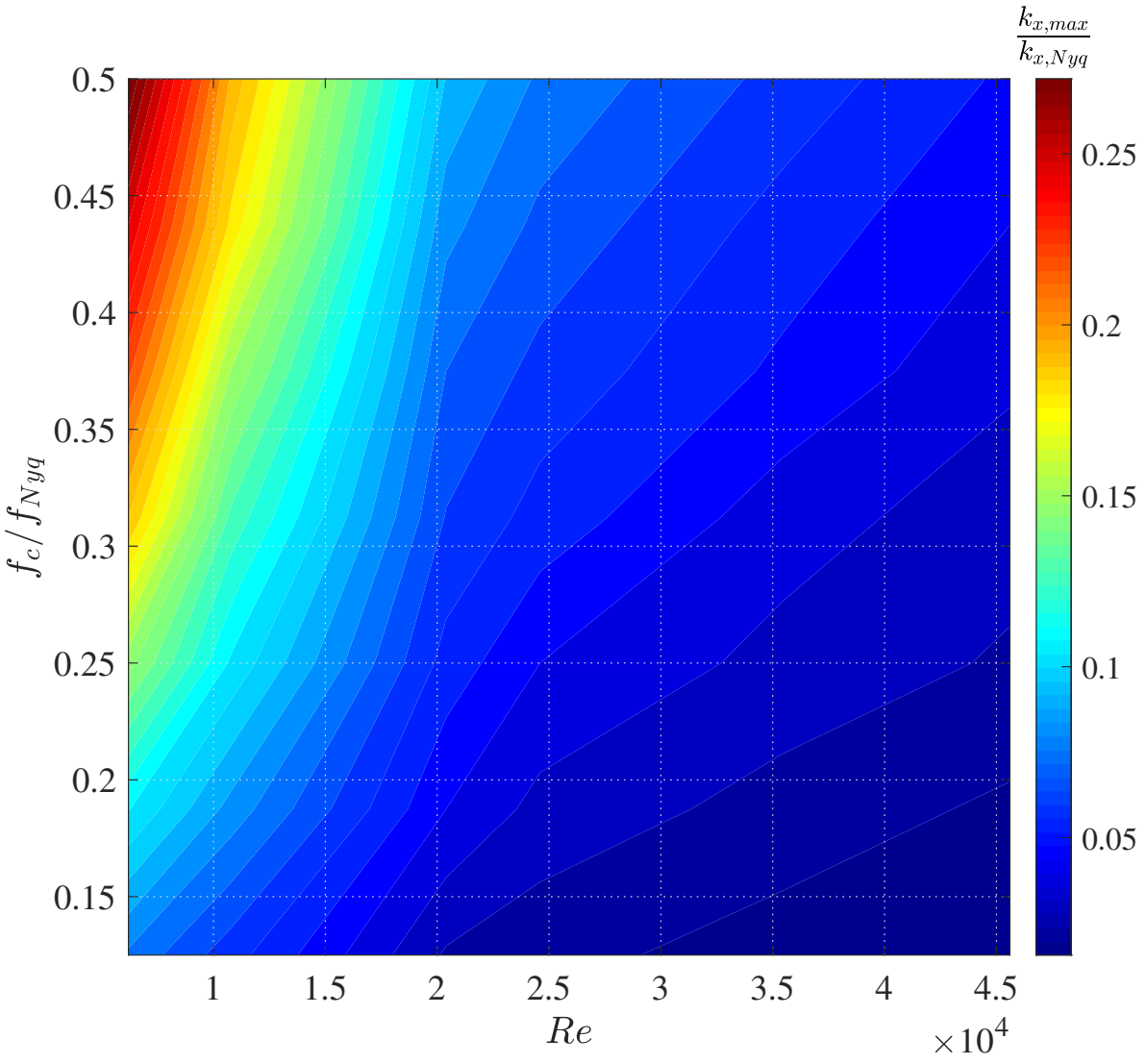

Figure 3.44: $k_{x,max}/k_{x,Nyq}$ as it varies with f_c/f_{Nyq} and Reynolds number, presented as a flooded contour plot. The value $k_{x,max}$ is the wavenumber where the maximum magnitude/prominence is located with respect to Reynolds number and of f_c/f_{Nyq}. $f_w/f_{Nyq} = 0.021$ for this set.

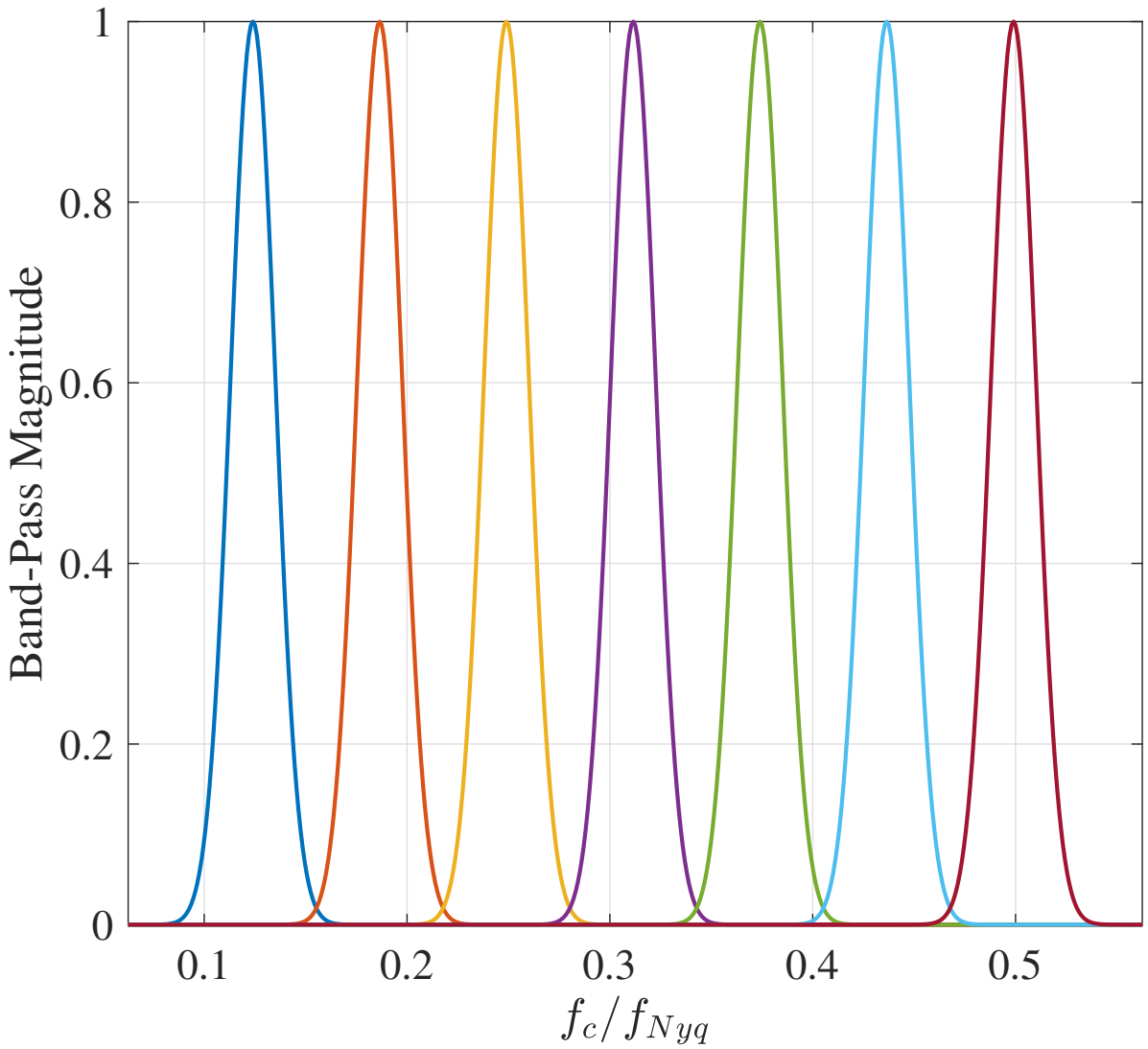

Figure 3.45: Illustration of band-pass filters used in PixTiF process - demonstration the centers and the widths normalized by the Nyquist Frequency associated with the image capture rate, $f_w/f_{Nyq} = 0.016$.

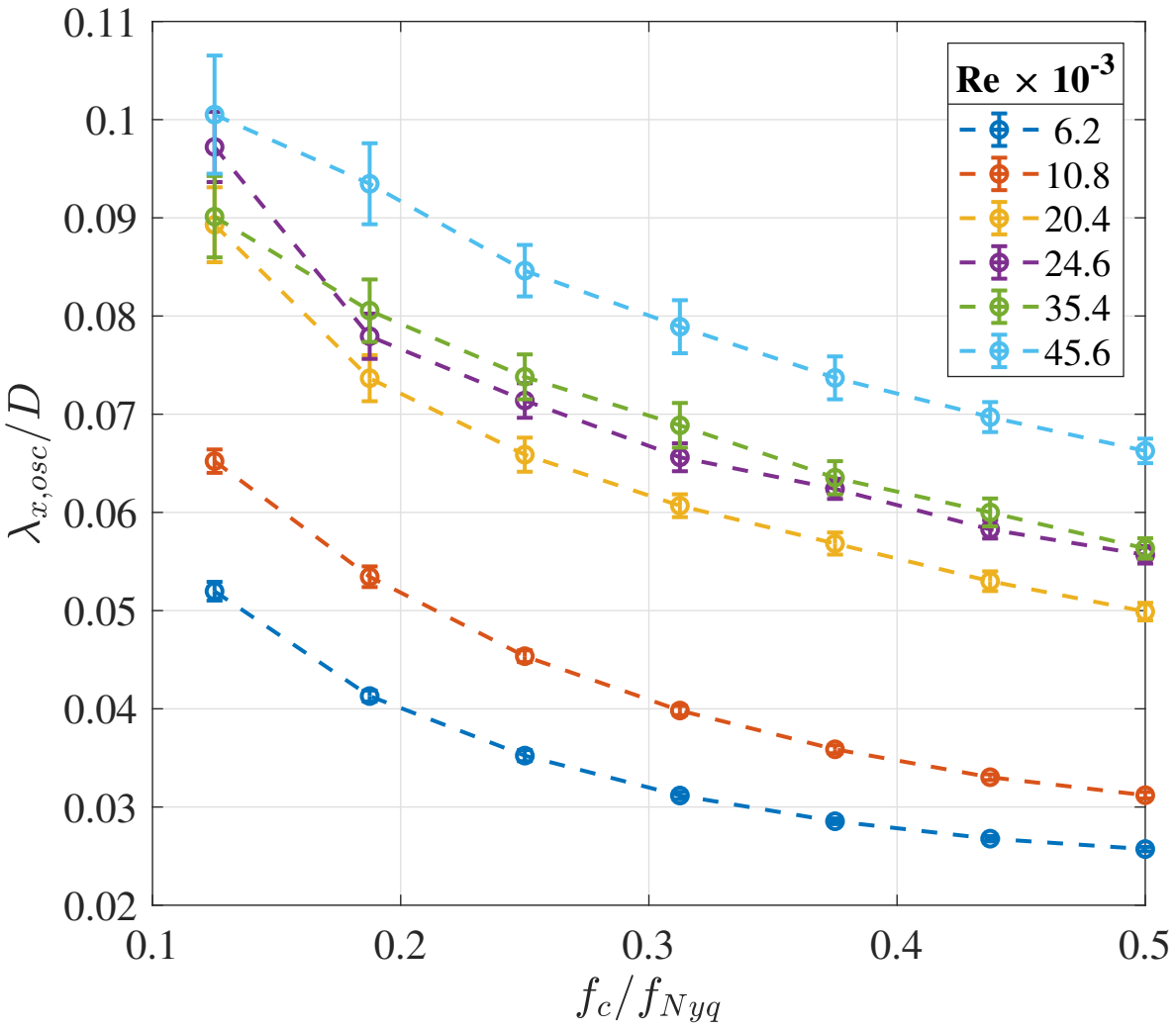

Figure 3.46: Streamwise length scales as measured through auto correlation osculating parabola of $\lambda_{x,osc}/D$ plotted against f_c/f_{Nyq} for different Reynolds Numbers. $f_w/f_{Nyq} = 0.016$ for this set.

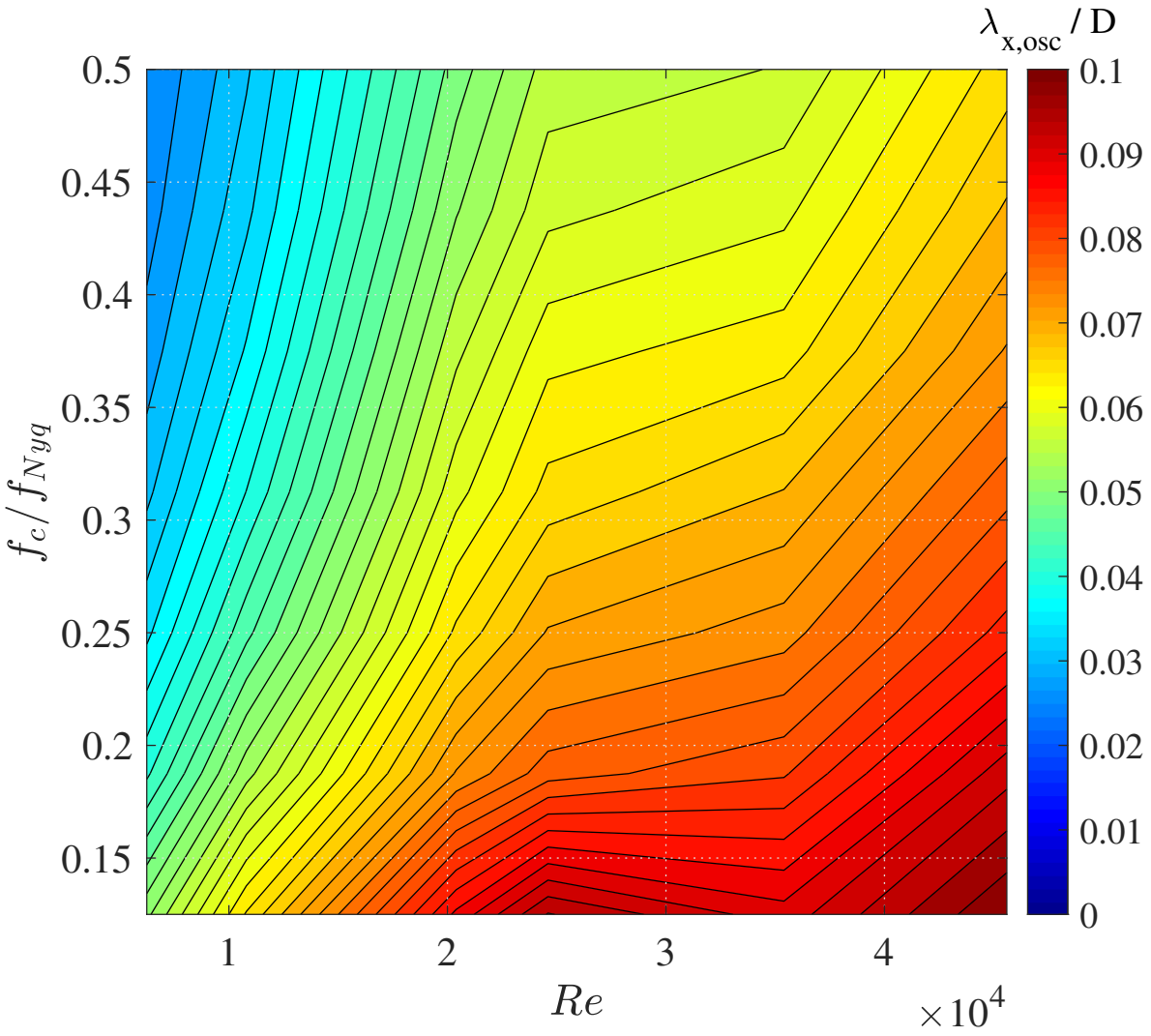

Figure 3.47: Flooded contour plot illustrating streamwise length scales as measured through auto correlation osculating parabola of $\lambda_{x,osc}/D$ as a function of f_c/f_{Nyq} and Reynolds Numbers, Re. $f_w/f_{Nyq} = 0.016$ for this set.

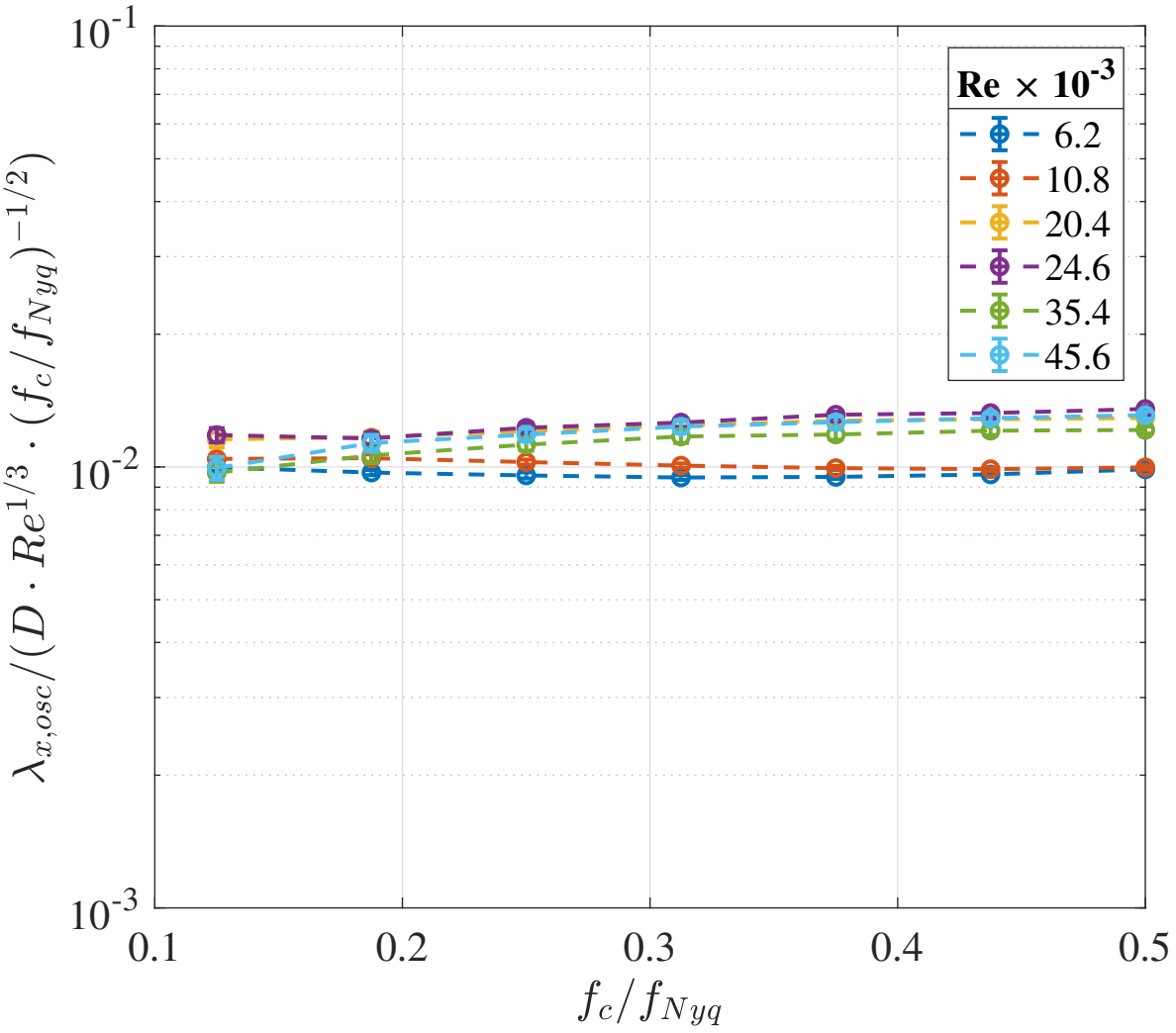

Figure 3.48: Normalized streamwise length scales as measured through auto correlation osculating parabola of $\lambda_{x,osc}/\left(D{\cdot}Re^{1/3}{\cdot}(f_c/f_{Nyq})^{-1/2}\right)$ plotted against f_c/f_{Nyq} for different Reynolds Numbers. $f_w/f_{Nyq} = 0.016$ for this set.

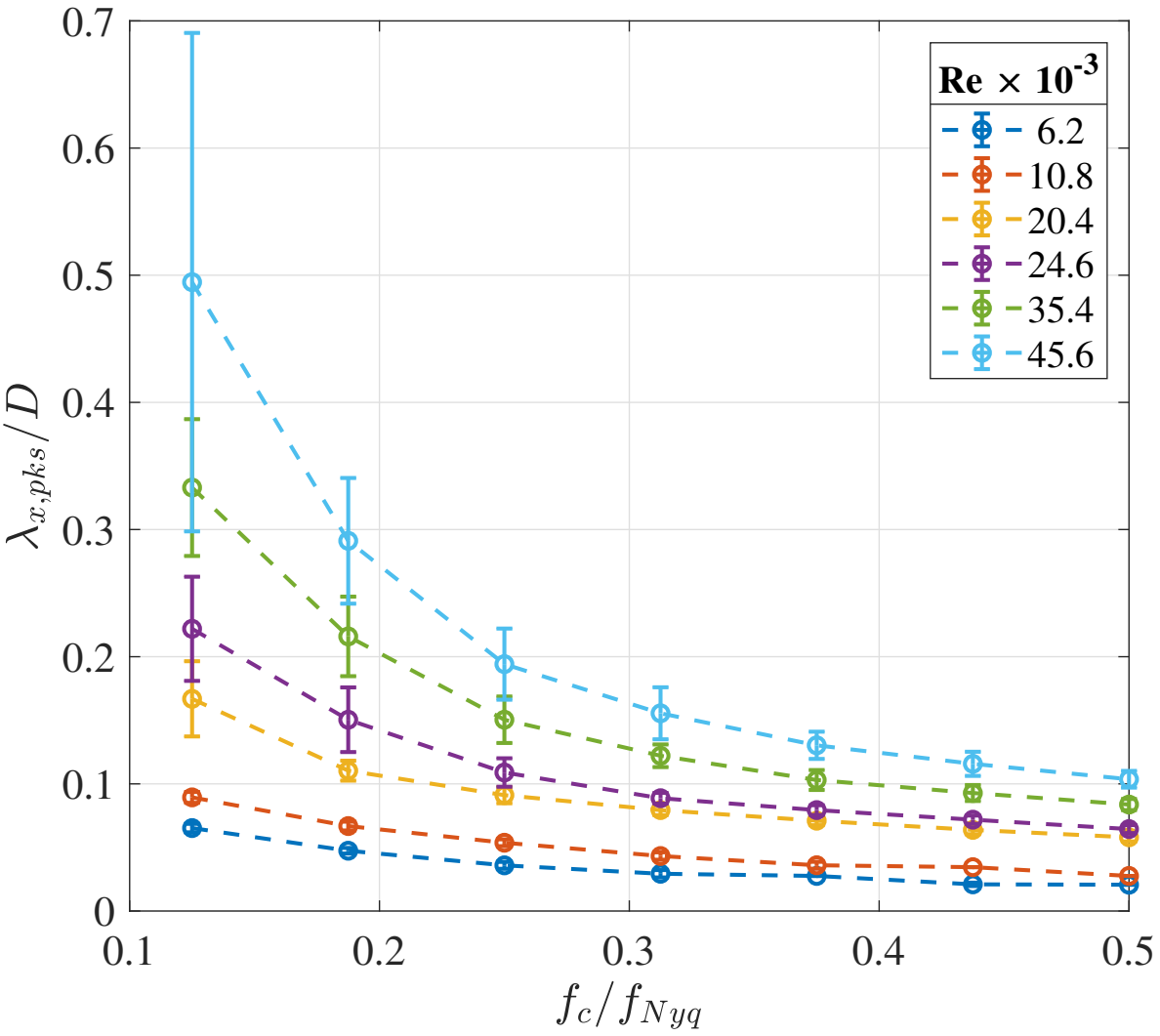

Figure 3.49: Streamwise length scales as measured through auto correlation peak-to-trough of $\lambda_{x,pks}/D$ plotted against f_c/f_{Nyq} for different Reynolds Numbers. $f_w/f_{Nyq} = 0.016$ for this set.

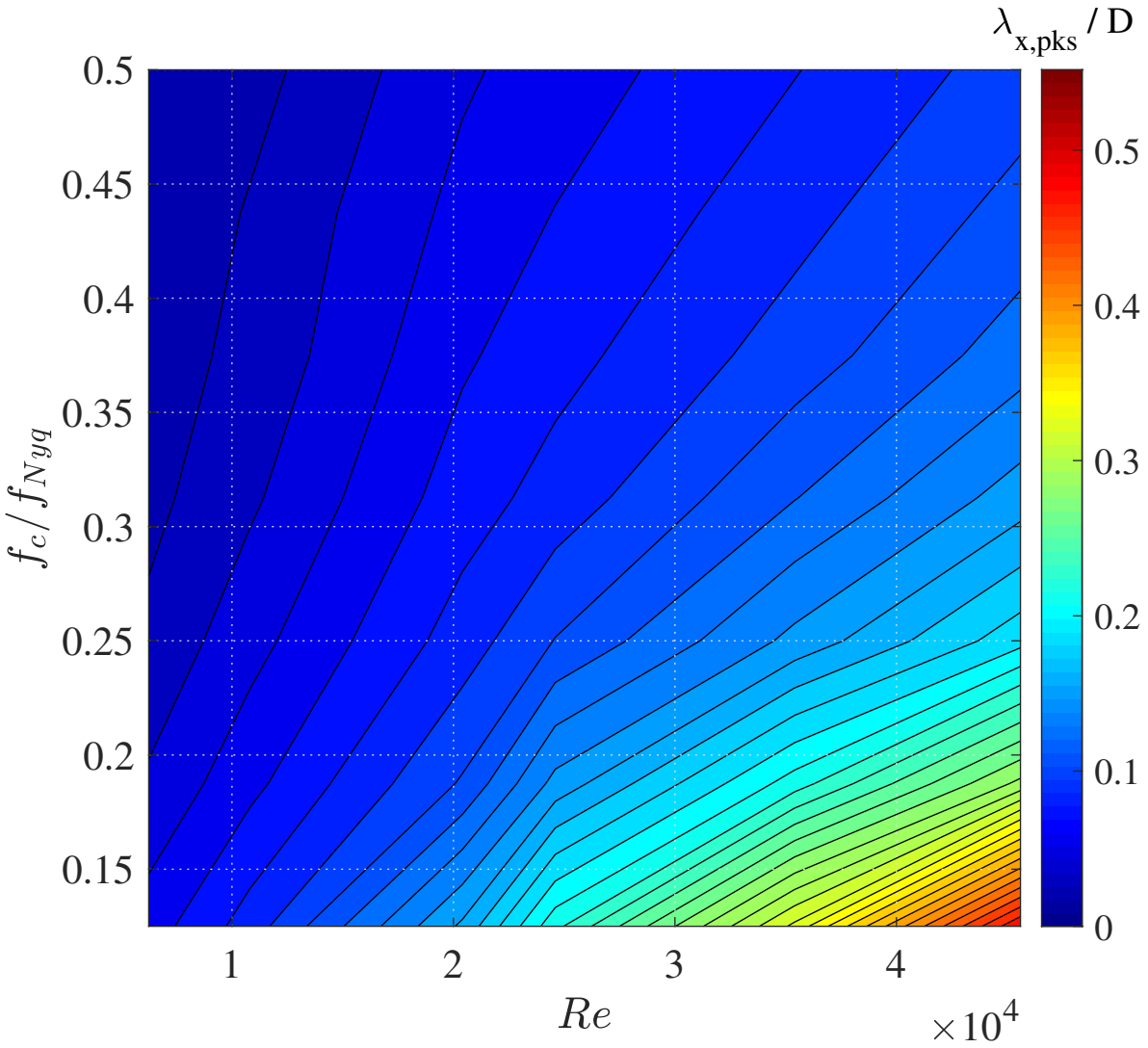

Figure 3.50: Flooded contour plot illustrating streamwise length scales as measured through auto correlation peak-to-trough of $\lambda_{x,pks}/D$ as a function of f_c/f_{Nyq} and Reynolds Numbers, Re. $f_w/f_{Nyq} = 0.016$ for this set.

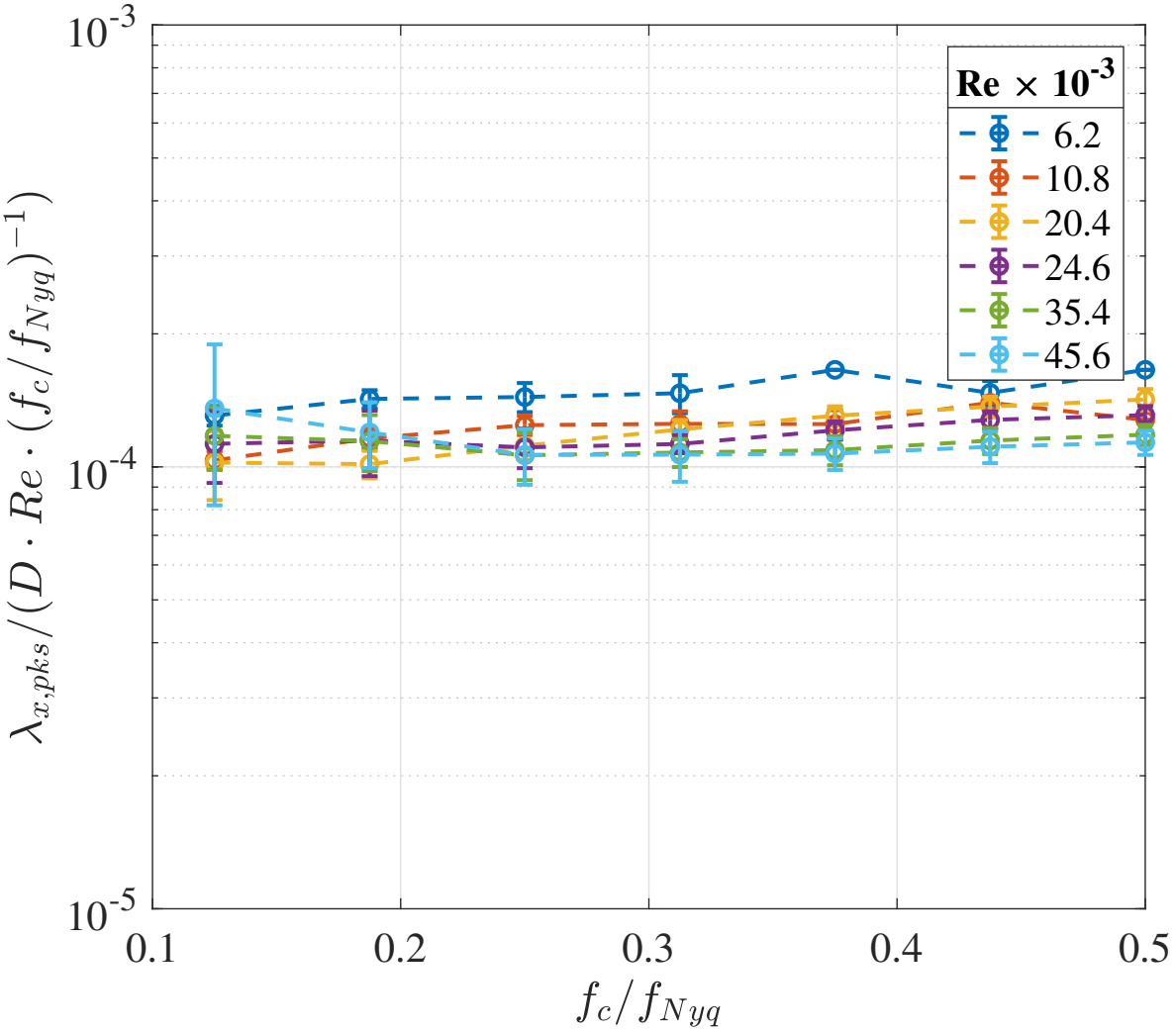

Figure 3.51: Normalized streamwise length scales as measured through auto correlation peak-to-trough of $\lambda_{x,pks}/\left(D \cdot Re \cdot (f_c/f_{Nyq})^{-1}\right)$ plotted against f_c/f_{Nyq} for different Reynolds Numbers. $f_w/f_{Nyq} = 0.016$ for this set.

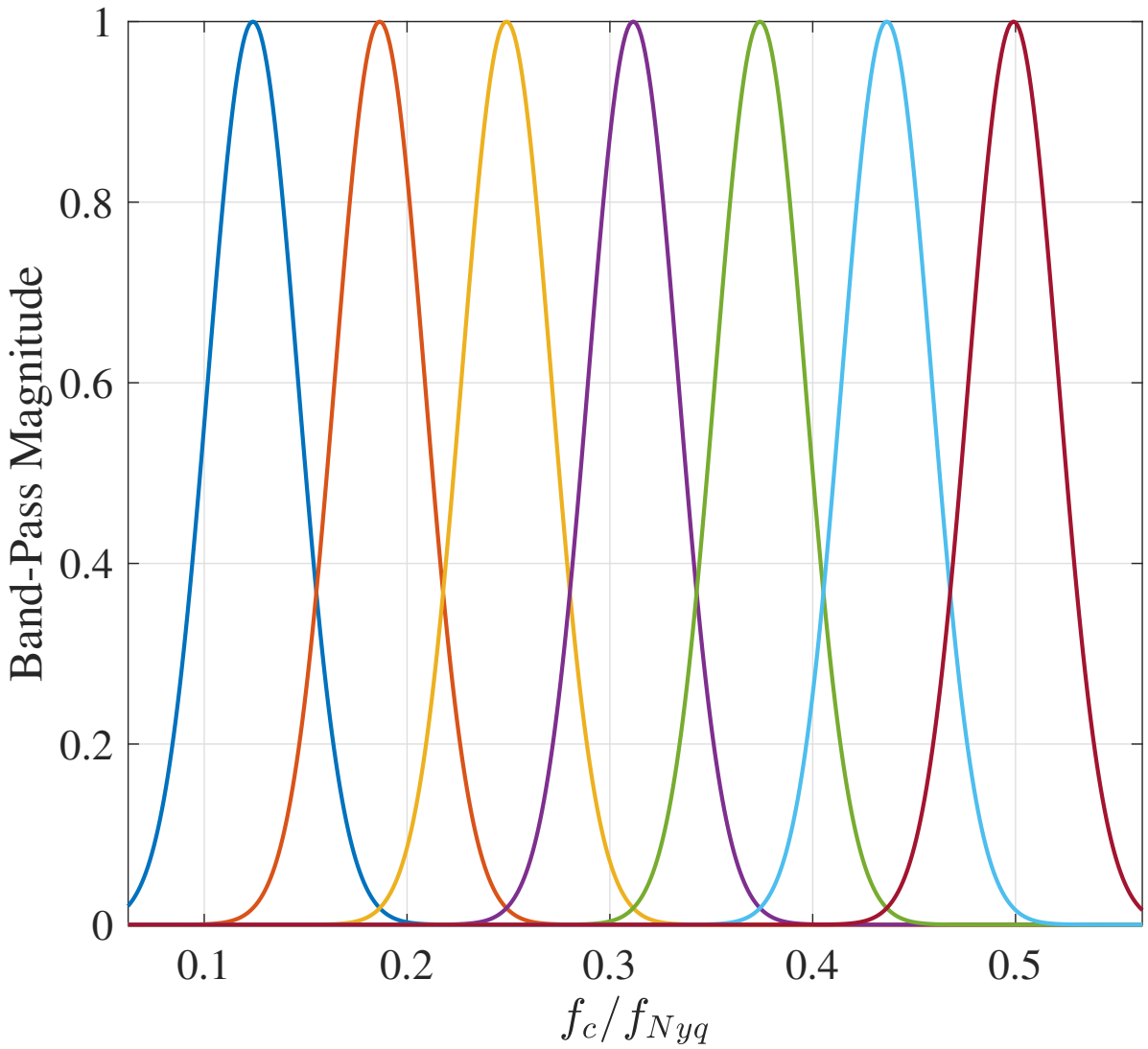

Figure 3.52: Illustration of band-pass filters used in PixTiF process - demonstration the centers and the widths normalized by the Nyquist Frequency associated with the image capture rate, $f_w/f_{Nyq} = 0.031$.

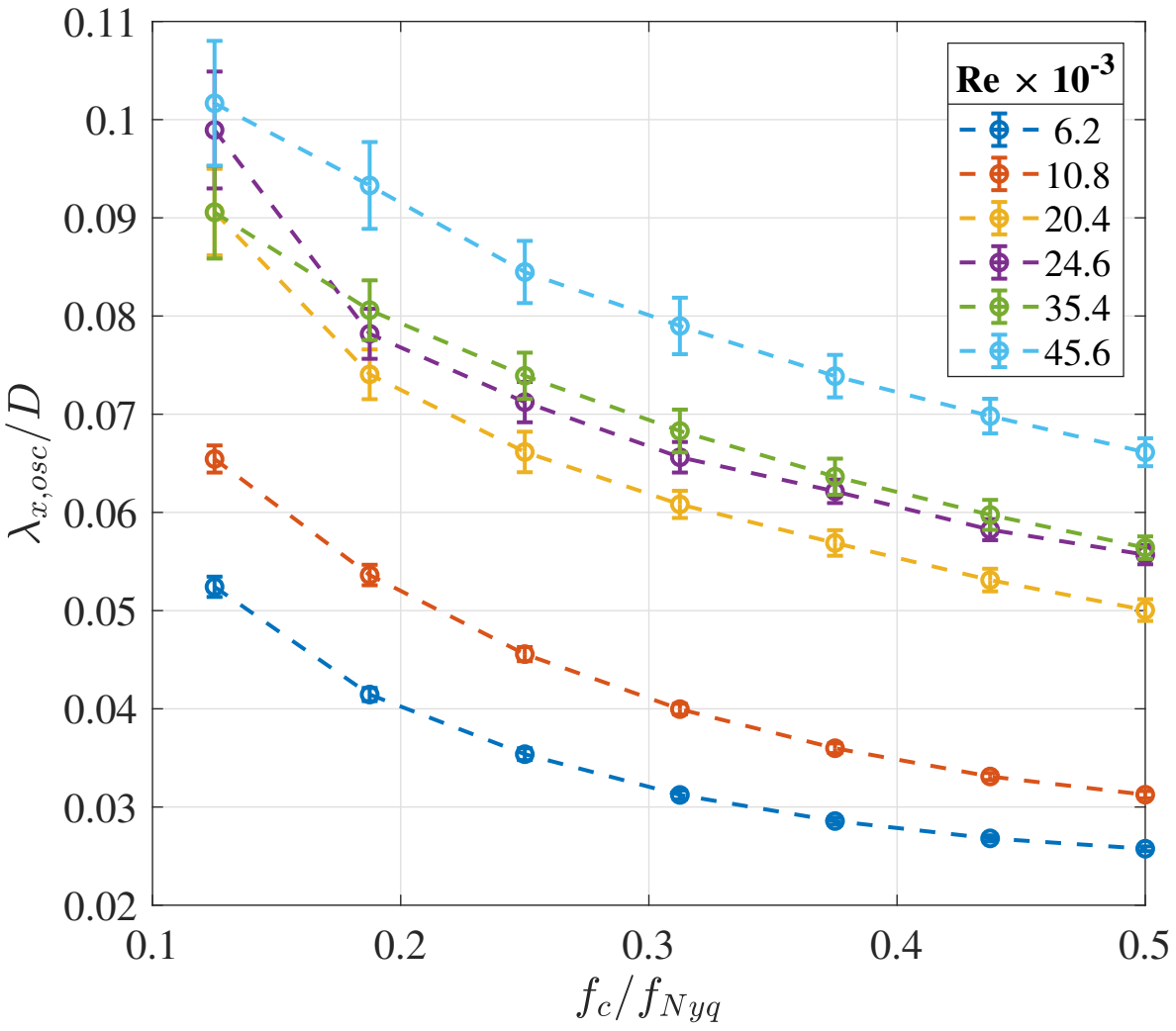

Figure 3.53: Streamwise length scales as measured through auto correlation osculating parabola of $\lambda_{x,osc}/D$ plotted against f_c/f_{Nyq} for different Reynolds Numbers. $f_w/f_{Nyq} = 0.031$ for this set.

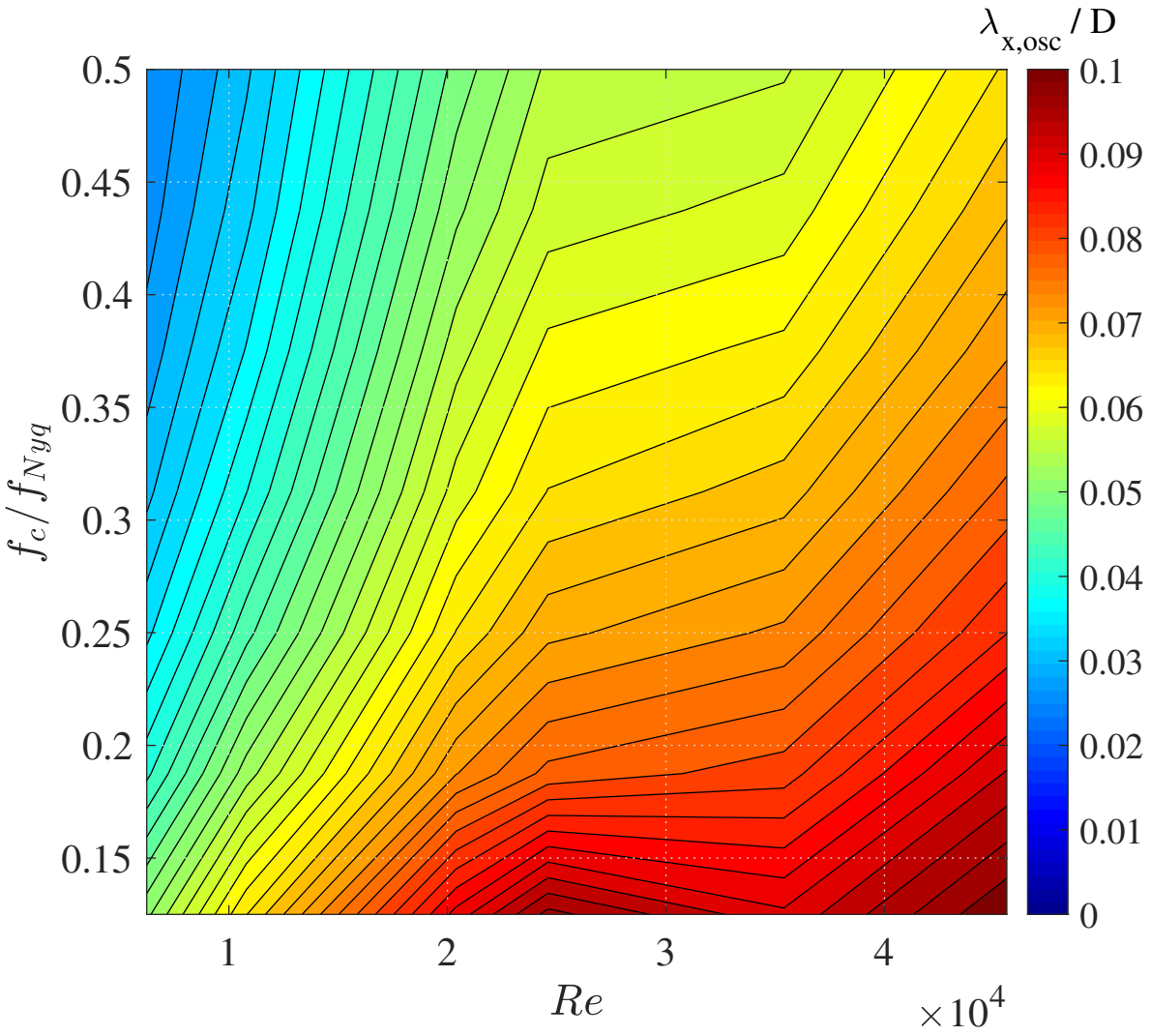

Figure 3.54: Flooded contour plot illustrating streamwise length scales as measured through auto correlation osculating parabola of $\lambda_{x,osc}/D$ as a function of f_c/f_{Nyq} and Reynolds Numbers, Re. $f_w/f_{Nyq} = 0.031$ for this set.

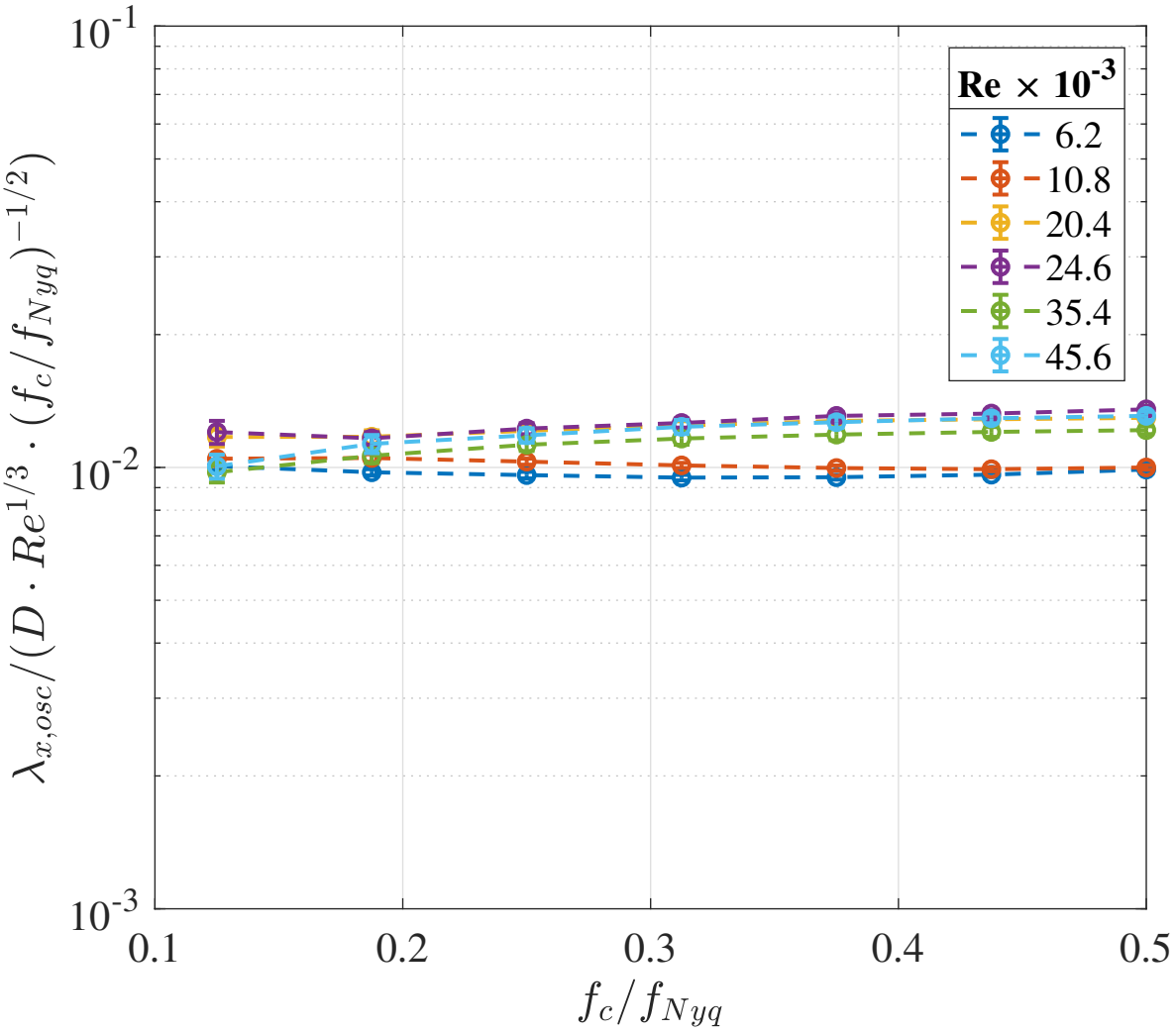

Figure 3.55: Normalized streamwise length scales as measured through auto correlation osculating parabola of $\lambda_{x,osc}/\left(D{\cdot}Re^{1/3}{\cdot}(f_c/f_{Nyq})^{-1/2}\right)$ plotted against f_c/f_{Nyq} for different Reynolds Numbers. $f_w/f_{Nyq} = 0.031$ for this set.

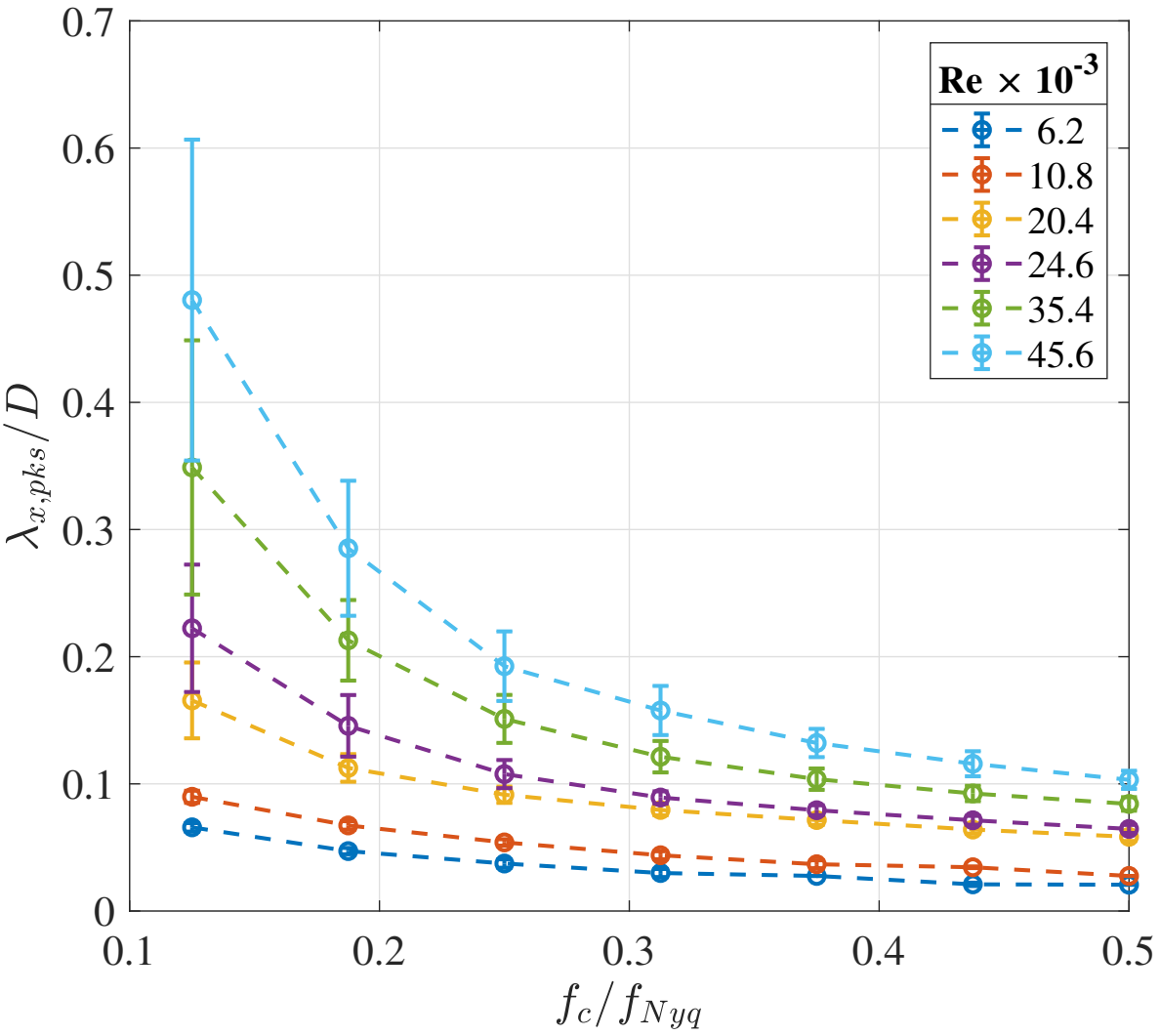

Figure 3.56: Streamwise length scales as measured through auto correlation peak-to-trough of $\lambda_{x,pks}/D$ plotted against f_c/f_{Nyq} for different Reynolds Numbers. $f_w/f_{Nyq} = 0.031$ for this set.

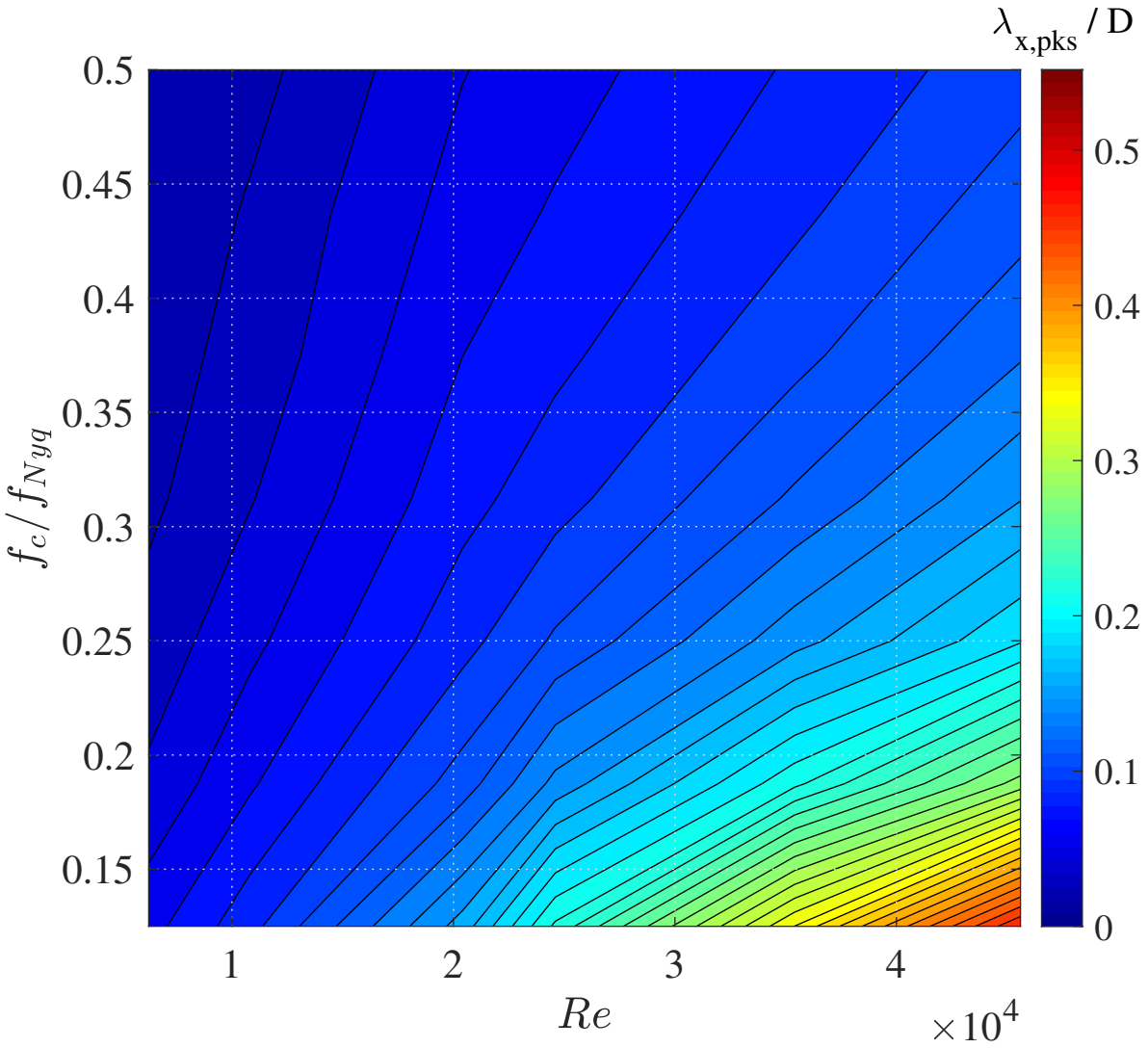

Figure 3.57: Flooded contour plot illustrating streamwise length scales as measured through auto correlation peak-to-trough of $\lambda_{x,pks}/D$ as a function of f_c/f_{Nyq} and Reynolds Numbers, Re. $f_w/f_{Nyq} = 0.031$ for this set.

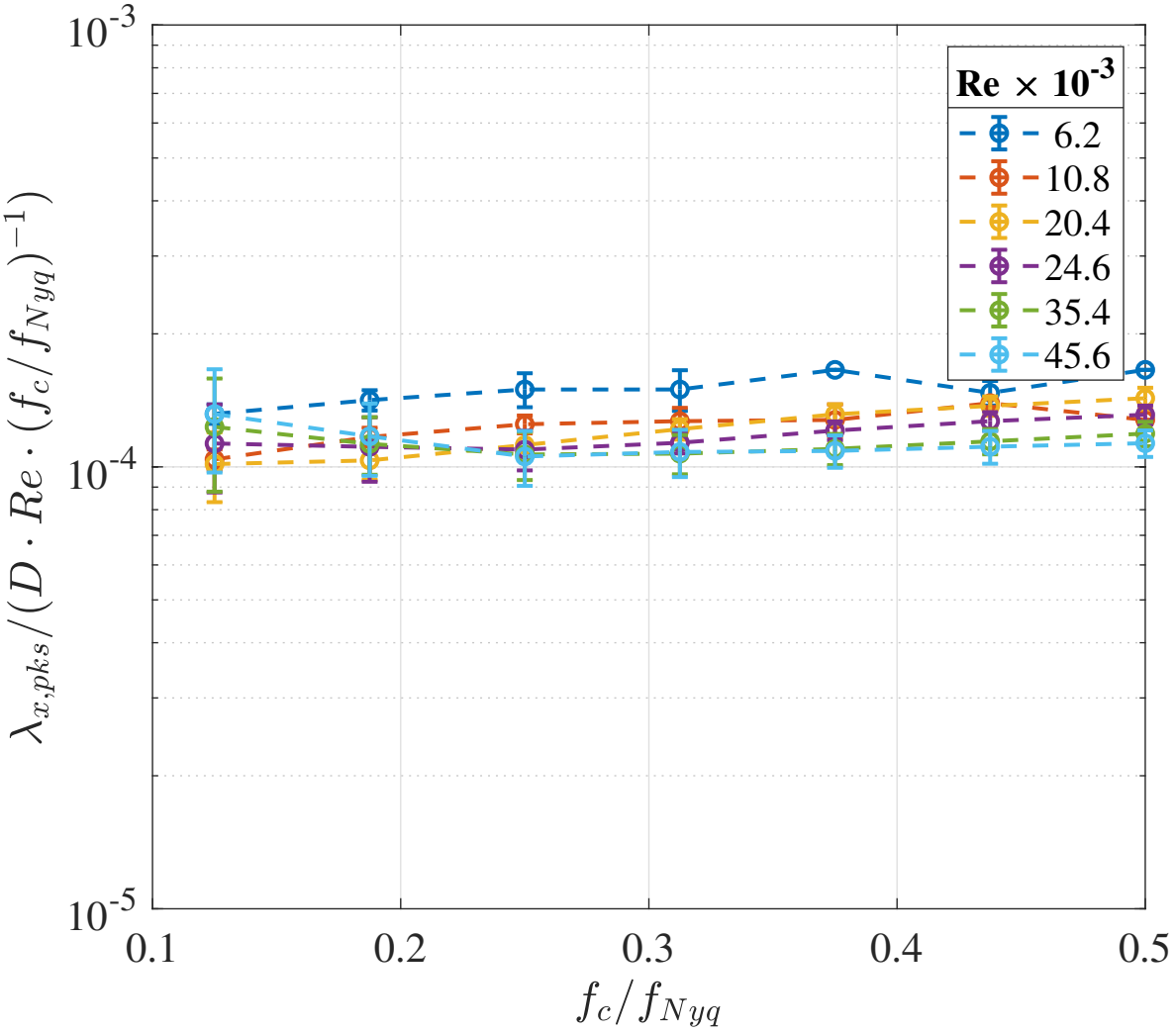

Figure 3.58: Normalized streamwise length scales as measured through auto correlation peak-to-trough of $\lambda_{x,pks}/\left(D \cdot Re \cdot (f_c/f_{Nyq})^{-1}\right)$ plotted against f_c/f_{Nyq} for different Reynolds Numbers. $f_w/f_{Nyq} = 0.031$ for this set.

Chapter 4

Oil Jets In Water

4.1 Oil Jets: 1cS

4.1.1 Edge Visualization

Figure 4.1 shows sample flow images for 1cS-oil jets at three Reynolds numbers: 0.4×10^4, 2.4×10^4 and 4.0×10^4. The flow in the tube upstream of the discharge orifice of the jet is expected to be transitional since it is tripped by a screen mesh, and the Reynolds number is about 4000. The combined effects of the immiscibility of the jet and ambient liquids, augmented by the expected transitional nature of the discharge flow, results in large detached parcels of oil after a short distance of undulations. As the Reynolds number is increased by six-fold in frame (b), the discharge tube length becomes adequate to achieve turbulent flow at the exit of the tube. The flow leaving the tube now shows streamwise features, namely, the wall signatures of the turbulent flow in the pipe. Further increase in the Reynolds number in frame (c) results in finer details as expected: both on the jet surface and in the size distribution of the detached oil droplets.

Figure 4.2 shows averages of 2048 images for 1cS-oil jet at the three Reynolds numbers. The transitional nature of the jet results in a contraction of the jet width soon (about 1 to 2 jet exit diameters) after discharge, followed by a barrel formation in frame (b). The averaged pictures at higher Reynolds numbers in frames (b) and (c) indicate a classical jet divergence, at a slightly smaller cone angle in (b).

4.1.2 Shadowgraphy

Figure 4.3 shows simultaneous shadowgraph images corresponding to the snapshots in figure 4.1. Due to the large difference between the refractive indices of water and oils, the oil jets appear nearly black in the shadowgraph pictures. The shadowgraph images are taken at a noticeably lower magnification, hence the features in the visible images look smaller in the shadowgraph images. At the lowest Reynolds number in (a), the flow field is fragmented, seemingly a collection of large oil patches. The discharging jet shows a combination of sinuous and varicose instabilities. At the higher Reynolds numbers, the flows exhibit less disorderly patterns. The detached oil packets are clearly visible as oil droplets of various sizes, mostly spherical. On examination of the corresponding video sequences, one can clearly identify oscillations in the shapes of the largest droplets. At the highest Reynolds number in frame (c), the observed average droplet size gets smaller.

Figure 4.4 shows an averaged shadowgraph image corresponding to the averaged pictures in figure 4.2. The averaged picture at the lowest Reynolds number in frame (a) nearly duplicates its counterpart in figure 4.2(a). The jet maintains a nearly uniform width, with a slight oscillation that has a wavelength of approximately three diameters. The mean shadowgraph images in (b) and (c) nearly match the corresponding visible images in figure 4.2. The mean shapes of the jets are now better revealed. The highest Reynolds number jet spreads at a slightly larger divergence angle.

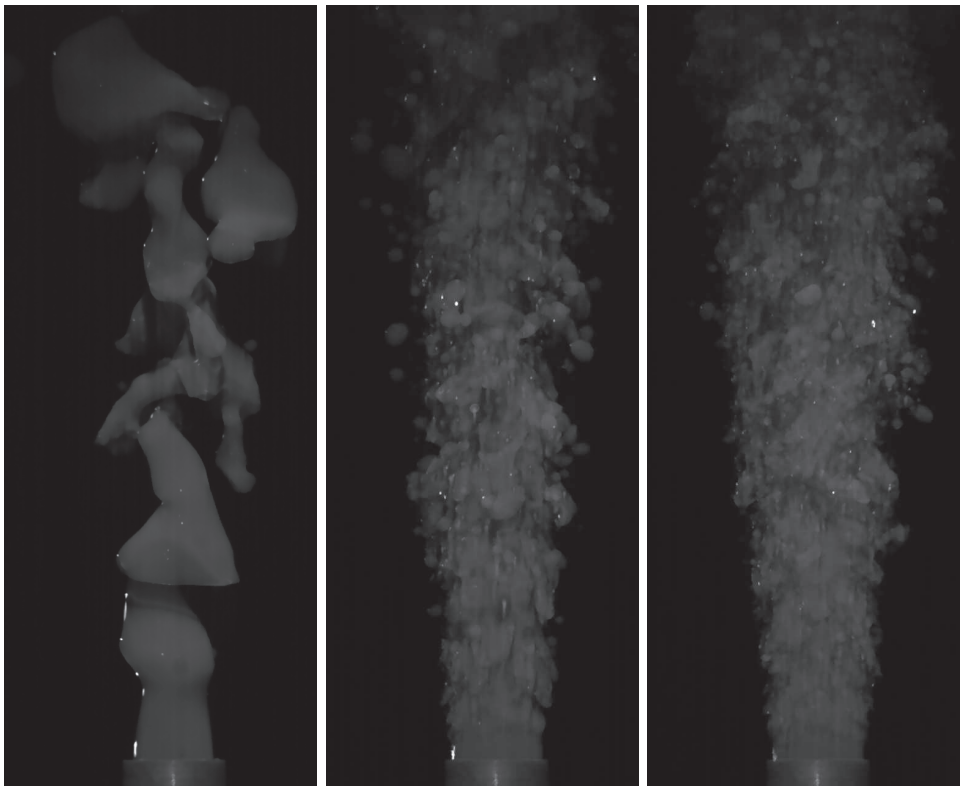

(a) Re = 0.40×10^4 (b) Re = 2.41×10^4 (c) Re = 4.02×10^4

Figure 4.1: The 1cS silicone oil jet experiments: instantaneous images. Flows 19, 21 & 23.

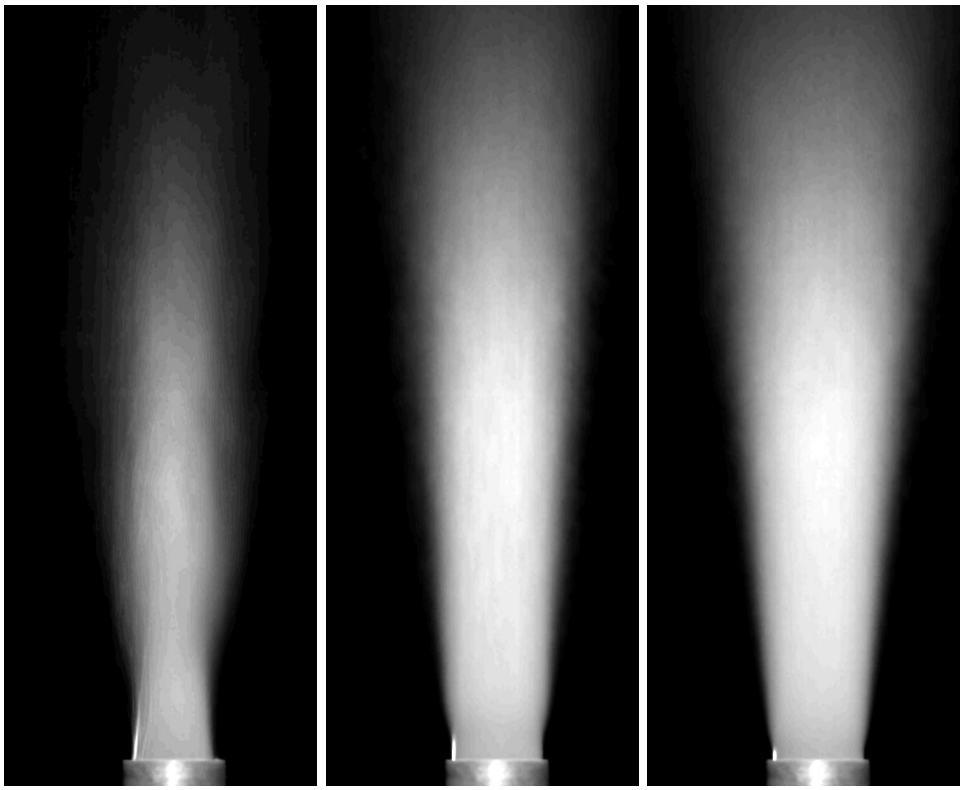

(a) Re = 0.40×10^4 (b) Re = 2.41×10^4 (c) Re = 4.02×10^4

Figure 4.2: The 1cS silicone oil jet experiments: averages of 2048 images: Flows 19, 21 & 23.

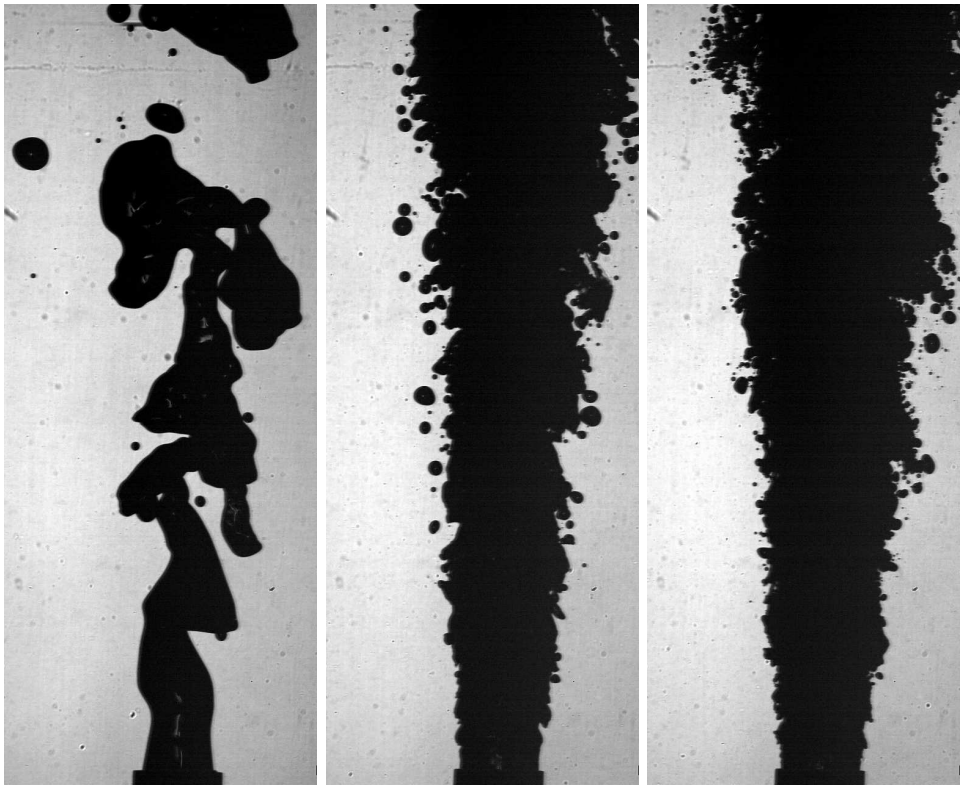

(a) Re = 0.40×10^4 (b) Re = 2.41×10^4 (c) Re = 4.02×10^4

Figure 4.3: Shadowgraph images of 1cS silicone oil jet experiments: instantaneous images corresponding to the frames in figure 4.1. Flows 19, 21 & 23.

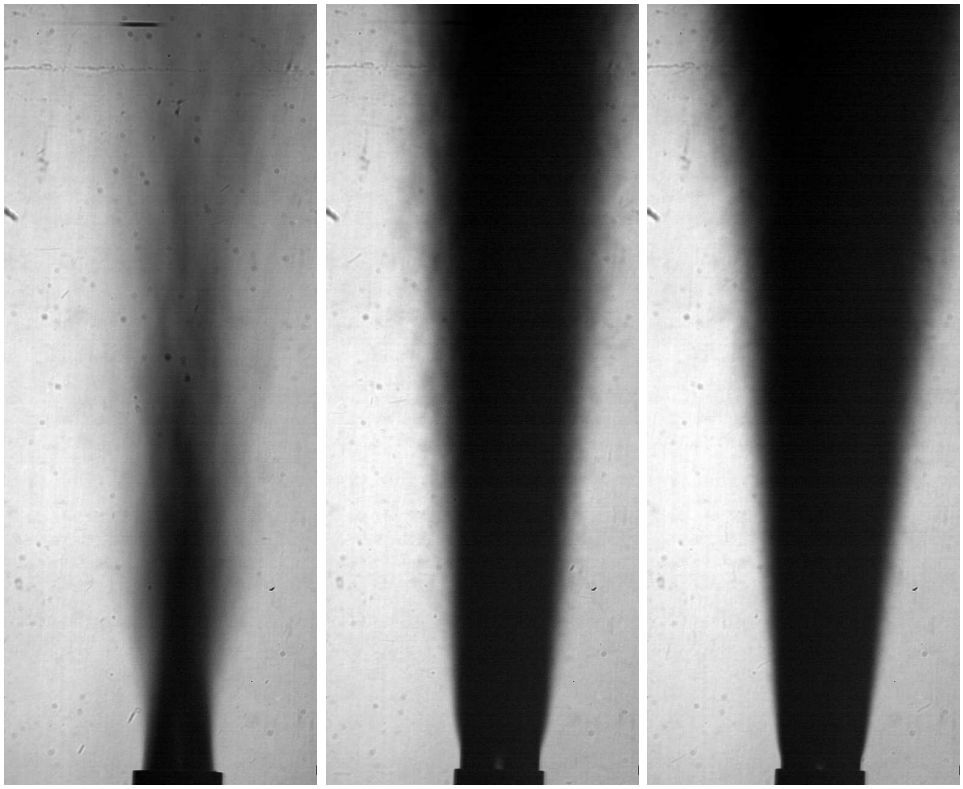

(a) Re = 0.40×10^4 (b) Re = 2.41×10^4 (c) Re = 4.02×10^4

Figure 4.4: Shadowgraph images of 1cS silicone oil jet experiments: intensity averages of 2048 images corresponding to the frames in figure 4.2: Flows 19, 21 & 23.

4.2 Oil Jets: 5cS

4.2.1 Edge Visualization

Figure 4.5 shows sample flow images for 5cS-oil jet at three Reynolds numbers. The flow in the tube shown in frame (a) is expected to have nearly developed into a laminar parabolic profile since the Reynolds number is about 800, below its critical value in tube with $L/D \approx 32$. This distance has been shown to be adequate for reaching fully developed laminar flow [Nikuradse(1932)]. The jet fluid in water still maintains contiguity in the field of view despite large undulations. At the higher Reynolds numbers, the oil jets breaks up and droplets form at the edge of the jet. The average size of the droplets and the surface features get smaller as the Reynolds number increases from frame (b) to (c).

Perhaps an unexpected observation is that the 5cS-oil jet at $Re \approx 8000$ in figure 4.5(c) shows finer scales than the 1cS-oil jet at $Re \approx 24,000$ in figure 4.1(b). Figure 4.6 shows averages of 2048 images for 5cS-oil jet at three Reynolds numbers. At the lowest Reynolds number in frame(a), the jet shows almost no spread. As in the case of figure 4.2(a), there are hints of undulations in the shape of the jet. At the higher Reynolds numbers, the 5cS-oil jets grow at a slightly greater rate, as seen in frame(c).

4.2.2 Shadowgraphy

Figure 4.7 shows shadowgraph images corresponding to the snapshots in figure 4.5. As in the visible pictures, the jet fluid at the lowest Reynolds number remains contiguous, with varicose instability at the discharge. At higher Reynolds numbers, the jet surface breaks up into droplets, with decreasing size and increasing number density at the highest Reynolds number, which corroborates the features seen in figure 4.5(b,c).

Figure 4.8 shows average shadowgraph images corresponding to the average pictures in figure 4.6. At the lowest Reynolds number flow, the jet discharges without much growth. Also, hints of the varicose instability are visible near the pipe exit plane. The averaged images in frames (b) and (c) are similar to those in figure 4.4(b, c) except for a slightly larger spreading angle.

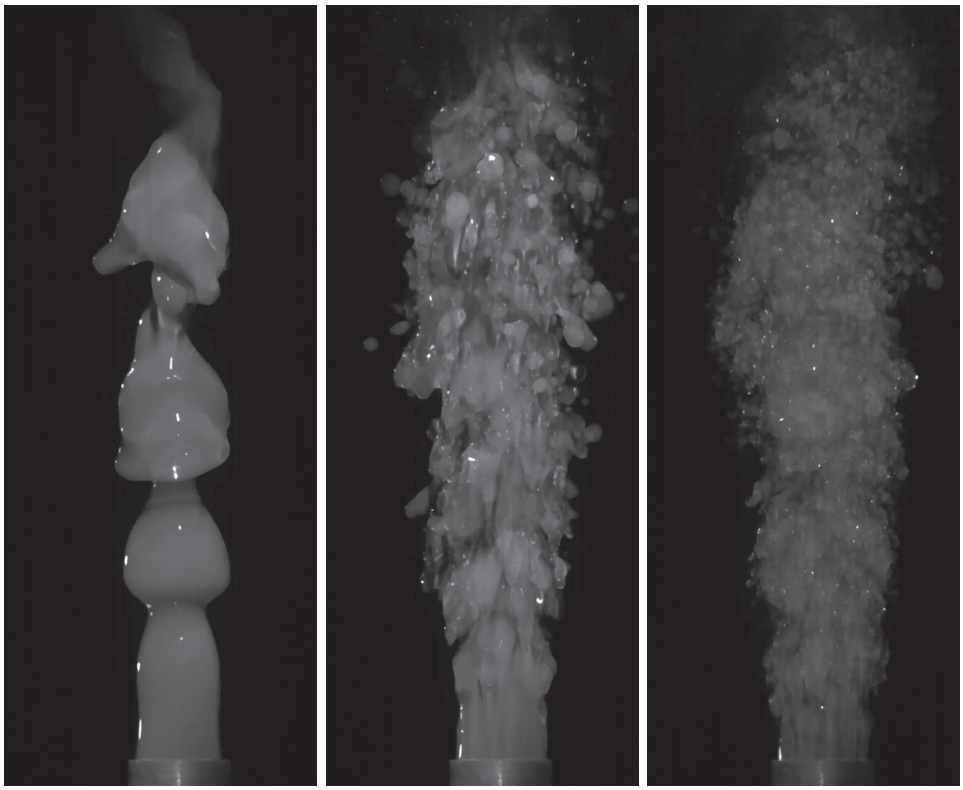

(a) $\mathrm{Re} = 0.80 \times 10^3$ (b) $\mathrm{Re} = 4.02 \times 10^3$ (c) $\mathrm{Re} = 8.03 \times 10^3$

Figure 4.5: The 5cS silicone oil jet experiments: instantaneous images. Flows 24, 26 & 29.

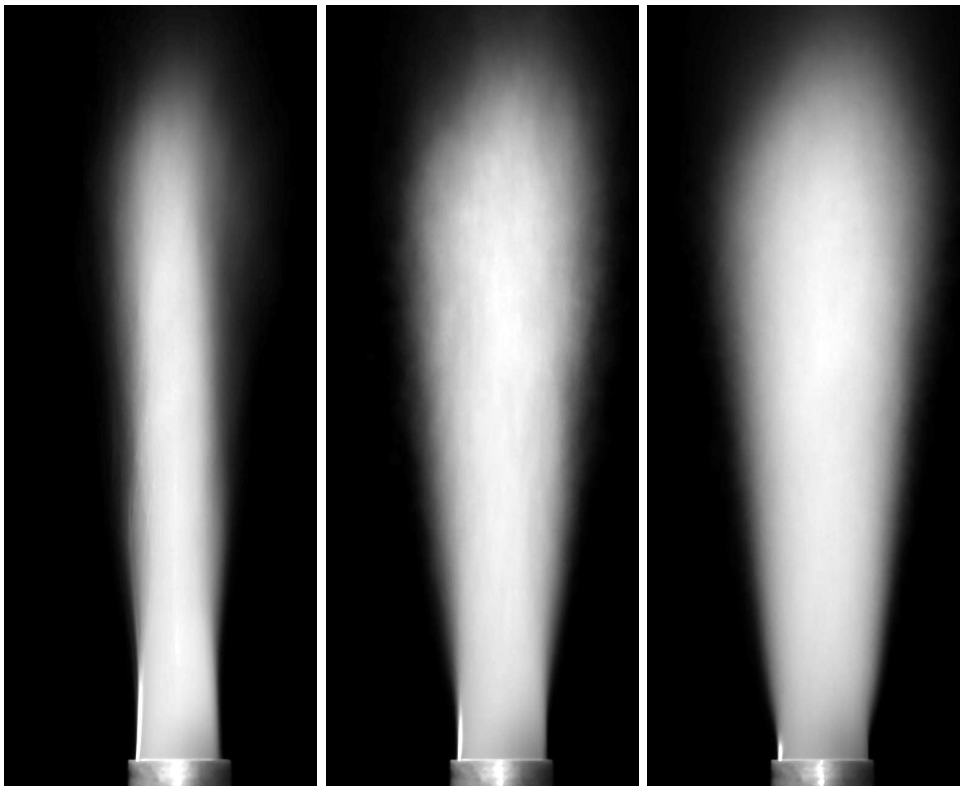

(a) Re = 0.80×10^3 (b) Re = 4.02×10^3 (c) Re = 8.03×10^3

Figure 4.6: The 5cS silicone oil jet experiments: averages 2048 images: Flows 24, 26 & 29.

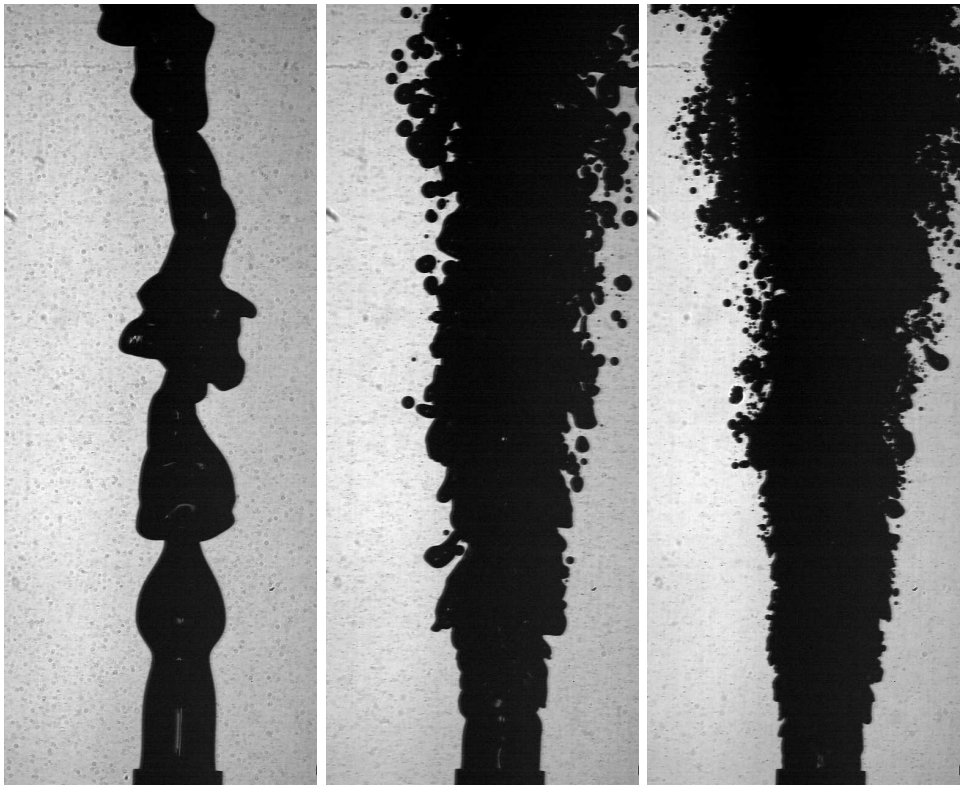

(a) $\mathrm{Re} = 0.80 \times 10^3$ (b) $\mathrm{Re} = 4.02 \times 10^3$ (c) $\mathrm{Re} = 8.03 \times 10^3$

Figure 4.7: Shadowgraph images of 5cS silicone oil jet experiments: instantaneous images corresponding to the frames in figure 4.5: Flows 24, 26 & 29.

(a) Re = 0.80×10^3 (b) Re = 4.02×10^3 (c) Re = 8.03×10^3

Figure 4.8: Shadowgraph images of 5cS silicone oil jet experiments: averages of 2048 images corresponding to the frames in figure 4.6: Flows 24, 26 & 29.

4.3 Interfacial Length Scales

Similar to figure 3.14 for the water jets, figures 4.9 and 4.10 show the results of the CLAHE process on the 1cS and 5cS silicone oil jets, respectively. For both oils, the visible scales seem uniform along the jet and get progressively finer with increasing flow rate (Reynolds number), albeit nonisotropic. What is intriguing is that the visible scales on the edge of the 5cS-oil jet in figure 4.10 are smaller than those of the 1cS-oil jets in figure 4.9, despite the 5cS-oil jets having Reynolds numbers that are an order of magnitude smaller.

Again, similar to the processing described in §3.3 and shown in figure 3.18 for interface scales on the water jets, figure 4.11 shows the interfacial length scale analyses for the 1cS-oil jet. Shown in the figure is a 256×256-pixel interrogation tile centered at $x/D = 3.42$ of the 1cS-oil jet for $Re = 2.41 \times 10^4$. In contrast to the water jet, the oil jet shows streamwise ligamentations in frame (a). The length scales extracted from the autocorrelation curves in frame (e) show a longer length scale in the streamwise direction than in the cross-stream direction. The same process is applied to the 5cS-oil jet for $Re = 8.45 \times 10^3$; the zero crossings for the cross-stream and streamwise osculating parabolas are smaller than the lower Reynolds number 1cS-oil jet. As in figure 4.11, the length scale in the streamwise direction is larger than that in the cross-stream direction for the 5cS-oil jets.

Figure 4.13 summarizes the interfacial length scale measurements for the oil jets. The ratio of the length scales λ_x/λ_y are shown in frames (a & c) and the average length scales λ in frames (b & d). Unlike the homogeneous water jets, the streamwise length scales in the oil jets at the interface are substantially larger than those in the cross-stream direction, quantifying the visual observations in figure 4.9 and 4.10. The elongation of oil droplets prior to the detachment of small trailing droplets may be a contributing factor in the differences between scales. The length scales for both oil jets are smaller than those of the water jets in figure 3.19. The scales are nearly uniform over the range studied here and monotonically decrease with Reynolds number. As stated earlier, the length scales for the 5cS-oil jet are smaller that those for the 1cS-oil jet.

Within the near fields investigated, the effects of buoyant forces are neglected when compared to the inertial forces within the domain. The Morton lengths (2.6) for these oil jet experiments are greater than the field of view (FOV). Within this region, the droplets are not expected to experience significant acceleration due to buoyancy. As noted earlier in table 2.1, the interfacial tension of 5cS-oil in water is lower than that of the 1cS-oil. This provides a likely reason for the presence of finer scales in the 5cS-oil jet runs, even at lower Reynolds numbers.

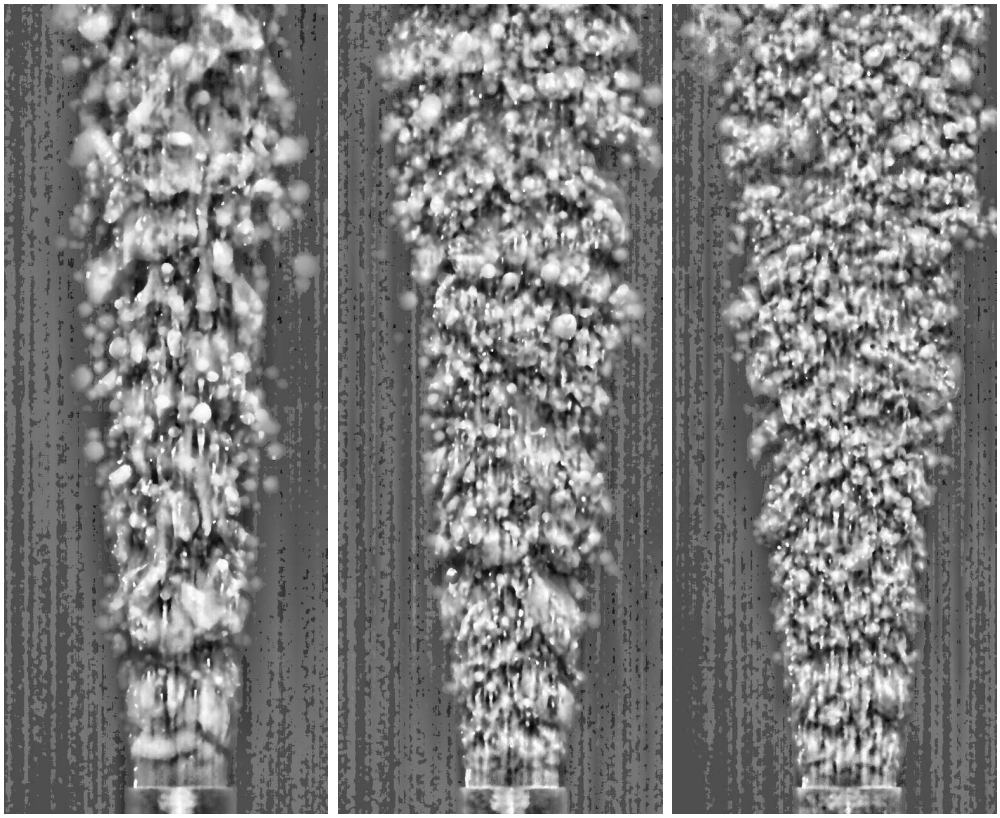

(a) $Re = 2.32 \times 10^4$ (b) $Re = 3.36 \times 10^4$ (c) $Re = 4.21 \times 10^4$

Figure 4.9: Sample images of CLAHE on 1cS-oil jets.

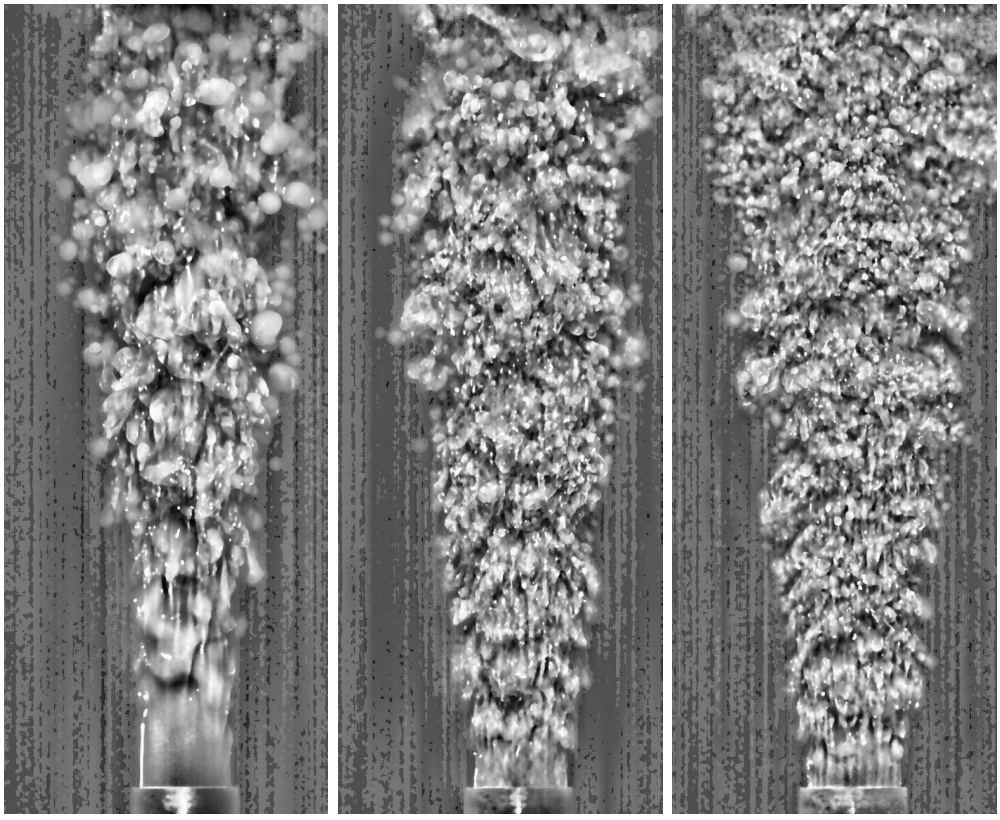

(a) $Re = 4.22 \times 10^3$ (b) $Re = 5.83 \times 10^3$ (c) $Re = 8.45 \times 10^3$

Figure 4.10: Sample images of CLAHE on 5cS-oil jets.

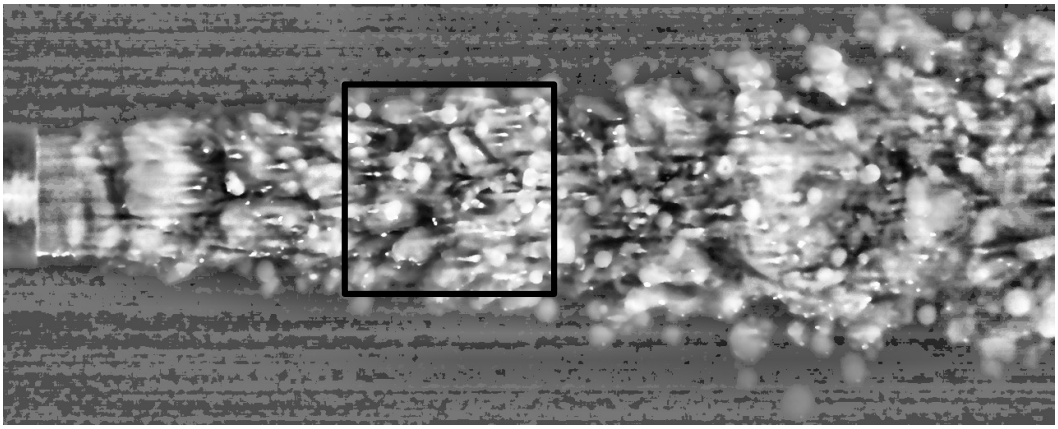

(a)

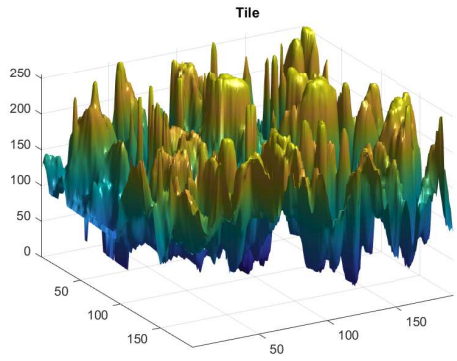

(b)

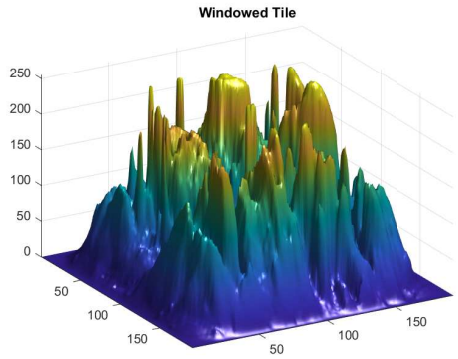

(c)

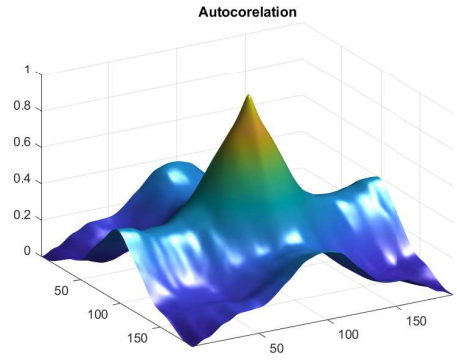

(d)

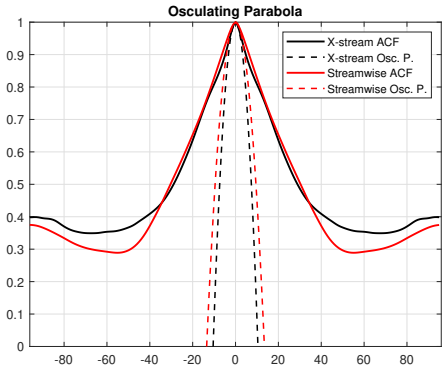

(e)

Figure 4.11: Processing steps for the interrogation region of the 1cS silicone oil jet at $Re = 2.41 \times 10^4$ at $x/d = 3.42$, (a) location of the interrogation region along the jet, (b) raw intensity array, (c) intensity array after 2D Tukey windowing , (d) autocorrelation of the windowed intensity array, and (e) the cross-stream (red dashed) and streamwise (black dashed) osculating parabolas to the autocorrelation surface (solid lines with same respective colors).

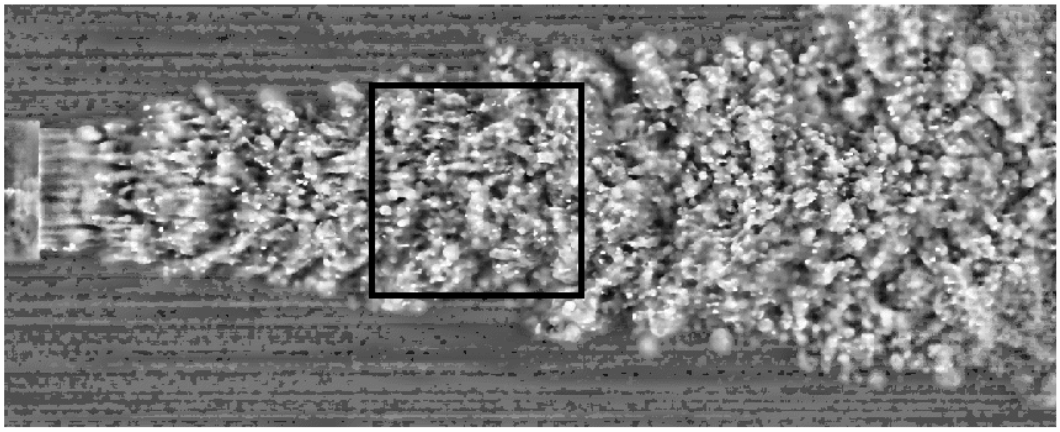

(a)

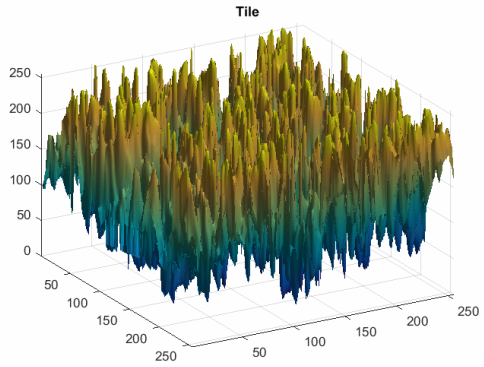

(b)

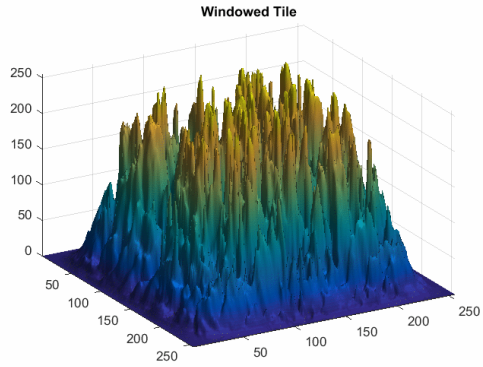

(c)

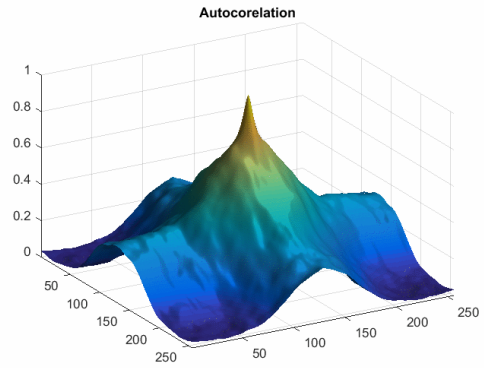

(d)

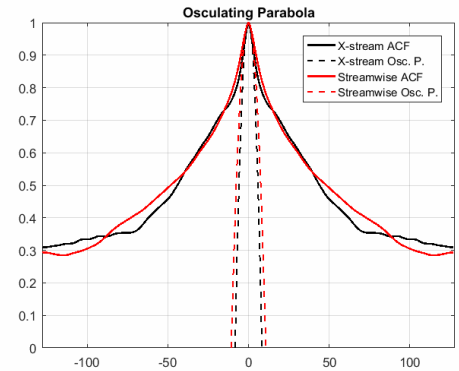

(e)

Figure 4.12: Processing steps for the interrogation region of the 5cS silicone oil jet at $Re = 8.45 \times 10^3$ at $x/d = 3.89$, (a) location of the interrogation region along the jet, (b) raw intensity array, (c) intensity array after 2D Tukey windowing , (d) autocorrelation of the windowed intensity array, and (e) the cross-stream (red dashed) and streamwise (black dashed) osculating parabolas to the autocorrelation surface (solid lines with same respective colors).

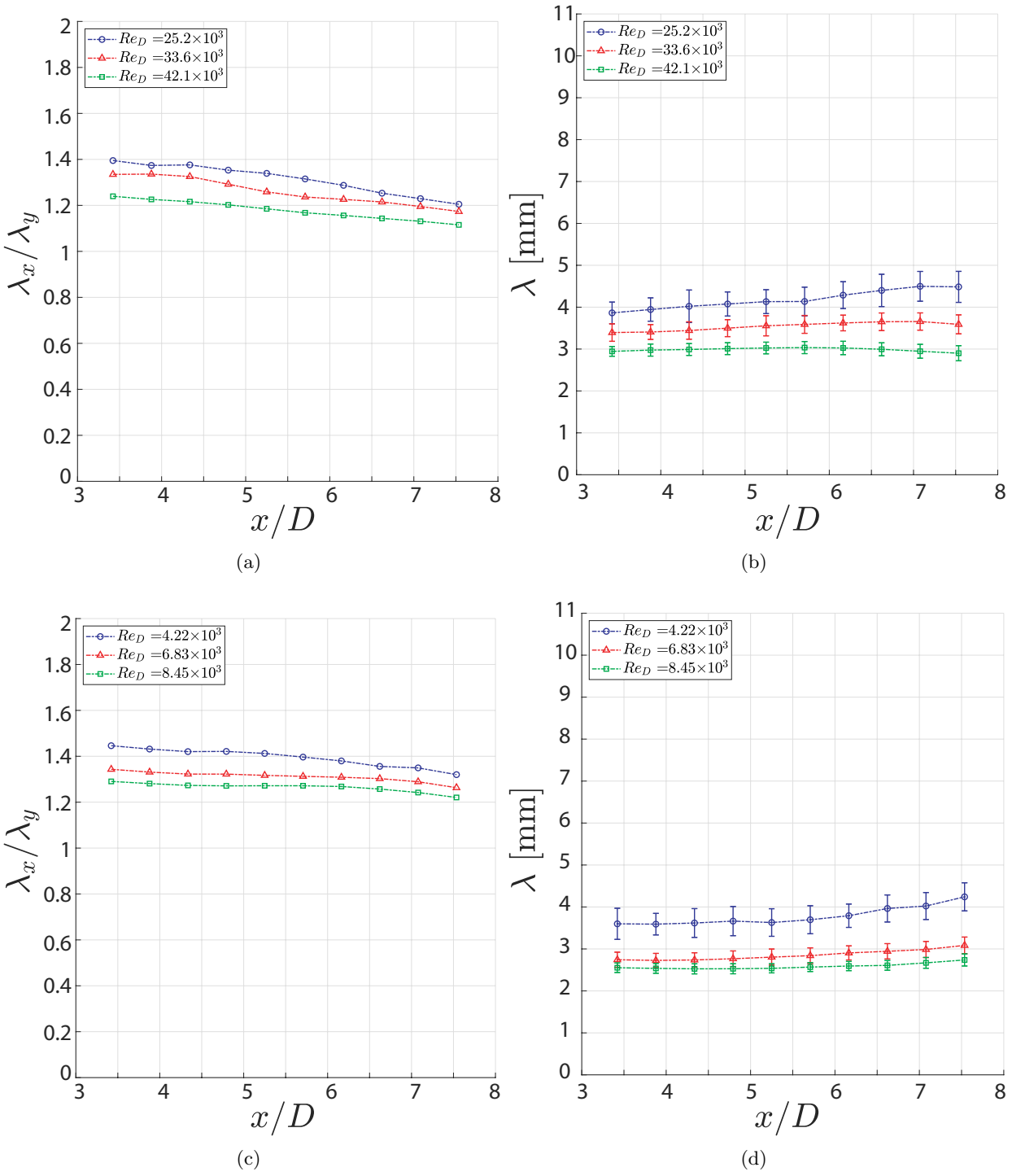

Figure 4.13: Interfacial length scale results for oil jets: (a, b) 1cS silicone oil and (c, d) 5cS silicone oil. (a, c) length ratios λ_x/λ_y and (b, d) mean length scales $\lambda = (\lambda_x + \lambda_y)/2$.

4.4 Hough Transformation For Oil Droplet Size

The large differences in the indices of refraction between oil jets and the surrounding water (table 2.1) make the cores of the jets inaccessible in shadowgraph imaging. However, the oil droplets forming at the edges of the jets are clearly recorded by the shadowgraphs (figures 4.3 and 4.7). The nearly spherical shapes and sharp contrast of the oil droplets allows these data sets to be processed using a Circular Hough Transformation (CHT) to estimate the droplet diameters at the interfaces of the oil jets and the ambient water. The CHT is a variation of the process detailed in a patent by [Hough(1962)], who presents a method for detection of complex patterns. The method is turned into a general scheme by [Duda & Hart(1972)] that is readily applied in detecting circular features. We have employed a variation to the standard CHT proposed by [Atherton & Kerbyson(1993)] which increases its computational efficiency. During the implementation of the CHT, raw oil jet images are first cropped to 768×256 pixels: spanning $x/D = 3.5 - 8.5$ and extending from the center of the jet into the ambient water. Then, the size of the cropped images are rescaled using a bilinear interpolation. This is done to mitigate the limitations of the CHT in detecting small objects (with radii less than 5 pixels). Using the CHT on the larger image size does increase the processing cost, but allows for the consistent detection of droplets for the higher Reynolds number flows.

[Atherton & Kerbyson(1993)] proposed a variation to the standard CHT, requiring a 3D voting space. The third dimension is used for phase encoding; this can be accomplished using a 2D complex voting space. Here the local maximum magnitude of the accumulator array will be recorded as a possible center of a circle. The phase information stored as a complex value in the accumulator will hold the radius of the object, as estimated by a voting procedure.

The process is illustrated in figure 4.14. The re-sampled image is first processed using a Canny edge detection as was done for the homogeneous jets described earlier. The information subsequently stored is the edge magnitude, I_g (a metric of the strength of an edge), and the direction angle normal to the edge, Θ (see equation 3.3). Segments with low edge magnitudes are excluded from the *voting* process to determine circles. The remaining segments are considered as likely edge locations, denoted as $\mathbf{x}'$. They are used as starting locations from which to project line segments, $S(\mathbf{x}')$. The segment exists from R_{min} to R_{max} away from $\mathbf{x}'$ in the Θ direction. The relative intensity between the objects and the background is used to set which direction the line segment should be projected. For every pixel location, $\mathbf{x}$, in the re-sampled image, an accumulator space, $H(\mathbf{x})$, is initialized as zero. The value:

$$H(\mathbf{x}) = \sum_{\mathbf{x}' \in S(\mathbf{x})} I_g(\mathbf{x}') \exp\left(-2\pi i \frac{||\mathbf{x} - \mathbf{x}'||}{(R_{max} - R_{min})} \right)$$

is summed for all edge locations, $\mathbf{x}'$, in the accumulator space. Local maximum magnitudes in the accumulator space are noted as likely locations for the center of a circular feature. The complex value information is used to estimate the radius of that circular feature. This process is used to determine the centers of the dark oil drops with a lighter background. As the radius information is encoded for a range of radii investigated, this process was run for three radii ranges for all images processed per experiment. The estimated radii are scaled to account for the re-sampling of the image.

Sample results from this analysis are shown in figure 4.15 for the 1cS-oil jets and in figure 4.16 for the 5cS-oil jets. Droplets identified through CHT are circles in color. As expected, each

sample frame shows a range of droplet sizes. Also as expected for both oils, the droplet sizes get smaller with increasing Reynolds number. What was unexpected, perhaps, was finding that the higher viscosity oil jet had smaller droplet sizes.

Droplet size distributions for both jets are shown in figure 4.17, 1cS-oil jet on the left column and 5cS on the right. At all conditions presented, the distribution is bimodal: a nearly symmetric distribution with a mean value of about 2 pixels and an asymmetric distribution above 4 pixels. A close examination of the video sequences suggests that the small droplets (2-pixels in diameter) are the secondary droplets formed during the pinching process of the primary droplets. The primary droplets constitute the remainder of the size distributions in the figure (see, for example, figure 7 of [Taylor(1934)]). Figure 4.18 shows an image sequence taken from Flow 27 videos, showing the breakup of a ligament into primary and secondary droplets. The top row of the figure shows the raw images at the native resolution of the camera, while the bottom row shows the enhanced images using bilinear sampling at 1/4 pixel resolution to bring out the shapes of the flow features. Breakup of primary droplet ligaments into secondary droplets is also reported by [Zhao *et al.*(2016)] in their underwater oil jet experiments.

Scaling of the mean droplet size with the estimated Kolmogorov scale of the discharge flow, with the jet diameter and velocity, are shown in figure 4.19 against the Weber number. Figure 4.19(a)shows no obvious relation the Kolmogorov scales. In contrast, figure 4.19(b) suggests that droplets for both oils follow the ostensible scales of the flows. The monotonic decline in the mean droplet diameter suggests a universal trend, albeit over a single decade of We number, as argued by [Kolmogorov(1949)]. The reference line in (b) is $\tilde{d}/D = 0.45\ We^{-1/5}$. [Johansen *et al.*(2013)] , following a series of experiments in the facility described by [Brandvik *et al.*(2013)], propose that the droplet diameter behaves like $We^{-3/5}$ where the Weber number is defined implicitly in terms of the droplet size. Clearly, the data shows that the interfacial tension is an essential factor in determining the droplet size at the edges of the oil jets. The droplets form and evolve under the competition of shear stresses and surface tension at the oil-water interface. The precise mechanism of their formation and dynamics is beyond the subject matter of the current study. However, for better understanding of the their behavior (e.g. splitting, coalescence, oscillation), a systematic study with respect to Weber number would be illuminating, as noted in [Hinze(1955)] and [Eastwood *et al.*(2004)].

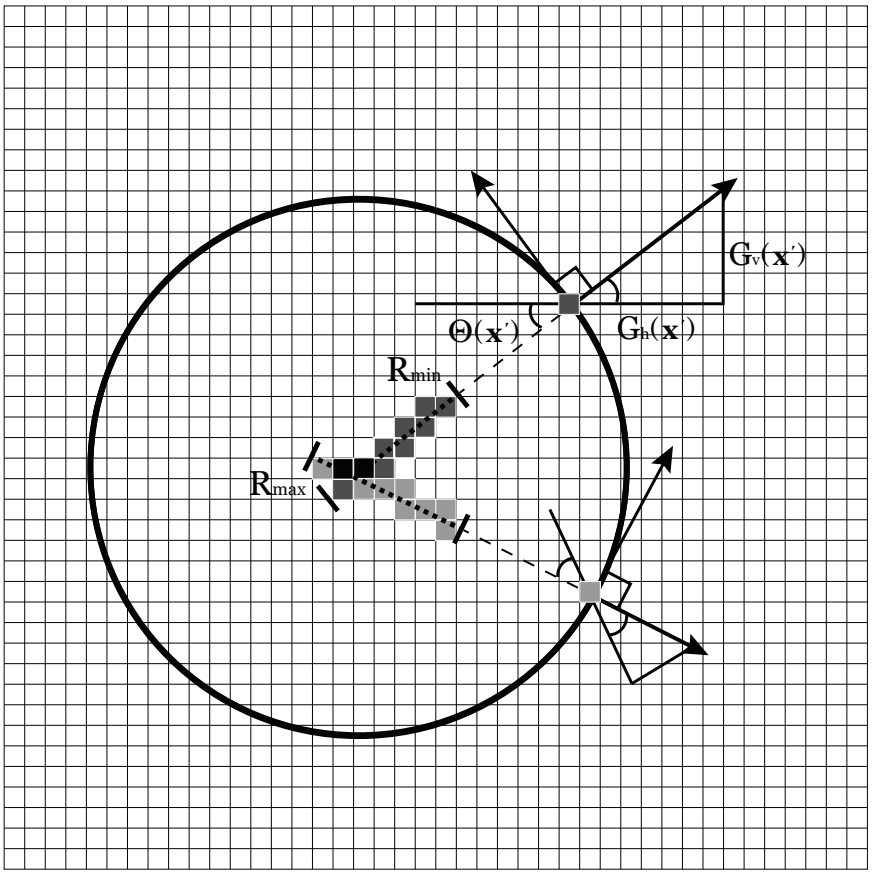

Figure 4.14: Illustration of identification of a circular droplet via Hough transform.

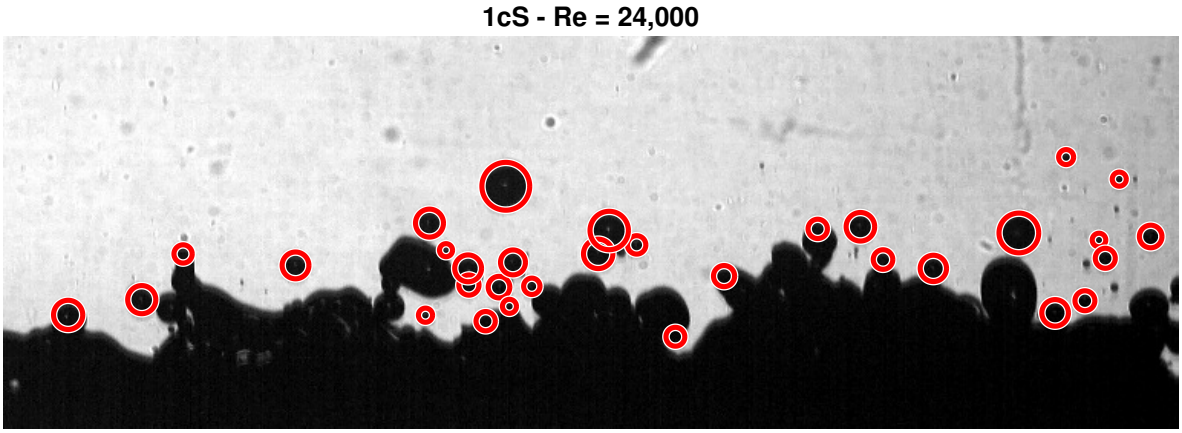

(a)

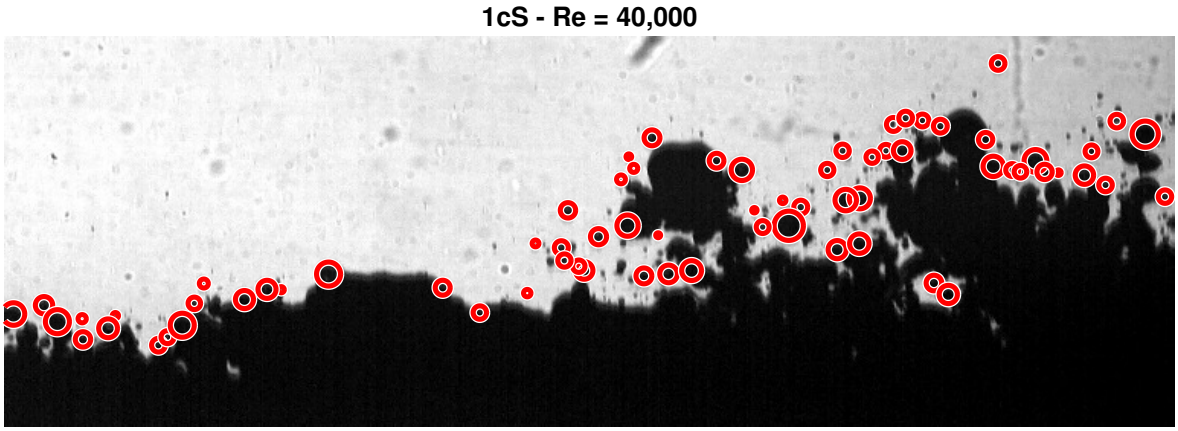

(b)

Figure 4.15: Identification of 1cS-oil droplets in water.

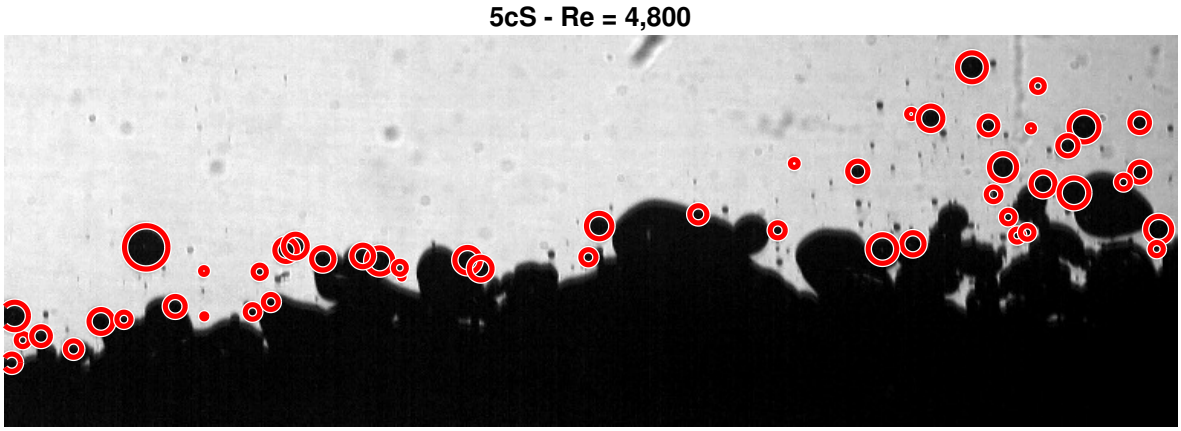

(a)

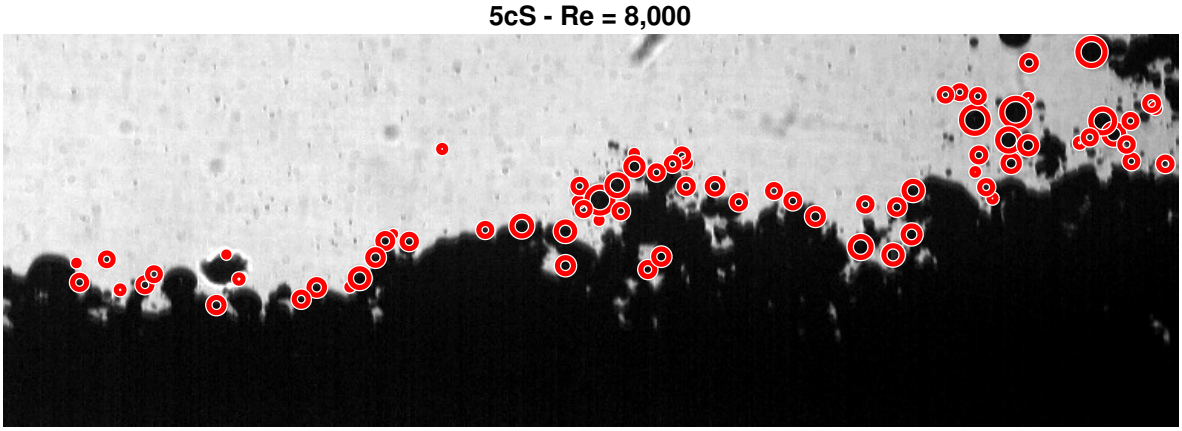

(b)

Figure 4.16: Identification of 5cS-oil droplets in water.

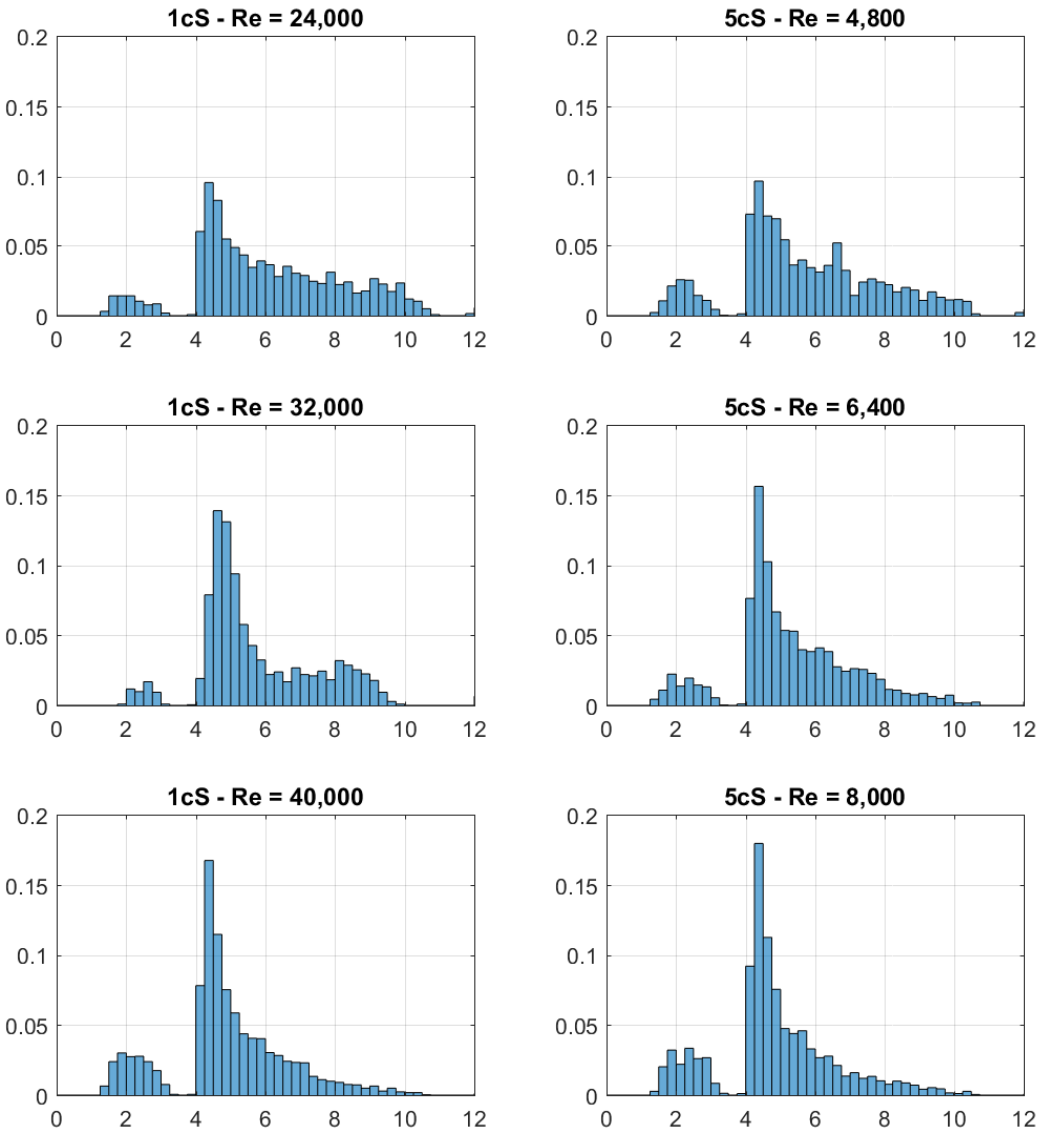

Figure 4.17: Oil droplet size histograms: 1cS-oil (left) and 5cS-oil (right) combined. Droplet size are resolved at 1/4 pixel resampling. The clusters around 2 pixels diameter are secondary droplets forming during pinch-off.

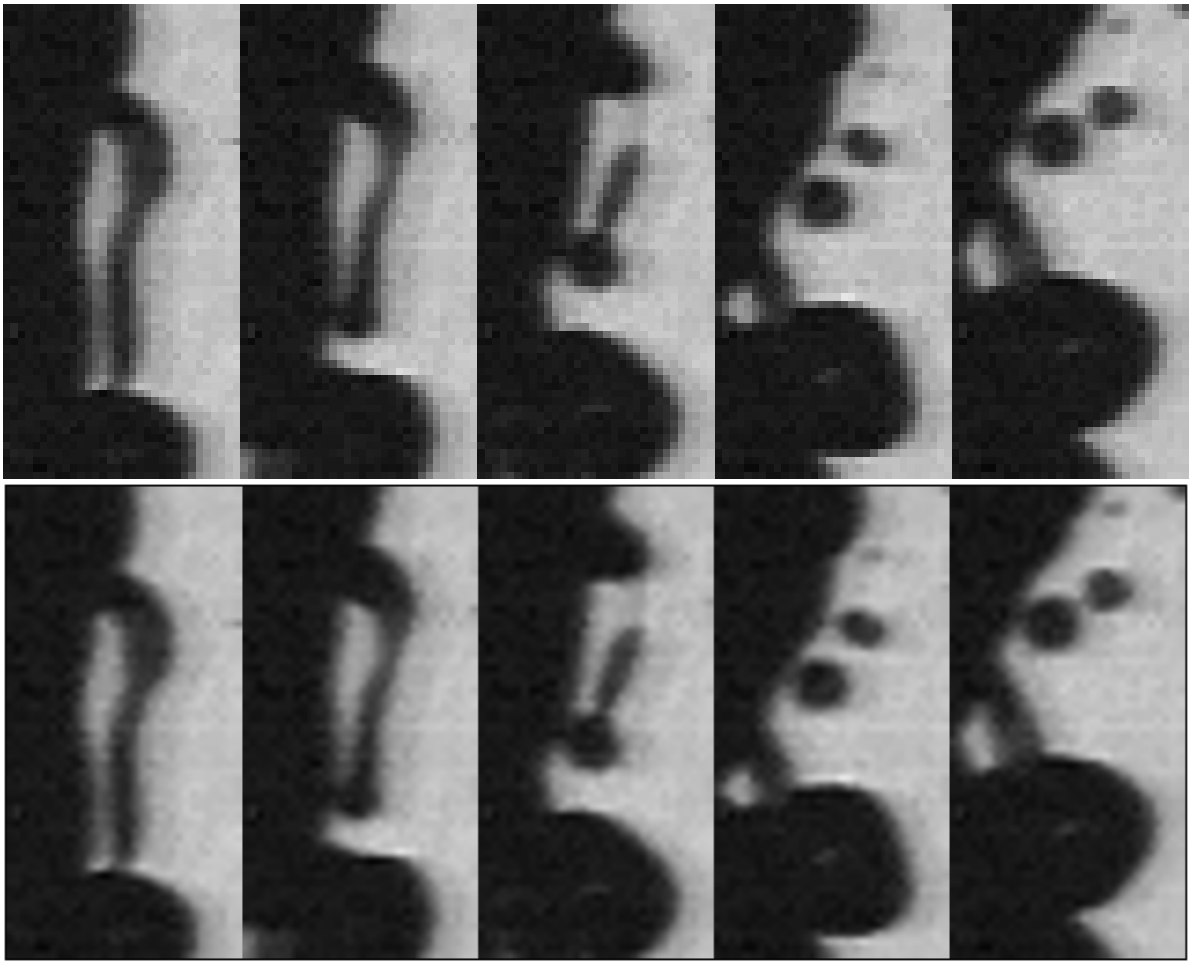

Figure 4.18: Droplet formation. Details from Flow 27 in Table 2.2. Raw images (top row) and rescaled images using bilinear interpolation (bottom row). Image area is 3mm×5mm. Images are 2 ms apart.

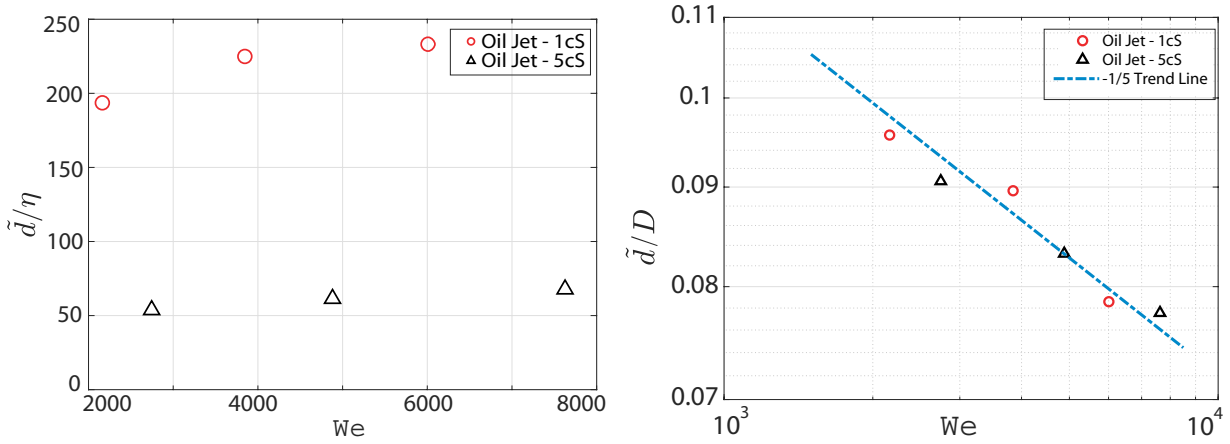

(a) (b)

Figure 4.19: Scaling of mean oil droplet size of the discharge flow with (a) estimated Kolmogorov scales in linear axes and (b) the jet diameter in logarithmic axes. The secondary droplets seen in figure 4.17 are excluded. The $-1/5$ slope line in (b) is drawn for visual reference: $\tilde{d}/D = 0.45We^{-1/5}$.

Chapter 5

Closing Remarks

The goal of this work was to formulate and test a set of methods that would allow discussion of turbulent flows; what is presented here pertains to turbulent jets, both homogeneous and immiscible, in the near field. The curvature analysis method can be used to parse results based on location along the axis of the jet, making it possible to study the form of the individual interfacial structures. Pixelwise Time Filter provides a framework for investigators to audit high-speed recordings of fluid motions, segregating features by their pixelwise signatures as they move through the image space. The interfacial length scale analysis falls short in providing information about the individual structures or droplets, but it does provide information about a quantifiable length scale for the region interrogated along the axis of the jet.

All methods suffer from limitations in data acquisition. Limitation of spatial resolution incurs noise in the measurements that appear as quantization errors for the curvature analysis scheme. Poor image quality, resulting from insufficient illumination or overexposure, also limits the effectiveness of the interfacial length scale approach, where streaks and blurring drastically effect the ability to obtain meaningful results. The effective band-pass ranges used in the PixTiF process are also limited by the capture rate and length of the recording (length of the temporal signal).

The relationship between the temporal and spatial scale provides a framework to extract flow parameters based on visual features of turbulent flows. A combination of the methods detailed here could be used to investigate cloud motions (utilizing satellite captures), environmental scale plumes, or events where other quantitative measurements may not being readily obtained. A relatively available application for researchers is to apply temporal filtering to schlieren recordings from previous work, providing an approach to possibly gain new insight by revisiting their datasets. Advancements in computational imaging techniques should be reviewed and applied to enhance experimental practices in the investigation of turbulence.

Acknowledgments

Part of this work was supported by the US Department of Interior, Bureau of Safety and Environmental Enforcement, Award No: DE-FE0014314, and the U.S. Department of Energy.

The following in this subsection is to serve as a reminder to myself and may be ignored.

I want to take the opportunity here to thank all the amazing people I have come to know at my time at Berkeley:
◦ The amazing Graduate Student Instructors that I learned under, from which I stole/borrowed ingenious teaching techniques/styles.
◦ The illustrious educators, that introduced my world to novel concepts with passion and wonder.
◦ The brilliant students, from which I have learned more from than I have perhaps taught.
◦ My precious friends I have made along the way, I would have been lost without you.
◦ The Hesse building staff: Mike, Alex, Daniel, Scott, and Tom. It might have never been your job, but you always took such great care of me, with support, knowledge, trust, and respect.
◦ The extended family that is the lab of 140 Hesse: Jocelyn, Onur, Rachael, Fatih, Daniel, Megan, Abdullah, and the coffee machine. You all have picked me up and warmed my spirit, to keep working and enjoying life, more times than I could ever keep track of.
All of this work was supported by the patience and encouragement of Ömer Savaş, without whom I would not be here. From my time with him, I have learned a couple of things. By watching him, I have gained a preliminary outlook on what it is to be an educator and the joy that comes from sharing what knowledge or experience one has. The value of practicing patience, empathy, and humility in general. And, I now and forever will share, "You have nothing without your health", safety is paramount. If I can keep passing what I have gained onto others as they grow, I will be happy.
I could not imagine having gone through this without my dad. Talking with him every night, from 2007 til 2011—at which point, we switched to video chatting, which we still do to this day. It has been everything. His ability to find humor in daunting times always inspires me to keep trying to find the joy in the work.
To my partner Sarah, I am thrilled to see what comes on our path.

References

[Abramowitz & Stegun (1964)] Abramowitz, M. & Stegun, I.A. 1964 Hanbook of Mathematical Functions, NBS, Applied Mathematics Series, No: 55, Washington, D.C. §25.3.6 and §25.3.24.

[Atherton & Kerbyson(1993)] Atherton, T.J. & Kerbyson, D.J. 1993 The coherent circle Hough transform. *BMVC.*

[Bardet *et al.*(2018)] Bardet, P. M., Peterson, P. F. & Savaş, Ö. 2018 Annular swirling liquid layer with a hollow core. *Journal of Fluid Mechanics*, **841**, 784–824.

[Bardet *et al.*(2010)] Bardet, P. M., Peterson, P. F. & Savaş, Ö. 2010 Split-screen single-camera stereoscopic PIV application to a turbulent confined swirling layer with free surface. *Experiments in Fluids*, **49**, 513–524.

[Bogusławski & Popiel(1979)] Bogusławski, L. & Popiel, Cz. O. 1979 Flow structure of the free round turbulent jet in the initial region. *J. Fluid Mech.*, **90** (3), 531–539.

[Brandvik *et al.*(2013)] Brandvik, P.J., Johansen, Ø., Leirvik, F., Farooq, U. & Daling, P.S. 2013 Droplet breakup in subsurface oil releases – Part 1: Experimental study of droplet breakup and effectiveness of dispersant injection. *Marine Pollution Bulletin* **73** 319—326.

[Canny(1987)] Canny, J. 1987 A computational approach to edge detection. *IEEE Transactions on Systems, Man and Cybernetics.* 184–203.

[Catrakis & Dimotakis(1996)] Catrakis, H.J. & Dimotakis, P.E. 1996 Mixing in turbulent jets: scalar measures and isosurface geometry. *J. Fluid Mech.*, **317**, 317–406.

[Chitanont *et al.*(2015)] Chitanont, N., Yaginuma, K., Yatabe, K. & Oikawa, Y. 2015 Visualization of sound field by means of Schlieren method with spatio-temporal filtering. *International Conference on Acoustics, Speech and Signal Processing*, 509-513.

[Crow & Champagne (1971)] Crow, S.C. & Champagne, F.H. 1971 Orderly structure in jet turbulence. *J. Fluid Mech.*, **48** (3), 547–591.

[Coles(1981)] Coles, D. 1981 Prospects for useful research on coherent structure in turbulent shear flow. *Proc. Indian Acad. Sci. (Eng. Sci.)* **4**, 111 –127 .

[Coles(1985)] Coles, D. 1985 The uses of coherent structure (Dryden Lecture). 1-13. *AIAA Paper 85-0506.* `http://dx.doi.org/10.2514/6.1985-506`

[Dimotakis(2000)] Dimotakis, P.E. 2000 The mixing transition in turbulent flows. *J. Fluid Mech.*, **409**, 69–98.

[Dimotakis *et al.*(1983)] Dimotakis, P.E., Miake-Lye, R.C. & Papantoniou, D.A. 1983 Structure and dynamics of round turbulent jets. *Physics of Fluids*, **26** (11), 3185–3192.

[Duda & Hart(1972)] Duda, R.O. & hart, P.E. 1972 Use of the Hough transformation to detect lines and curves in pictures. *Graphics and Image Processing.* Ed. W. Newman

[Eastwood *et al.*(2004)] Eastwood, C.D., Armi, L. & Lasheras, J.C. 2004 The breakup of immiscible fluids in turbulent flows. *J. Fluid Mech.*, **502**, 309–333.

[Eustice *et al.*(2002)] Eustice, R., Pizarro, O., Singh, H. *et al.*Howland, J. 2002 UWIT: Underwater Image Toolbox for optical image processing and mosaicking in MATLAB. *IEEE Proceedings of the 2002 International Symposium on Underwater Technology*, , 141–145.

[Girifalco & Good(1957)] Girifalco, L.A. & Good, R.J. 1957 A theory for the estimation of surface tension and interfacial energies. I. Derivation and application to interfacial tension. *J. Phys. Chem*, **61**, 904–909.

[Hinze(1955)] Hinze, J.O. 1955 Fundamentals of the hydrodynamics mechanisms of splitting in dispersion processes. *AIChE J.*, **1**, 289 —295.

[Hinze(1975)] Hinze, J.O. 1975 Turbulence, McGraw-Hill Inc., New York, NY.

[Holzner *et al.*(2007)] Holzner, M., Liberzon, A., Nikitin, N., Kinzelbach, W. & Tsinober, A. 2007 Small-scale aspects of flows in proximity of the turbulent/nonturbulent interface. *Physics of Fluids*, **19** (7), 071702(1-4).

[Hough(1962)] Hough, P.V.C. 1962 Method and means for recognizing complex patterns. U.S. Patent 3,069,654, Dec. 18, 1962.

[Hu *et al.*(2003)] Hu, H., Saga, T., Kobayashi, N. & Taniguchi, N. 2003 Analysis of a turbulent jet mixing flow by PIV-PLIF combined system. *J. Visualization*, **7**(1), 33 – 42.

[Hunt *et al.*(2006)] Hunt, J.C.R., Eames, I. & Westerweel, J. 2006 Mechanics of inhomogeneous turbulence and interfacial layers. *J. Fluid Mech.* **554**, 499 — 519.

[Hunt *et al.*(2011)] Hunt, J.C.R., Eames, I. da Silva, C.B. & Westerweel, J. 2011 Interfaces and inhomogeneous turbulence. *Phil. Trans. R. Soc. A* **369**, 811-–832.

[Hübner(2004)] Hübner, J. 2004 Buoyant plumes in a turbulent environment PhD Thesis, University of Cambridge.

[Ibarra, Shaffer, & Savaş (2020)] Ibarra, E., Shaffer, F. & Savaş, Ö. 2020 On the near-field interfaces of homogeneous and immiscible round turbulent jets. *J. Fluid Mech.*, 889.

[Jang & Chin(1990)] Jang, B.K. & Chin, R.T. 1990 Analysis of thinning algorithms using mathematical morphology. *IEEE Transactions on Pattern Analysis and Machine Intelligence*, **12**(6), 541–551.

[Johansen *et al.*(2013)] Johansen, Ø., Brandvik, P.J. & Farooq, U. 2013 Droplet breakup in subsea oil releases – Part 2: Predictions of droplet size distributions with and without injection of chemical dispersants. *Marine Pollution Bulletin* **73** 327—335.

[Kolmogorov(1949)] Kolmogorov, A.N. 1949 On the breakage of drops in a turbulent flow. *Dokl. Akad. Nauk. SSSR*, **66**, 825 -– 828. English translation in *Selected Works of A. N. Kolmogorov*, Vol. 1. Ed. V. M. Tikhomirtov, pp. 339–343, Springer.

[Lau & Fisher(1975)] Lau, J.C. & Fisher, M.J. 1975 The vortex-street structure of 'turbulent' jets. *J. Fluid Mech.*, **67**(2), 299–337.

[McNutt *et al.*(2011)] McNutt, M.K., Camilli, R., Crone, T.J., Guthrie, G.D., Hsieh, P.A., Ryerson, T.B., Savaş, Ö. & Shaffer, F. 2011 Review of flow rate estimates of the Deepwater Horizon oil spill. *PNAS.*

[Morton(1959)] Morton, B.R. 1959 Forced plumes. *J. Fluid Mech.*, **5**(1), 151–163.

[Nikuradse(1932)] Nikuradse, J. 1932 Gesetzmäsigkeiten der turbulenten Stromung in glaten Rohren. Translated as 'Laws of turbulent flow in smooth pipes', NASA TT F-10, 359 (1966).

[Ortega *et al.*(2003)] Ortega, J.M., Bristol, R.L. & Savaş, Ö. 2003 Experimental study of the instability of unequal strength counter-rotating vortex pairs. *J. Fluid Mech.*, **474**, 35–84.

[Otsu(1979)] Otsu, M. 1979 A threshold selection method from grey-level histograms. *IEEE Transactions on Systems, Man and Cybernetics.*, **9** (1), 62–66.

[Pizer *et al.*(1987)] Pizer, S.M., Amburn, E.P., Austin, J.D., Cromartie, R., Geselowitz, A., Greer, T., ter Haar Romeny, B., Zimmerman, J.B. & Zuiderveld, K. 1987 Adaptive histogram equalization and its variations *Computer Vision, Graphics, and Image Processing.* **39** (3), 355–368.

[Pope(2000)] Pope, S.B. 2000 Turbulent Flows, Cambridge University Press, Cambridge, UK.

[Popiel & Trass(1991)] Popiel, C.O. & Trass, O. 1991 Visualization of a free and impinging round jet. *Experimental Thermal and Fluid Science*, **4** (3), 253–264.

[Reinsch(1967)] Reinsch, C. H. 1967 Smoothing by spline functions. *Numerische Mathematik*, **10** (3), 177–183.

[Savaş & Gollahalli(1986)] Savaş, Ö. & Gollahalli, S.R. 1986 Flow structure in near-nozzle region of gas jet flames. *AIAA J.* **24** (7), 1137–1140.

[Savaş(2012)] Savaş, Ö. 2012 A visual study in the near field of turbulent jets and implications for estimating accidental discharges. *Experiments in Fluids* **53**(5), 1501–1514.

[Sezgin & Sankur (2004)] Sezgin, M. & Sankur, B. 2004 Survey over image thresholding techniques and quantitative performance evaluation. *Journal of Electronic Imaging*, **13**, 146–168.

[Shaffer *et al.*(2015)] Shaffer, F., Savaş, Ö., Lee, K. & De Vera, G. 2015 Determining the discharge rate from a submerged oil leak jet using ROV video. *Flow Measurement and Instrumentation*, **43**, 34-46.

[Shaffer, Ibarra, & Savaş (2021)] Shaffer, F., Ibarra, E., & Savaş, Ö. 2021 Visualization of submerged turbulent jets using particle tracking velocimetry. *Journal of Visualization*, 1-12.

[Sholl & Savaş(1997)] Sholl, M. & Savaş, Ö. 1997 A fast Lagrangian PIV method for study of general high gradient flows. *AIAA Paper 97-0493.*

[Sobel & Feldman(1968)] Sobel, I. & Feldman, G. 1968 A 3×3 isotropic gradient operator for image processing. Presented at a talk at the Stanford Artificial Project. (Indirect reference.)

[Taylor(1934)] Taylor, G.I. 1934 The formation emulsions in definable fields of flow. *Phil. Trans. R. Soc. A* **146**, 501–523.

[Tukey(1967)] Tukey, J.W. 1967 An introduction to the calculations of numerical spectrum analysis. *Spectral Analysis of Time Series*: 25–46.

[Turner(2012)] Turner, J.S. 1979 Buoyancy effects in fluids, Cambridge University Press, Cambridge,

[Westerweel *et al.*(2002)] Westerweel, J., Hoffman, T., Fukushima, C. & Hunt, J.C.R. 2002 The turbulent/nonturbulent interface at the outer boundary of a self–similar turbulent jet. *Experiments in Fluids*, **33**, 873—878.

[Westerweel *et al.*(2005)] Westerweel, J., Fukushima, C., Pedersen, J.M. & Hunt, J.C.R. 2005 Mechanics of the turbulent-nonturbulent interface of a jet. *Physical Review Letters* **95**.(17).

[Westerweel *et al.*(2009)] Westerweel, J., Fukushima, C., Pedersen, J.M. & Hunt, J.C.R. 2009 Momentum and scalar transport at the turbulent/non-turbulent interface of a jet. *J. Fluid Mech.* **631**, 199 – 230.

[Westerweel *et al.*(2011)] Westerweel, J., Petracci, A., Delfos, R. & Hunt, J.C.R. 2011 Characteristics of the turbulent/non-turbulent interface of a non-isothermal jet. *Phil. Trans. R. Soc. A* **369**, 723–737. DOI: 10.1098/rsta.2010.0308

[Yule(1978)] Yule, A.J. 1978 Large-scale structure in the mixing layer of a round jet. *J. Fluid Mech.*, **89** (3), 413–432.

[Zhao *et al.*(2016)] Zhao, L., Shaffer, F., Robinson, B., King, T., D'Ambrose, C., Pan, Z., Gao, F., Miller, R.S., Conmy, R.N. & Boufadel, M.C. 2016 Underwater oil jet: Hydrodynamics and droplet size distribution. *Chemical Engineering Journal*, **299**, 293–303. Elsevier.